Investigation of Thermal Tempering in Bulk Metallic Glasses

Thesis by

Cahit Can Aydıner

In Partial Fulfillment of the Requirements

for the Degree of

Doctor of Philosophy

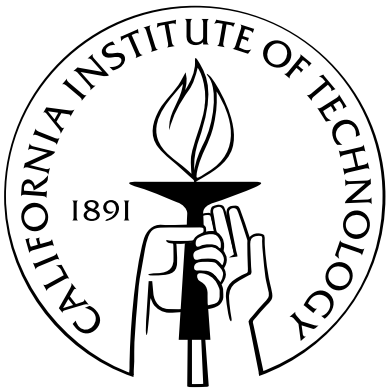

California Institute of Technology

Pasadena, California

2004

(Defended December 11, 2003)

Acknowledgements

The last five years at this leading science institute have challenged me in many different ways, from the intense load of heavily theoretical classes to experiments that seemed like they will never work. I could survive through all with dearly bought gifts of adapted ('built') character and developed intellect. This could not be possible without the support of many people, and I'll try to express my gratitude to them, although it will be impossible to name all of them here.

I would like to thank my advisor, Prof. Üstündağ, for giving me the opportunity to work on this project. I appreciate his advice and guidance especially during the period that I was trying to become some sort of an experimentalist. Also, he put conscious effort to make his group members meet facets of academic life outside Caltech. So, I'd like to thank him for my national laboratory and conference experiences that broadened my scientific vision and allowed me to meet many good researchers/people. I also owe my appreciation to Prof. Hall for his advice in the always-difficult first year at Caltech. I would like to thank Prof. Knauss, Prof. Ravichandran and Prof. Johnson for graciously agreeing to be members of my thesis committee.

I'm grateful to everyone from whom I received various forms of help in this scientific investigation. In this respect, special thanks are to Dr. Michal B. Prime of Los Alamos National Laboratory. Dr. Prime was extremely courteous sharing his years of know-how

and experience on the residual stress measurement technique used in this study. At the very first time I tried this method, I felt quite surprised when I saw the experiment was working, rather than joyful (which caught up later), probably due to the long period of frustration with other methods during which my subconscious was convinced that experiments, quite simply, do not really do so. Every experimentalist, although what he has to do is to develop a solid, hard-to-discourage character, needs a moment of success once in a while. I'd like to thank Dr. Prime for my first such moment. Also, I'd like to gratefully acknowledge Dr. Atakan Peker of Liquidmetal Technologies who helped me many times with sample production.

To name all the friends that helped me through these years (and it is in help category even when your friend shares your moment at Red Door Cafe to relax your research-loaded nerves) is impossible and will always result in an incomplete list. Hence, to represent my thanks to them all, I choose my oldest friends (room mates) here: Burak Erdoğan and Arkadaş Özakın. Also, the support of these extremely bright individuals in my first year struggle with Caltech classes is sincerely appreciated. They really made me think again when I thought I was an analytical thinker.

And on a larger timescale, I'd like to thank my mother, Türkan Aydıner, who cared so deeply for my education at every stage of my life. Without her guidance, which always felt like coming from an encouraging friend, I could never be as successful. I'd like to thank my father, Gökhan Aydıner, for setting an incredible example of work ethic. I become more able to appreciate his sound principles as life proceeds.

Abstract

Bulk metallic glasses are recent advanced materials which generate residual stresses due to rapid cooling from their surfaces during processing. These stresses arise from the thermal gradients that form within the sample at and above the glass transition region. A typical processing of BMGs involves feeding the alloy melt into a mold followed by severe quenching. The formation and nature of these stresses are analogous to the residual stresses due to the thermal tempering of silicate glasses. This analytical-experimental study investigates the thermal tempering phenomenon in BMGs for the first time.

One of the best glass forming metallic alloys, $Zr_{41.2}Ti_{13.8}Cu_{12.5}Ni_{10}Be_{22.5}$ (Vitreloy 1^{TM}), is employed in this study. First, the best technique for the high-resolution measurement of residual stresses in BMGs is determined to be the crack compliance method. Second, the formation of the stresses is modeled with three different levels of viscoelastic phenomenology, namely, an instant freezing model, a viscoelastic model and a structural model. The first is a simplistic analytical model to estimate residual stresses whereas the structural model accounts for the temperature history dependence of the glassy structure. The constitutive laws for the viscoelastic and structural models are incorporated into the finite element method (ABAQUS^{TM} software package) allowing the application of these models to complex geometries. To increase the accuracy of the analysis, the 'correct' temperature evolution in the sample during processing has to be input to these 'mechanical'

models. Therefore, the heat transfer problem during the casting process of the BMG is analyzed in detail. Accuracy also requires a detailed knowledge of the thermal parameters of the material as a function of temperature; thus, some attention is also devoted to their measurement.

At the end, calculated and measured stresses are compared and good agreement is achieved. BMGs are demonstrated to be capable of generating very high (around 400 MPa) compression on their surfaces. The study also yielded valuable physical insight into the thermal tempering process itself. It is seen that this process exhibits significant discrepancies in BMGs compared to its analogy in silicate glasses. For instance, the transient tensile stresses that develop in the latter are shown to be lacking in the BMGs. Another discrepancy between the two materials is that the density of BMGs is uniform across the sample cross section in contrast to that found in silicate glasses. Overall, this investigation developed sufficient understanding of the thermal tempering phenomenon in BMGs to establish it as a viable process to manipulate properties.

Contents

List of Figures

List of Tables

Chapter 1

Introduction

1.1 Motivation

Although metallic glasses have been made since 1960s, specimen dimensions were previously limited to tens of μm due to the very fast cooling rates (about 10^6 to 10^{12} K/s) needed in order to prevent crystallization. Recently, multicomponent alloys have been developed with exceptional glass formation ability that allow the processing of bulk specimens (Peker [67]). These alloys form glass at critical cooling rates low enough to allow the casting of specimens up to 5 cm in diameter. The ability to prepare large specimens has permitted the bulk characterization of these materials using more *traditional* techniques. The unique properties of bulk metallic glasses (BMGs) place them among significant engineering materials: very high strength (1.9 GPa), good fracture toughness (20–55 $\mathrm{MPa} \cdot \mathrm{m}^{1/2}$), a high specific strength, excellent wear and corrosion resistance, and a high elastic strain limit (up to 2 %) (see, e.g., Gilbert et al. [35] and Bruck et al. [17]).

One important question that arises with bulk production is the nature and magnitude of processing induced residual stresses, since, as with all materials, these stresses can affect the mechanical behavior of BMGs significantly. Typical processing of BMGs includes rapid cooling of the alloy from the melt (above liquidus temperature) such that the material

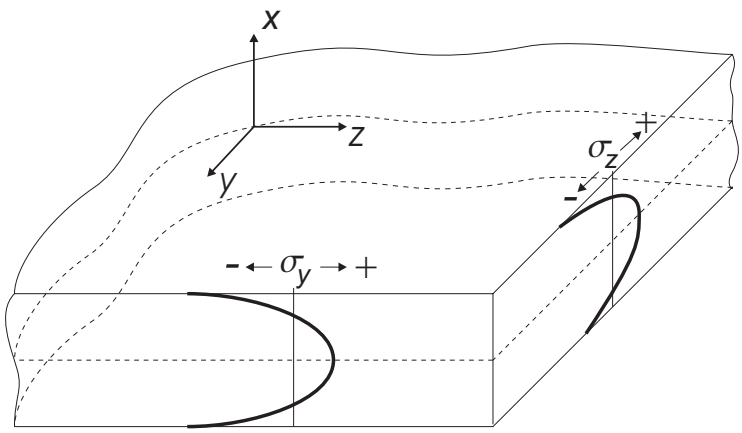

Figure 1.1: Typical residual stress state in an infinite glass plate subjected to thermal tempering. Stresses are equibiaxial varying only in the out-of-plane direction (x). This stress profile is roughly parabolic with surface compression balanced by tension in the interior.

undergoes glass transition and remains amorphous. Observing the fairly low thermal conductivity of these alloys ($\sim 10\,\mathrm{W/(m \cdot K)}$ at glass transition), rapid cooling from the surface would form significant thermal gradients in these 'thick' samples, i.e., a surface point will cool considerably faster than a point at the core. Thermal gradients that form above and during the glass transition were observed to generate residual stresses in the more traditional amorphous materials (see, e.g., Gardon [34] for silicate glasses and Struik [82] for polymers). These residual stresses had a typical compression on the surface balanced by tension in the interior, and they were the subject of an intense research activity, in particular, for silicate glasses. The motivation there was that the bending strength of silicate glass plates could be significantly improved with the residual stresses of this nature (as much as three times their regular strength). Therefore, inducing residual stresses by heating above glass transition and subsequent rapid quenching has become an industrial process. The process/phenomenon is known as 'thermal tempering' (Gardon [34]) and the typical residual stress profile in a thermally tempered plate is shown in Figure 1.1.

The hypothesis of the present study is that residual stresses with the same mechanism could also be formed in metallic glass samples. Therefore, the name 'thermal tempering' is inherited. The study involves the following topics and challenges:

1. Investigation of relevant material properties and constitutive behavior

   Thermal tempering is a thermomechanical problem that is extremely material data intensive. Furthermore, the temperature span of the process in BMGs (up to 1000 K), and therefore the temperature span over which material data are required, is several times that of the silicate glasses. Also, investigation of these properties between glass transition and liquidus temperature is inhibited by phase separation and crystallization in BMGs.

2. Controlling and monitoring of the processing conditions

   BMGs need to be cast from their melt under a controlled atmosphere (inert gas flush or vacuum), since oxygen is utterly detrimental to glass formation. This requirement and the high temperature of the melt ($\sim 900^{\circ}$C) pose a difficult problem to monitor the process.

3. Modeling of residual stresses with the input of items 1 and 2

   This involves determination of models that comprise sufficient physics to predict the residual stresses successfully.

4. Measurement of residual stresses

   BMGs, as opaque and amorphous materials, preclude the use of typical non-destructive methods of photoelasticity or X-ray diffraction. Also, the problem requires not an average value of surface residual stresses as most methods would offer, but the high-

resolution measurement of the residual stress profile through the thickness for meaningful comparison with model results. This know-how did not exist in the literature, hence, adapting a 'powerful' residual stress measurement method to these materials is an important goal of this study.

1.2 Formation of Thermal Tempering Stresses

In silicate glass tempering, the thermal tempering process involves (i) cooling a glass plate above its glass transition temperature (T_g) by $\sim\ 50-100$ K where it is still viscous enough to retain its shape and then (ii) rapidly cooling it from both sides, typically by air quenching.

During this process, first, temperature gradients form in the sample that is initially at a uniform temperature, T_i, i.e., surface cools faster than the mid-plane. Then, these gradients grow and reach a maximum, realized by the maximum differential between the mid-plane and surface temperatures. After this point, the gradients decay and the sample temperature eventually settles to the ambient temperature, T_a .

In an always-elastic plate, stress generation in a time increment dt due to an x-symmetric temperature increment $dT(x,t)$ across the thickness is given by the simple thermoelastic formula (e.g., Timoshenko and Goodier [85], p. 433)

$$d\sigma = \frac{E\,\alpha}{1-\nu}(dT(x,t) - d\bar{T}(t)) \tag{1.1}$$

where E is the Young's modulus, ν is the Poisson's ratio, α is the coefficient of thermal expansion, $d\bar{T}$ is the temperature increment averaged over x. Integrating this equation, it is easy to see that no residual stresses are generated due to cooling from the uniform temperature T_i to the uniform temperature T_a, since stresses generated during the growth

of temperature gradients are nullified by the equal-in-magnitude but opposite stresses that form as the gradients decay.

On the other hand, stress evolution in thermal tempering is different due to three stages of material behavior demonstrated in Figure 1.2. In this figure, the temperature profile is pictured at the top in reference to T_i, T_g and T_a, whereas corresponding stress state is shown at the bottom.

In the first stage, the temperatures in the entire cross section are sufficiently above glass transition such that stresses formed by imposed thermal gradients are instantly relaxed. Let us call this material behavior 'liquid' for which typical stress relaxation time is much smaller than the process time scale. Hence, thermal gradients are formed but no stress is generated (Figure 1.2(i)).

When the surface temperature cools down to the temperature at which relaxation time becomes comparable to the process time scale, 'solidification stage' commences and the surface of the material becomes capable of holding stresses. This material behavior is called 'viscoelastic' and involves simultaneous relaxation of the generated stresses. Eventually, the material will cool to a temperature at which relaxation time becomes large compared to the process time scale, and thus, the material becomes 'elastic'. As neighboring layers cool, an increasingly bigger fraction of the cross section becomes viscoelastic, and subsequently, elastic. Finally, the center of the material will freeze at time t_s which is the end of the 'solidification' stage. The temperature and stress profile at an instant in the solidification stage are demonstrated in Figure 1.2(ii). Note on this figure that stresses do not exist in the still fluid region about the core. The sense of stresses generated (via equation (1.1)) naturally depends on whether temperature gradients are still growing or started to decay at this stage of the process. For silicate glasses T_i is close to T_g, and typically the former

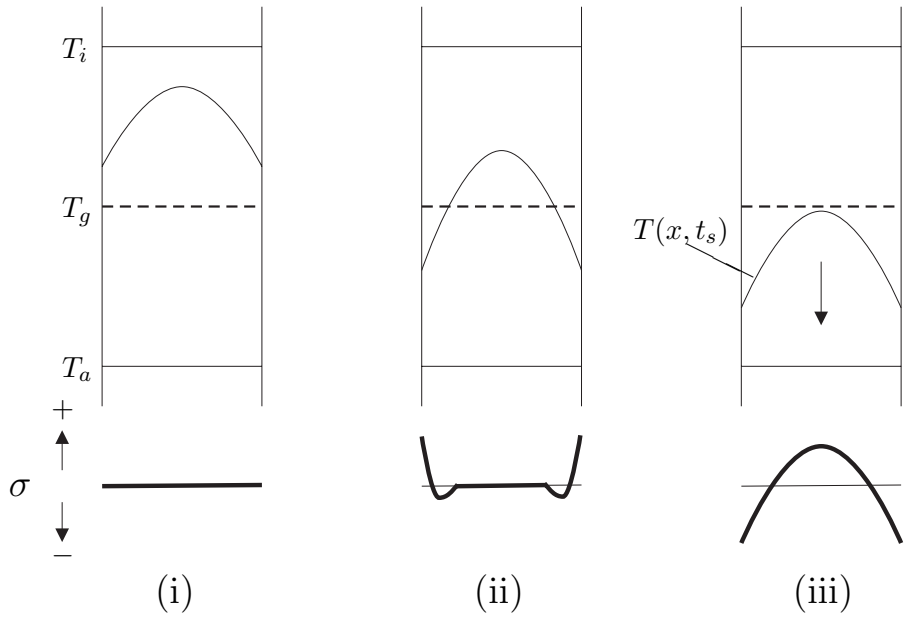

Figure 1.2: Temperature profiles (top) and stress states (bottom) in the three stages of thermal tempering: (i) The temperatures are sufficiently above glass transition T_g and stresses are zero although thermal gradients exist. (ii) Solidification stage; part of the cross section became capable of holding stresses and relaxation times decrease from the (cold) surface to the (hot) mid-plane. The shown stress state is for still-growing thermal gradients that results in tension at the surface. At this particular instant, a region about the mid-plane is still 'liquid' and does not hold stress. (iii) Temperature equalization stage; begins with the solidification of entire cross section at time t_s. In this stage, the temperature profile $T(x, t_s)$ decays to uniform T_a. The shown stresses are temperature equalization stresses, namely, the thermoelastic stresses generated during this decay.

is the case leading to tensile stresses at the surface. This was the case demonstrated in Figure 1.2(ii). The stresses generated are prone to viscous relaxation until t_s and the ('survived') stresses at this point, $\sigma(x, t_s)$, are called the 'solidification stresses.'

In the third stage of thermal tempering that starts at time t_s, the material becomes practically an elastic plate, imposed with the temperature profile at that instant. The stresses that will be generated upon decay of this temperature profile are called 'temperature equalization stresses,' and determined via equation (1.1) as

$$\sigma(x, \infty) - \sigma(x, t_s) = -\frac{E\alpha}{1-\nu}(T(x, t_s) - \bar{T}(t_s)) \tag{1.2}$$

Temperature equalization stresses are compressive on the surface and tensile in the core and they are demonstrated in Figure 1.2(iii). The final residual stresses ($\sigma(\mathbf{x}, \infty)$) are obviously the superposition of solidification and temperature equalization stresses, and due to relaxation in the first and second stages, the former is smaller in magnitude[1]. As a result, residual compression is obtained on the surface balanced by mid-plane tension.

Gardon [34] reviewed the thermal tempering of silicate glasses and terms such as temperature equalization and solidification stresses are taken from this work. Unlike the trivial temperature equalization stresses, the analysis of solidification stresses and the stress evolution in the glass transition region is a complicated problem and necessitate various levels of viscoelastic phenomenology. Gardon classifies the varius models developed for silicate glasses as instant-freezing theories (e.g., Aggarwala and Saibel [3]), the viscoelastic theory (Lee et al. [50]) and the structural theory (Narayanaswamy [63, 64]). The first is a simplistic approach to estimate residual stresses, the second is the linear thermoviscoelastic treatment with time-temperature-superposition principle and the last one is nonlinear viscoelastic accounting for the temperature history dependence of the glass structure. The latter theory is accepted to be the *definitive* theory of thermal tempering in silicate glasses since it achieved reasonable agreement with experiments for both the evolution and magnitude of temper stresses. In silicate glasses, photoelasticity could be used to monitor both the evolution and final value of temper stresses whereas for BMGs no known method will avail to monitor the stress evolution *in situ*.

[1] As explained, the sense of solidification stresses are dependent on the process and they may be partly neutralizing (as is the case in Figure 1.2) or contributing to the temperature equalization stresses.

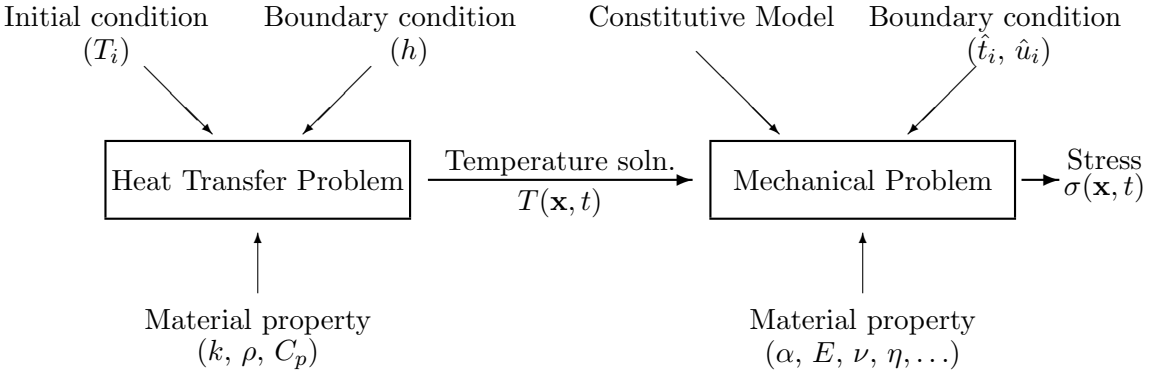

Figure 1.3: Structure of the thermal tempering problem: The heat transfer problem is uncoupled from the mechanical problem due to the dominance of forced cooling over heat generation by viscous mechanisms. Hence, it is solved first with the inputs of the boundary condition (e.g., that imposed by the heat transfer coefficient, h), the initial conditions (e.g., initial temperature, T_i), and material parameters in the heat equation. The obtained temperature solution $T(x,t)$ is then fed to the mechanical problem which is solved with a constitutive model (instant freezing, thermoviscoelastic, etc.), the material properties required by the chosen model and the mechanical boundary conditions. The stress history ($\sigma(\mathbf{x},t)$), and in particular, residual stresses are solved for comparison with the experimental data.

1.3 Structure of the Problem and Organization of the Thesis

Figure 1.3 is a block diagram to demonstrate the physics of this thermomechanical problem. The heat produced through inelastic dissipation mechanisms is negligible in comparison to the heat drawn by forced cooling, therefore the thermal problem is uncoupled from the mechanical problem. In this way, the heat transfer problem is solved first to obtain the temperature field, $T(\mathbf{x},t)$, and then this temperature field is imposed on the succeeding mechanical analysis.

Since the main cause of stress generation is the thermal gradient within the sample, the accurate prediction of stresses relies firstly on the accurate solution of the heat transfer problem. The constituents of this problem are the boundary conditions (e.g., that imposed by the heat transfer coefficient, h), the initial condition (e.g., T_i) and the thermal properties

of the material such as thermal conductivity $k(T)$, specific heat $C_p(T)$ and density $\rho(T)$, which are the material parameters in the heat diffusion equation

$$\nabla \cdot (k(T)\,\nabla T) = \rho(T)\,C_p(T)\,\frac{\partial T}{\partial t} \tag{1.3}$$

As mentioned earlier, the temperature range during the casting of the $Zr_{41.2}Ti_{13.8}Cu_{12.5}Ni_{10}Be_{22.5}$ alloy used in this study is broad (typically from $\sim$ 1200 to 300 K) and k and C_p exhibit pronounced temperature dependence in this range. Due to the important role of the temperature dependence of these parameters in the problem, a detailed chapter is given in Appendix A that describes material properties and the study to measure them.

As seen on the block diagram, the evaluated $T(x,t)$ is then fed to the mechanical problem which also employs material data. The mechanical problem is solved with a constitutive model and the material properties needed become a larger set as the sophistication of the constitutive models increases. Note also that the boundary conditions during the processing of BMGs are more complicated than the traction-free surfaces of silicate glass tempering due to the interaction of BMGs with the mold. Finally residual stress prediction is made and compared with the experimental data. Chapter 2 gives a broad background of the mechanical constitutive models, namely, linear viscoelasticity concepts, the phenomenology of silicate glass tempering models and certain characteristic metallic glass features.

A series of studies have been performed for the first time (Aydıner et al. [11], Aydıner et al. [12], Aydıner and Üstündag [9] and Aydıner et al. [10]) to evaluate the thermal tempering of BMGs. While these articles were prepared, the available material data, in particular the high temperature values of the thermal parameters, progressively increased in time. In this thesis, however, the material data used for all calculations are unified with the material data

in Appendix A. For this reason, some slight discrepancies will be found when the results in these articles are compared with those in this thesis.

Chapter 3 describes an analytical-experimental study of a copper-mold-cast BMG plate, the same geometry employed for silicate glasses. On the experimental side, it is demonstrated for the first time that the crack compliance method is a highly effective technique to measure residual stresses in BMGs and is particularly suited to thermal tempering studies due to its ability to resolve through-thickness stress profiles. On the modeling end, a viscoelastic model for BMG is formulated for the first time making use of the equilibrium viscosity data as a function of temperature. Analysis is also carried out with a simple instant freezing model. It is concluded that copper mold casting, due to separation of the cast BMG from the mold, does not allow well defined analysis of the heat transfer problem. This precludes any detailed comparison of the stress results from the models and the measurements.

To remedy this problem, Chapter 4 presents an analytical-experimental study for which an alternative casting process is employed to determine and enhance heat transfer. Here, the BMG is melt in a stainless steel tube and the cooling is implemented by water quenching. This method presents a geometry change from a plate to a long cylinder. Agreement between the measured stresses (using the crack compliance method) and the model results is achieved within the accuracy of the thermal problem.

A related study is summarized in Appendix B, where a cylindrical stainless steel-BMG composite produced with a similar process is considered. In this case, the residual strains in the stainles stainless phase are measured with neutron diffraction and then related to thermal tempering.

Chapter 5 attempts to develop a structural model (the most advanced model in silicate

glass tempering) for the $Zr_{41.2}Ti_{13.8}Cu_{12.5}Ni_{10}Be_{22.5}$ alloy. In order to investigate the required material function, volumetric physical aging (structural relaxation) experiments are performed and presented.

Finally, Chapter 6 summarizes the main conclusions of the study and lists possible future work.

Chapter 2

Background

This chapter presents a broad background of the thermal tempering phenomenon by drawing upon literature from multiple fields. First, there are the thermal tempering theories for silicate glasses for which the process has proved useful for their mechanical performance, in particular, in glass plates. Roughly over a period of forty years, theories of thermal tempering evolved by gradually accounting for more complicated physics of the material behavior: from the theories with a simple instant freezing assumption (e.g. Aggarwala and Saibel [3]) to a theory that accounted for the temperature history (cooling rate) dependence of the viscoelastic behavior (Narayanaswamy [64]). This latter theory has been accepted as the *definitive* theory of thermal tempering in silicate glasses since it yielded good qualitative and reasonable quantitative agreement with experiments not only for residual stresses but also for stress evolution during quenching that could be measured in situ by photoelasticity. Hence, the silicate glass thermal tempering literature provides an obvious starting point considering behavioral similarities of silicate and metallic glasses. However, although it seems to comprise the essential physics of silicate glass tempering, the phenomenology of even the Narayanaswamy theory is arguable in terms of completeness. A broader framework is, therefore, considered here which will have elements from the polymer literature which is more extensive in viscoelastic phenomenology. The ideas here might help with a better

understanding of the metallic glass rheology.

On the other hand, the rheological literature of metallic glasses should be elaborated considering the material's unique features dissimilar to other amorphous materials. Metallic glass literature is indeed noticeably different in character. The lower glass formation ability of metallic glasses allows limited time to conduct viscoelastic experiments often with little confidence that the material has perfectly maintained its amorphous structure. Hence, viscoelastic behavior cannot be investigated to the same degree as in silicate glasses or polymers. For example, rheology of metallic glasses is often considered only in terms of *average* viscosity. Furthermore, the material has a pronounced nonlinear viscoelastic regime unlike silicate glasses. This is characterized by softening of the material due to deformation itself and considerable work has been focused on this *shear thinning* phenomenon, also in relation to formation of shear instabilities called *shear bands*.

In order to span this broad field in a sufficiently concise manner, concepts are introduced only to the extent they are needed in later discussions. The reader is referred to the numerous excellent sources cited throughout the text for additional details.

2.1 Linear Viscoelasticity Preliminaries

There are many good texts (e.g., by Ferry [33], Lakes [49], Christensen [25]) that cover the standard material of linear viscoelasticity. The concise coverage here will be confined to the integral formulation and will exclude the dynamic response. Assuming small deformations under isothermal and isobaric (more generally structure-preserving) conditions, linear viscoelastic constitutive behavior that relates stress and strain tensors in time is given by

$$\sigma_{ij}(t) = \int_{-\infty}^{t} C_{ijkl}(t-t') \frac{\partial \varepsilon_{kl}(t')}{\partial t'} dt' \tag{2.1}$$

or

$$\varepsilon_{ij}(t) = \int_{-\infty}^{t} J_{ijkl}(t-t') \frac{\partial \sigma_{kl}(t')}{\partial t'} dt' \tag{2.2}$$

where C_{ijkl} is the tensorial relaxation function and J_{ijkl} is the tensorial creep function. Thus, local stress history is related to the local strain history via the Boltzmann superposition which assumes linearity, translation-invariance and non-retroactivity (Gurtin and Sternberg [36]). To construct the boundary value problem for a body B, the remaining field equations are

$$\varepsilon_{ij} = \frac{1}{2} \left(\left. \frac{\partial u_i(\mathbf{x},t)}{\partial x_j} \right|_t + \left. \frac{\partial u_j(\mathbf{x},t)}{\partial x_i} \right|_t \right) \tag{2.3}$$

$$\left. \frac{\partial \sigma_{ij}(\mathbf{x},t)}{\partial x_j} \right|_t + f_i = 0 \tag{2.4}$$

namely, compatibility (2.3) and equilibrium (2.4) that preserve their form in linear elasticity and hold at all times. Using the equilibrium equation instead of the equation of motion—ignoring inertia term—assumes that the body is in quasi-static equilibrium at all times. If the body is initially undisturbed initial conditions are given by

$$u_i = \varepsilon_{ij} = \sigma_{ij} = 0 \quad for \quad -\infty < t < 0 \tag{2.5}$$

The boundary conditions on the surface of B, denoted by ∂B, take their usual form of either prescribed traction over ∂B_t with an outward-pointing normal vector $\mathbf{n}$ or prescribed displacement over ∂B_u, $\partial B_u + \partial B_t = \partial B$. Thus

$$\begin{aligned} \sigma_{ij}(\mathbf{x},t)\, n_j(\mathbf{x}) &= \hat{t}_i(\mathbf{x},t) \quad over \quad \partial B_t \\ u_i(\mathbf{x},t) &= \hat{u}_i(\mathbf{x},t) \quad over \quad \partial B_u \end{aligned} \tag{2.6}$$

More complicated boundary conditions can be conceived where a traction boundary, in time, turns into a displacement boundary or vice versa, yet such considerations are out of scope in this study where even the time dependence in (2.6) can be dropped for the considered problems.

When the constitutive equations are reduced to isotropic[1], linearly viscoelastic materials, it is logical to express material response through its shear and dilatation components. Hence, deviatoric stress $s_{ij} = \sigma_{ij} - \frac{1}{3}\sigma_{kk}\delta_{ij}$ is related to the deviatoric strain $e_{ij} = \varepsilon_{ij} - \frac{1}{3}\varepsilon_{kk}\delta_{ij}$ via

$$s_{ij}(t) = \int_{-\infty}^{t} \mathbf{G}(t-t')\frac{\partial e_{ij}(t')}{\partial t'}dt' \tag{2.7}$$

where $\mathbf{G}(t)$ is the shear relaxation modulus and, similarly, dilatational stress σ_{kk} is related to dilatational strain ε_{kk} by

$$\sigma_{kk}(t) = \int_{-\infty}^{t} \mathbf{K}(t-t')\frac{\partial \varepsilon_{kk}(t')}{\partial t'}dt' \tag{2.8}$$

where $\mathbf{K}(t)$ is the bulk relaxation modulus. Alternatively, creep formulation is given by

$$e_{ij}(t) = \int_{-\infty}^{t} \mathbf{J_1}(t-t')\frac{\partial s_{ij}(t')}{\partial t'}dt' \quad , \quad \varepsilon_{kk}(t) = \int_{-\infty}^{t} \mathbf{J_2}(t-t')\frac{\partial \sigma_{kk}(t')}{\partial t'}dt' \tag{2.9}$$

where $\mathbf{J_1}$ and $\mathbf{J_2}$ are the shear and bulk creep compliances, respectively. Explicitly, shear (bulk) relaxation modulus is defined by the time-dependent response of the material point to a step disturbance in shear (dilatational) strain normalized by the amplitude of the step. Shear relaxation modulus is demonstrated in parts (a) and (b) of Figure 2.1. Creep compliance definitions are obtained by swapping the terms stress and strain in the previ-

[1]Isotropy is well justified for silicate and metallic glasses. In the case of polymers, preferential aligning of molecule chains, e.g., due to melt injection, may cause anisotropy.

ous expression. For brevity, the discussion will be limited to the shear (bulk) relaxation formulation from this point onwards. On a phenomenological basis, relaxation moduli are

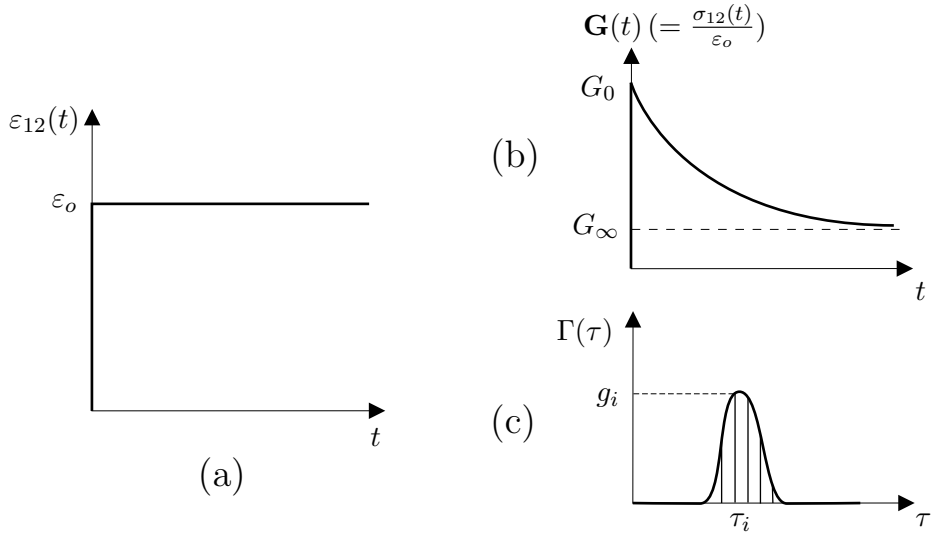

Figure 2.1: (a) Step disturbance in shear strain at $t = 0$. (b) Shear relaxation modulus $\mathbf{G}(t)$: stress response normalized by the magnitude of the step in strain. (c) Continuous relaxation spectrum $\Gamma(\tau)$, line spectrum; the set of all (g_i, τ_i).

expressed as a superposition of exponential decay functions

$$\begin{aligned} \mathbf{G}(t) &= G_\infty + (G_0 - G_\infty) \sum_i g_i \exp\left(-\tfrac{t}{\tau_i^s}\right) \\ \mathbf{K}(t) &= K_\infty + (K_0 - K_\infty) \sum_i k_i \exp\left(-\tfrac{t}{\tau_i^d}\right) \end{aligned} \tag{2.10}$$

where $G_\infty(K_\infty)$ is the infinite time (equilibrium) modulus, $G_0(K_0)$ is the instantaneous (elastic) modulus, $g_i(k_i)$ is the weight and $\tau_i^s(\tau_i^d)$ the time constant of the i^{th} relaxation process and the weights satisfy $\sum_i g_i = 1$ $(\sum_i k_i = 1)$. The set of all (τ_i^s, g_i) $((\tau_i^d, k_i))$ constitutes the line spectrum of the shear (bulk) relaxation modulus. Relaxation via a single time constant (single process) is the *Debye* relaxation. The idea presented by (2.10) can be extended to a continuous spectrum of relaxation times. Thus, e.g., for the shear

relaxation modulus the following expression is written

$$\mathbf{G}(t) = G_\infty + (G_0 - G_\infty) \int_0^\infty \Gamma(\tau) \exp\left(-\frac{t}{\tau}\right) d\tau \tag{2.11}$$

where $\Gamma(\tau)$ is the continuous spectra of relaxation times satisfying $\int_0^\infty \Gamma(\tau) d\tau = 1$. A symbolic plot of discrete and continuous spectrum of the shear relaxation modulus of Figure 2.1(b) is given in Figure 2.1(c). Numerical algorithms can be utilized to extract both types of spectra from relaxation modulus data[2] (e.g., see Tschoegl [87]). A simple alternative expression that can represent multiple-relaxation-time moduli (often reasonably well) is the stretched exponential function. This form is given by

$$\begin{aligned} \mathbf{G}(t) &= G_\infty + (G_0 - G_\infty) \exp\left[-\left(\tfrac{t}{\tau_s}\right)^{\beta_s}\right] \\ \mathbf{K}(t) &= K_\infty + (K_0 - K_\infty) \exp\left[-\left(\tfrac{t}{\tau_d}\right)^{\beta_d}\right] \end{aligned} \tag{2.12}$$

where $\tau_s(\tau_d)$ is *a mean* relaxation time and $\beta_s(\beta_d)$ is the stretching exponent that varies between 0 and 1. $\beta_s(\beta_d) = 1$ is obviously the Debye relaxation and the spectrum becomes broader as the value of the stretching exponent gets smaller.

2.2 Basic Linear Thermoviscoelasticity

The theory here refers to the framework introduced by Morland and Lee [60], which is restricted to a set of materials that are *thermorheologically simple*[3]. For these materials, characteristic viscoelastic functions measured at different temperatures (such as relaxation

[2] Yet, such depth is not meaningful (it may even be deceptive) when the material of concern does not preserve its structure, i.e., the relaxation time(s) change within the time span of the experiment.

[3] The term thermorheological simplicity has been introduced by Schwarzl and Staverman [77], another popular term for the same phenomenon is time-temperature superposition.

and creep moduli) exhibit only a pure shift—no change in shape—when they are plotted versus logarithm of time. Of course, being a purely phenomenological definition, such translational invariance is sought only within the accuracy of careful experiments. Figure 2.2(a) exhibits this phenomenon for the shear relaxation modulus, where $\mathbf{G}(t)$ measured *at* temperature T is denoted by $\mathbf{G}^T$. As shown in Figure 2.2(b), a reference temperature T_r with

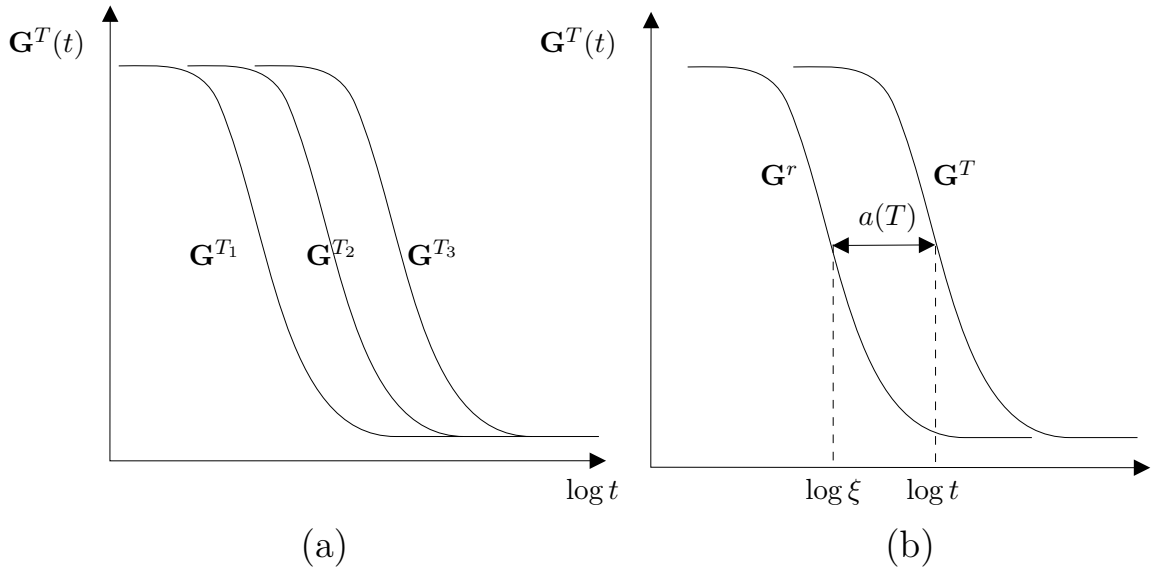

Figure 2.2: (a) Demonstration of thermorheological simplicity (time-temperature superposition) for shear relaxation modulus $\mathbf{G}^T(t)$ where T is the constant temperature of the measurement (here $T_1 > T_2 > T_3$). (b) Representation of $\mathbf{G}^T(t)$ with the reference (master) curve $\mathbf{G}^r$ measured at temperature T_r where ξ is the reduced time.

corresponding relaxation modulus $\mathbf{G}^r(\equiv \mathbf{G}^{T_r})$ can be chosen such that $\mathbf{G}^T$ can be represented by $\mathbf{G}^r$ and the shift function $a(T)$ that bears the separation between the two curves, defined as

$$a(T) = \frac{\tau_i^s(T)}{\tau_i^s(T_r)} \quad ,\forall i \tag{2.13}$$

Setting the notation $F(t) = \tilde{F}(\ln(t))$ for a function:

$$\tilde{\mathbf{G}}^T(\ln t) = \tilde{\mathbf{G}}^r(\ln t - \ln a(T)) = \tilde{\mathbf{G}}^r(\ln \frac{t}{a(T)}) \tag{2.14}$$

It follows that

$$\mathbf{G}^T(t) = \mathbf{G}^r(\xi) \quad , \quad \xi = \frac{t}{a(T)} \tag{2.15}$$

Hence $\mathbf{G}^T$ can be represented by the *master curve*, $\mathbf{G}^r$, only by allowing the time for the latter to proceed at a different pace. This latter time, denoted in (2.15) by the letter ξ, is called the *reduced time*, whose pace with respect to real time t is determined by the shift function $a(T)$. When the material experiences a temperature field that is, most generally, not uniform in time and space, the above definition of reduced time is generalized to

$$\xi(T(\mathbf{x}, t)) = \int_0^t \frac{1}{a(T(\mathbf{x}, t'))}\, dt' \tag{2.16}$$

With this definition, the Boltzmann superposition form of the constitutive law is preserved and the reader is referred to Morland and Lee [60] for the proof. Once more exemplifying for shear relaxation:

$$s_{ij}(\mathbf{x}, t) = \int_{-\infty}^{t} \mathbf{G}^r(\xi(\mathbf{x}, t) - \xi(\mathbf{x}, t')) \frac{\partial e_{ij}(\mathbf{x}, t')}{\partial t'}\, dt' \tag{2.17}$$

or in an easily derived alternative form

$$s_{ij}(\mathbf{x}, \xi) = \int_{-\infty}^{\xi} \mathbf{G}^r(\xi - \xi') \frac{\partial e_{ij}(\mathbf{x}, \xi')}{\partial \xi'} d\xi' \tag{2.18}$$

Hence, compared to the isothermal constitutive equations, all that is needed is to replace time by reduced time and the characteristic function with the master curve. The remaining field equations are again compatibility (2.3) and equilibrium (2.4) and it is emphasized that they hold in real time t. Unfortunately, when the temperature field varies with spatial coordinates, their form is not preserved upon converting the independent variable to reduced

time ξ. An important consequence is that the *Correspondence Principle* (see, e.g., Gurtin and Sternberg [36]) is no longer useful. This principle, given non-time-varying boundary conditions, allows obtaining the solution for a linear viscoelasticity boundary value problem from the problem's solution in linear elasticity, i.e., the solution of the problem with the linear elastic constitutive law. It can be seen through the examination of the field equations that the farthest point the Correspondence Principle would be valid is a temperature field that varies in time but homogeneous in space. For example, sufficiently slow cooling of a hot thermorheologically simple viscoelastic body may be approximated like this (see, e.g., Scherer and Rekhson [76]). Since the thermal tempering problem is certainly not in this class, further elaboration on this solution method is not necessary. Actually, semi-analytical solutions to thermoviscoelastic problems with non-uniform temperature fields are limited (e.g., Muki and Sternberg [62]) only to a few cases with simple geometries and often under simplifying assumptions such as elastic (instantaneous) bulk response. The thermoviscoelastic tempering solution for a uniformly cooled infinite plate by Lee at al. [50] is in this group detailed in the next section.

2.3 Thermoviscoelastic Theory of Silicate Glass Tempering

The solution by Lee et al. [50] is for the simple boundary value problem where an infinite (length and width $\gg$ thickness) glass plate above its glass transition, yet viscous enough to retain its shape is cooled homogeneously from both sides via air convection. The framework introduced above has been used to obtain semi-analytical results by assuming that the dilatational response is linear elastic (instantaneous). Thermal strain, $\varepsilon_\theta(\mathbf{x},t) = \alpha\,(T(\mathbf{x},t) - T(\mathbf{x},0))$, is introduced as an isotropic eigenstrain in the dilatational constitutive behavior

the same way it is done in thermoelasticity (e.g., Boley and Weiner [15]). Hence

$$\sigma_{kk} = K_0(\varepsilon_{kk}(\mathbf{x}, t) - 3\varepsilon_\theta(\mathbf{x}, t)) \tag{2.19}$$

where $K_0 = 3K$, and K is the elastic bulk modulus.

This equation, along with equations (2.16), (2.17) and an appropriate shift function $a(T)$ define the constitutive behavior. The solution of this particular boundary value problem is not reproduced here since it is one of the problems that are considered for the thermal tempering of bulk metallic glasses in this thesis. The Finite Element Method (FEM) is generically employed throughout this study to solve the boundary value problems specifying constitutive laws also since problems other than the infinite plate case are too complicated for semi-analytic solutions and require numerical solutions[4].

The instant freezing theory (e.g., Aggarwala and Saibel [3]) can be deduced from the viscoelastic theory by assigning an instant freezing temperature such that the material becomes a non-viscous fluid above it and an elastic solid below it. Therefore, glass transition is artificially shrank to a point. Under certain operating conditions, it is shown to yield good accuracy for the final residual stresses, though obviously, it does not comprise the physics to predict the correct evolution of stresses.

Now, let us worry about the validity of the assumed elastic bulk behavior. For silicate glasses, the partial justification behind this and another commonly used assumption for simplifying viscoelastic problems, $\mathbf{K}(t) \gg \mathbf{G}(t)\,, \forall t$, is demonstrated in Figure 2.3 that has been adapted from Rekhson and Rekhson [72]. First, the bulk relaxation is seen to

[4]The solution of Lee et al. [50], too, requires numerical routines to tackle the coupled time integration of the constitutive law and the equilibrium equation which is not entirely trivial (this is the reason the term semi-analytic has been adopted for such solutions). Indeed, their solution method did not give enough accuracy resulting in erroneous results later corrected by Narayanaswamy and Gardon [65]

be more sluggish than the shear relaxation, and second, the equilibrium modulus K_∞ is nonzero, unlike isochoric shear relaxation which is generally observed to continue until complete relaxation, i.e., $G_\infty \simeq 0$ and $G_0 = 2\mu$. Rekhson and Rekhson reported $\tau_i^d/\tau_i^s = 6$ and $K_0/K_\infty = 3$. Then, they calculated the uniaxial relaxation modulus $\mathbf{E}(t)$ and biaxial

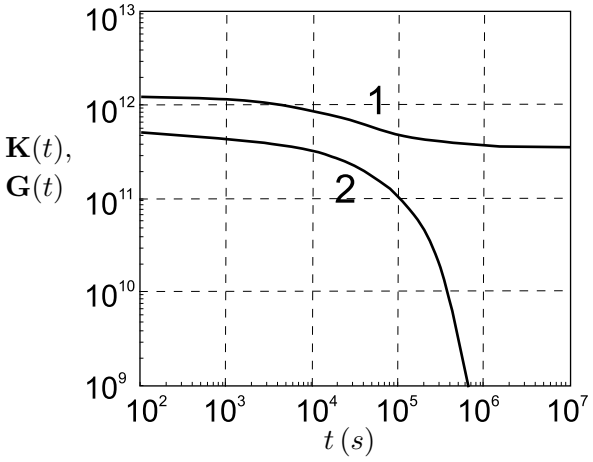

Figure 2.3: Bulk relaxation modulus $\mathbf{K}(t)$ (curve 1) in comparison to shear relaxation modulus $\mathbf{G}(t)$ (curve 2) for silicate glass at 473°C (adapted from Rekhson and Rekhson [72]).

relaxation modulus $\mathbf{M}(t)$ whose elastic counterparts are E and $\frac{E}{1-\nu}$, respectively, for the two cases simplified with the aforementioned assumptions and the *exact* case for which $\mathbf{K}(t)$[5] shown in Figure 2.3 is used. They observed that neither of the two assumptions yield particularly closer results to the exact solution and both seem reasonable for the problems of uniaxial and biaxial loading. The biaxial relaxation modulus is the viscoelastic function that relates in-plane stress to in-plane strain for the one-dimensional (i.e., fields (stress, temperature, etc.) vary only in the thickness direction) infinite plate problem. So, this study of Rekhson and Rekhson specifically targets the plate tempering problem with the treatment for biaxial modulus.

To draw conclusions for the present study, if metallic glass demonstrates similar charac-

[5]The bulk relaxation modulus curve here has been inverted from creep compliance measurements.

teristics, the elastic bulk response appears to be a good assumption. Unfortunately, there is lack of data from metallic glasses on this issue. For this reason, the present study limits itself to an elastic bulk deformation. In addition, the relatively low pressures employed in BMG casting may be expected to limit the inadequacy of ignoring bulk relaxation.

There is another significant shortcoming of the thermoviscoelastic theory that will be discussed starting in the next section, which led to the *structural theory* of tempering (Narayanaswamy [64]): The thermoviscoelastic theory makes use of the relaxation data for stabilized glass, which was shown to be indeed thermorheologically simple (see, e.g., Kurkjian [48]). Stabilized glass is a term in silicate glass terminology for liquid at metastable equilibrium. However, rapidly-cooled glass deviates from metastable equilibrium and mere temperature dependence does not describe the behavior well. Rather, it is required to account for the dependence of structure on *temperature history*.

2.4 Temperature History Dependence of Structure

The general term *structure* is used in the title since the complete set of thermodynamic and kinetic properties of a glassy material, such as enthalpy, entropy, volume and viscosity are influenced by the imposed temperature history around glass transition. However, in the context of the thermal stress problem, attention is essentially constrained to specific volume, v, and viscosity (more specifically relaxation times). An important parameter for the following discussion is the linear coefficient of thermal expansion (CTE), which for isotropic expansion, is given by

$$\alpha = \frac{1}{3v}\left(\frac{\partial v}{\partial T}\right)_P \simeq \frac{1}{3v(0)}\left(\frac{\partial v}{\partial T}\right)_P \tag{2.20}$$

where $v(0)$ is the specific volume at the beginning ($t = 0$) of the process and the second part is valid for small volumetric changes[6]. Also, in terms of isotropic thermal strain ε_θ, CTE definition becomes

$$\alpha = \left(\frac{\partial \varepsilon_\theta}{\partial T} \right)_P \tag{2.21}$$

Now, let us formally phrase the question that we currently seek an answer for: "Consider a traction-free particle of glassy material under atmospheric pressure. Given, temperature history, $\underset{t=0}{\overset{\infty}{T}}$, imposed on it, what is the specific volume response of the particle in time, $v(t)$?"

The question has a nontrivial answer about the glass transition region, due to the kinetic nature of the glass transition phenomenon. This is demonstrated in the example shown in Figure 2.4(a) that considers the volumetric response to cooling from above melting temperature to room temperature with two different rates denoted by $\dot{T}_1$ and $\dot{T}_2$, such that $\dot{T}_2 > \dot{T}_1$. As the cooling rate is increased, the material has less time for structural arrangements that result in volume compaction and the glass transition is shifted to higher temperatures. Also, the curve of the case where crystallization occurs at melting temperature T_m is plotted for reference. For a rapidly cooled glass forming material that evades crystallization at and under T_m, the region between T_m and glass transition is called the *supercooled liquid region*[7]. In the supercooled liquid region, the material is in *metastable equilibrium*; metastable, since real thermodynamic equilibrium is achieved with crystallization that is averted in laboratory time scales by sluggish kinetics. The CTE here is denoted by α_l, where subscript 'l' is for 'liquid'. On the other hand, the low temperature region to the left of glass transition region in Figure 2.4 is called the *glassy region* and the CTE

[6]For clarity, the factor 3 will be omitted in the volume expansion expressions in this chapter that follow. In these expressions, α should be understood as the volumetric CTE that is three times the linear CTE.

[7]This terminology is somewhat particular to metallic glass literature.

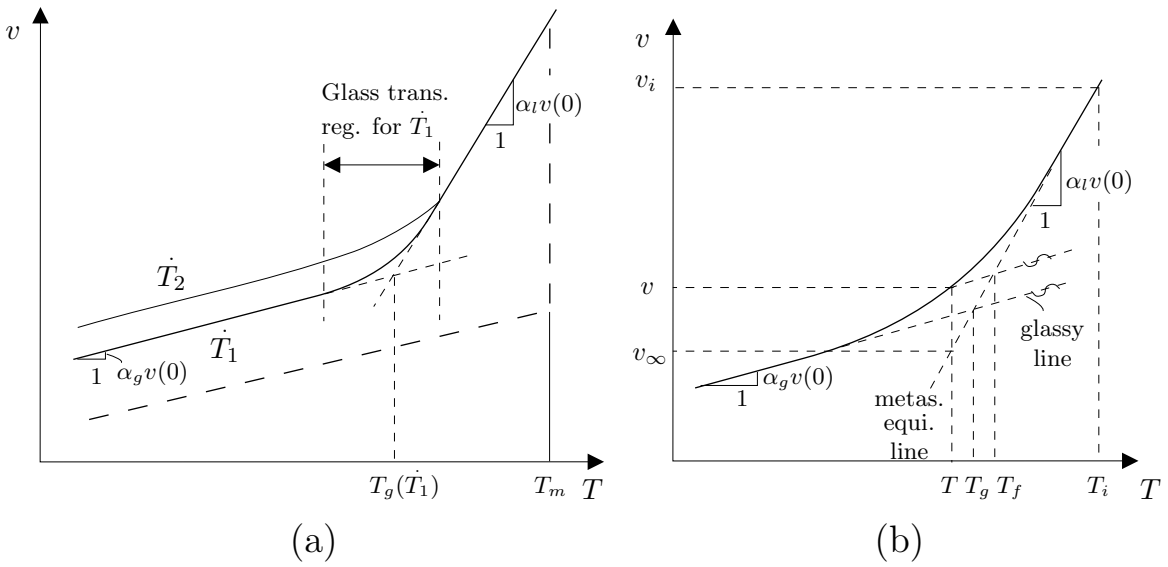

Figure 2.4: (a) Specific volume (v) vs. temperature (T) curves traced by a glassy material for cooling rates $\dot{T}_1$ and $\dot{T}_2$, $\dot{T}_2 > \dot{T}_1$. The crystal curve (dashed) is also provided for reference. The glass transition region is indicated for the $\dot{T}_1$ case between supercooled liquid and glassy regions. (b) Zoom of the glass transition region for the $\dot{T}_1$ case.

here is denoted by α_g. Typically, the value of α_l is 1.5 to 3 times that of α_g. For the sake of discussion, let us assume that both α_l and α_g are constant values ignoring their weak variation in supercooled liquid and glassy regions, respectively.

As shown Figure 2.4(a), the glass transition region is where the CTE decays from α_l to α_g while its span and nature depend on the cooling history. Figure 2.4(b) is a zoom of the glass transition region for the $\dot{T}_1$ cooling rate. In this plot, let us call the line that passes through (but not limited to) the points in the supercooled liquid region, the *metastable equilibrium line*. Likewise, the line that passes through the points in the glassy region will be the *glassy line*. Accordingly, *the glass transition temperature*, T_g, is defined as the temperature at the intersection of these two lines. This definition is somewhat more rigorous than the engineering definition as the temperature that corresponds to a fixed value of viscosity ($= 10^{13}\,\mathrm{Pa}\cdot\mathrm{s}$). The definition of fictive temperature, T_f, is also demonstrated in Figure 2.4(b) and is one of the commonly used *disorder* parameters to quantify the

deviation from metastable equilibrium. Verbally, T_f corresponds to a point (T, v) at the intersection of the line that is extrapolated from (T, v) with the glassy slope $\alpha_g v(0)$ and the metastable equilibrium line. It should now be apparent that T_f equals to the actual temperature T in the supercooled liquid region, then starts to lag behind it in the glass transition region and finally settles to the constant value of T_g at the onset of glassy region. The volumetric departure from metastable equilibrium at point (T, v), denoted by Δv, can easily be expressed in terms of T_f as

$$\Delta v = v - v_\infty(T) = \alpha_s v(0)(T_f - T) \tag{2.22}$$

where $\alpha_s = \alpha_l - \alpha_g$ is called the *structural CTE* and $v_\infty(T)$ is the metastable equilibrium volume at temperature T. More explicitly, it is the specific volume the material would tend to as $t \to \infty$ in an isothermal hold at temperature T. Now, as a step to formulate an answer to our main question, consider some simple temperature step experiments. In these, the glassy material is allowed to achieve metastable equilibrium, and then its temperature is altered abruptly by ΔT.

The experiment for upward and downward jumps of ΔT to a common target temperature T is shown in Figure 2.5(a). An important assumption on material behavior is that the material gives an instantaneous response to the temperature jump with the glassy CTE, hence volume contracts for the downward jump (expands for the upward jump) by $\alpha_g v(0)\Delta T$ instantly. This is due to the fact that glassy expansion represents stretching of interatomic bonds, much like the one in a perfect crystalline lattice with no viscous mechanisms. The time dependence is in the remainder of the isothermal contraction (expansion) of $\alpha_s v(0)\Delta T$ magnitude. This is called *structural relaxation* and, the normalized structural relaxation

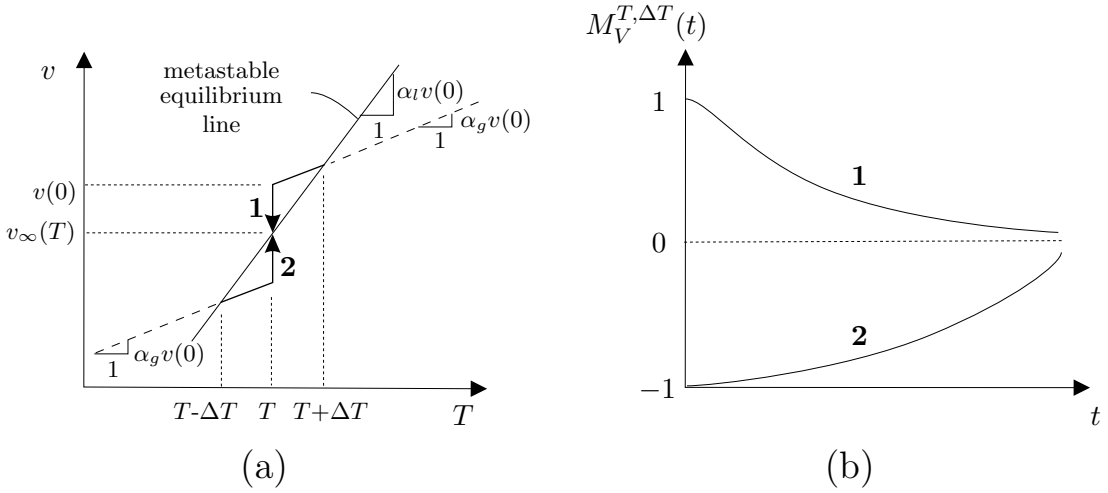

Figure 2.5: (a) Upward and downward temperature jump experiments to a target temperature T on the $v - T$ plot; instantaneous response with the glassy slope and following time-dependent relaxation to the equilibrium volume for downward (path **1**) and upward (path **2**) jumps. (b) Structural relaxation function $M_V^{T,\Delta T}(t)$ for downward(**1**) and upward(**2**) jumps.

function of Figure 2.5(b) is given by

$$M_V^{T,\Delta T}(t) = \frac{v(t) - v_\infty(T)}{v(0) - v_\infty(T)} = \frac{T_f(t) - T}{\Delta T} \tag{2.23}$$

where T is the temperature of the isothermal hold and ΔT is the jump to it. The sign of ΔT is positive for an upward jump and vice versa. To demonstrate the ΔT dependence, the asymmetry of the structural relaxation functions $M_V^{T,\Delta T}(t)$ and $M_V^{T,-\Delta T}(t)$, is pictured in Figure 2.5(b). The reason for this asymmetry is the dependence of the relaxation times on the dependent variable v itself. This, by definition makes the process nonlinear. In the upward jump experiment, the material obviously starts from a more compact structure in comparison to the downward jump experiment. In fact, the specific volume in the former process is always less than $v_\infty(T)$ whereas the opposite is true for the latter. This means, the relaxation times are always bigger in the upward jump experiment making it more sluggish. On the other hand, the relaxation becomes slower during the downward jump experiment

as the structure becomes more compact and therefore it is called *autoretarded*. Obviously, the opposite is true for the upward jump experiment and it is called *autocatalytic*.

To eliminate the dependence on ΔT, Narayanaswamy [63] has written the function in the limit sense

$$\mathbf{M}_V^T(t) = \lim_{\Delta T \to 0} M_V^{T,\Delta T}(t) \tag{2.24}$$

which is called the structural relaxation modulus. Now, analogous to the time-temperature superposition, a reference temperature, T_r is chosen and the structural relaxation modulus *for the equilibrium liquid* at this temperature is taken to be the master curve, denoted by $\mathbf{M}_V^r$. Through the reduced time concept, any $M_V^{T,\Delta T}$ can be represented as

$$M_V^{T,\Delta T}(t) = \mathbf{M}_V^r(\xi) \tag{2.25}$$

provided that the shift function depends not only on temperature but structure (specific volume) to account for the aforementioned nonlinearity. Expressing in terms of fictive temperature to reproduce Narayanaswamy's theory, the shift function is given by

$$\xi(T, T_f) = \int_0^t \frac{1}{a(T(t'), T_f(t'))} dt' \tag{2.26}$$

This generalization of the time-temperature superposition is called the time-temperature-structure superposition[8]. Narayanaswamy [63] proposed the following form

$$a(T, T_f) = \exp \frac{Q}{R} \left(\frac{x}{T} + \frac{1-x}{T_f} - \frac{1}{T_r} \right) \tag{2.27}$$

[8]The formal justification of the time-temperature-structure superposition by demonstrating shape preservation in stress relaxation experiments is even more challenging. One has to do experiments at different Δv's for each temperature which is only possible when the time scale of structural relaxation is much bigger than that of shear relaxation. This allows taking snap shots of the material with stress relaxation experiments as it isothermally approaches equilibrium.

where $0 \leq x \leq 1$, and for $x = 1$, Arrhenius type dependence is recovered by which this relation has been inspired. The parameter x determines the relative weight of temperature and fictive temperature (deviation from equilibrium) on the viscosity of the material.

With the convolution of step functions assuming linear superposition, the response to an arbitrary temperature history up to time t, $\underset{t=0}{\overset{t}{T}}$, starting from equilibrium material at specific volume v_i in Figure 2.4(b) may be formulated as follows:

$$v(t) = v_i + \alpha_l(T(t) - T_i) - \alpha_s \int_0^t \mathbf{M}_V^r(\xi(t) - \xi(t')\frac{\partial T}{\partial t'}dt' \tag{2.28}$$

where the first two terms yield the metastable equilibrium volume at time t and the last term is Δv, deviation from metastable equilibrium volume. Thus, once more, the kernel function, $\mathbf{M}_V^r$, can conveniently be kept constant bearing all the structure and temperature dependence on reduced time.

Narayanaswamy derived the formal relation for T_f from the volumetric formulation (2.28) and the relation between Δv and T_f (2.22) as

$$T_f = T - \int_0^t \mathbf{M}_V^r(\xi(t) - \xi(t')\frac{\partial T}{\partial t'}dt' \tag{2.29}$$

Therefore, it is indeed a matter of taste to use T_f or Δv as the disorder parameter which lumps the effect of entire temperature history on the relaxation times. These theories with essentially identical phenomenology to explain structural relaxation have been reviewed by McKenna and Simon [59] and attributed to Tool [86], Narayanaswamy [63], Moynihan et al. [61], and Kovacs at al. [47], the last one making use of Δv and the others of T_f. Narayanaswamy's work is focused here due to its use in the definitive thermal tempering study of silicate glasses (Narayanaswamy [64]). Through his generalization of T_f with

equation (2.29), problems encountered with single relaxation time description of Tool (such as crossover effect, see, e.g., Ritland [74]) are resolved. Actually, the theory does not require the introduction of T_f since everything can be formulated through specific volume if it were not for the Arrhenius-relation-inspired shift function (2.27).

2.5 Structural Theory of Tempering

The structural theory (Narayanaswamy [64]) is then formulated by (i) the structure dependent shift function (equation (2.27)), (ii) reduced time (equation (2.26)), (iii) convolution of the structure parameter, T_f, over time with the kernel $\mathbf{M}_V^r$ (equation (2.29)), and (iv) the following expression for thermal strain that is easy to see on Figure 2.4(b)

$$\varepsilon_\theta = \alpha_g \left(T(\mathbf{x},t) - T_i\right) + \alpha_s \left(T_f(\mathbf{x},t) - T_i\right) \tag{2.30}$$

Alternatively, the expression of coefficient of thermal expansion α that depends on thermal history can be derived simply taking the temperature derivative (equation (2.21)) as

$$\alpha = \alpha_g + \alpha_s \frac{\partial T_f(\mathbf{x},t)}{\partial T} \tag{2.31}$$

In this theory, the effect of thermal strain on stresses are still through the elastic dilatational response given by equation (2.19). Thus, the addition of structural model over the thermoviscoelastic one is twofold: (i) the stress generating thermal strain becomes dependent on structure as depicted by any of the two equations above; (ii) via the T_f dependent shift function relaxation times depend on the structure. Narayanaswamy reports that the effect of the former is much more pronounced for the residual stresses. These stresses, simply put,

are due to the freezing of glass of different densities (or residual 'free volume's as introduced in next section) across the plate. Since the surface is cooled faster, it will attain a lower density.

In this theory, there is no coupling between the local stress state at the material point and the thermal strain that depends on the thermal history. In other words, the thermal strain history a material point will experience is fixed once its temperature history is given regardless of whether it is inside a body or it is a traction-free small particle. This deficiency though is consistent with the assumption of elastic dilatational response.

For example, a more complete theory, developed by Losi and Knauss [52], allows the coupling between pressure and thermal response by defining the mechanical effect of temperature change through 'thermal pressure' given by

$$\hat{p} = K_\infty \, \alpha_l \Delta T \tag{2.32}$$

Then the dilatational law is written in its creep form as

$$\varepsilon_{kk}(t) = \int_{-\infty}^{t} \mathbf{J_2}(\xi(t) - \xi(t')) \frac{\partial(\sigma_{kk} + \hat{p})(t')}{\partial t'} dt' \tag{2.33}$$

2.6 Free Volume and Vitreloy 1 Viscosity

Free volume, v_f, is a phenomenological parameter that quantifies the amount of vacancies present in glassy materials. In free volume based theories, the viscosity of the material is expressed as a function of free volume and other parameters such as temperature, pressure, strain rate, etc., that affect the relaxation time of the material via their influence on the free

volume. With statistical considerations, Cohen and Turnbull [27] formulated the viscosity

$$\eta = \eta_0 \exp(b\frac{v_m}{v_f}) \tag{2.34}$$

where v_f is the average free volume per atom and $b\,v_m$ is the critical volume for flow. This equation was formerly derived empirically by Doolittle from experiments on hydrocarbon liquids (see, e.g. Doolittle [30]). Williams, Landell and Ferry [90] then showed that the viscosity dependence of most glass-forming substances can be described by the Doolittle equation and that the free volume is given by

$$v_f = v_{f,ref} + \alpha_s v_m (T - T_{ref}) \tag{2.35}$$

where T_{ref} is a reference temperature, and $v_{f,ref}$ is the corresponding free volume. Setting T_{ref} as the glass transition temperature T_g, they obtained the 'universal' value of fractional free volume (v_f/v_m) as 0.25% at T_g which is valid for a large set of amorphous materials. If T_{ref} is taken as the kinetic freezing temperature, denoted by T_0, at which free volume becomes zero, equations (2.34) and (2.35) yield the Vogel-Fulcher-Tammann (VFT) equation

$$\eta = \eta_0 \exp(\frac{C}{T - T_0}) \tag{2.36}$$

where C is a constant. The viscosity data of Vit.1 are successfully fit with this equation and are used in the latter chapters for implementing the thermoviscoelastic theory to Vit.1. For the purpose of discussion here, only the regressed value of constant C is important, yet, it is worth noting that in the original references (see, e.g., Waniuk et al. [89]) for Vit.1, C is taken as D^*T_0 where D^* is the fragility parameter introduced by Angell [5]. The values

of T_0 and D^* for Vit.1 are 412.5 K and 18.5, respectively, and this alloy is called a *strong* liquid.

2.7 The Matsuoka Model for the Nonequilibrium State

Nonequilibrium means deviation from the metastable liquid, as detailed in Section 2.4. In his treatment for polymers, Matsuoka [58], by cooperative domain and configurational entropy concepts similar to Adam and Gibbs [2] first derives the Adam-Gibbs equation[9]. Then he states that the Adam-Gibbs equation is valid both for equilibrium and nonequilibrium states. His derivation with the equilibrium assumption leads to a shift function identical to that given by the VFT equation. For the nonequilibrium state, first, he criticizes the treatment of Narayanaswamy given by equation (2.27) since a good fit to the data in a relatively broad temperature interval cannot be obtained without changing activation energy Q and the parameter x. Instead, he argues that the configurational entropy of the nonequilibrium state at temperature T (i.e., $T_f\,(> T)$) is equal to the configurational entropy of the equilibrium liquid at its fictive temperature T_f. Then via the Adam-Gibbs equation he obtains

$$a(T, T_f) = \exp\left[C\left(\frac{1}{T}\frac{T_f}{T_f - T_0} - \frac{1}{T_{ref} - T_0}\right)\right] \tag{2.37}$$

where T_0 is again the kinetic freezing temperature and the above equation reverts to the VFT shift function for $T_f = T$. At this point, for the treatment in Chapter 5, it is emphasized that the constant C is unchanged from its value in the equilibrium VFT fit. Also, according to this theory, it is easy to see that the fractional free volume for the nonequilibrium state

[9]Detailed description of this set of theories is out of the scope of this thesis and the reader is referred to the original references.

is equal to

$$\frac{v_f}{v_m} = \alpha_s \left(T_f - T_0\right) \frac{T}{T_f} \tag{2.38}$$

2.8 Shear Thinning of Vitreloy 1

At high strain rates and low temperatures, metallic glasses deform in the non-Newtonian regime, i.e., the relaxation times decrease due to the deformation itself (Lu et al. [54], Johnson et al. [43]). The effect is exemplified on a figure reproduced from Lu et al. that plots the stress-strain response of the material for a series of strain rates at a constant temperature $T = 643$ K. At the beginning of the deformation, the material is Newtonian, and in this case, the stress response would settle to $\sim \eta\dot{\varepsilon}$ where η is the Newtonian viscosity. This is the case for $\dot{\varepsilon} = 2.0 \times 10^{-4}\,\mathrm{s}^{-1}$ on Figure 2.6. For the strain rates of $\dot{\varepsilon} = 5.0 \times 10^{-3}\,\mathrm{s}^{-1}$ and $\dot{\varepsilon} = 3.2 \times 10^{-2}\,\mathrm{s}^{-1}$, the internal relaxation time of the material decreases in time and the overshoot phenomenon occurs that results in a smaller *equilibrium* viscosity and a final stress value as seen in this figure. If the strain rate is higher, then the material fails by shear banding via localized deformation which is the case for $\dot{\varepsilon} = 3.2 \times 10^{-2}\,\mathrm{s}^{-1}$.

The three regimes in deformation for Vit.1 as a function of strain rate and temperature are shown in Figure 2.7. Note, however, this figure considers the steady state response of the material for which the experiments are carried out at a constant strain rate and temperature. The rapidly varying temperature and strain rates in the thermal tempering problem would require the transient response, more specifically, the effect of deformation history on the shift function.

Lu et al. modeled the transient (and steady-state) response with an empirical fictive stress model. Johnson et al.'s treatment is more prone to be incorporated into the reduced time models of thermoviscoelasticity since there the formulation is pursued by adding a

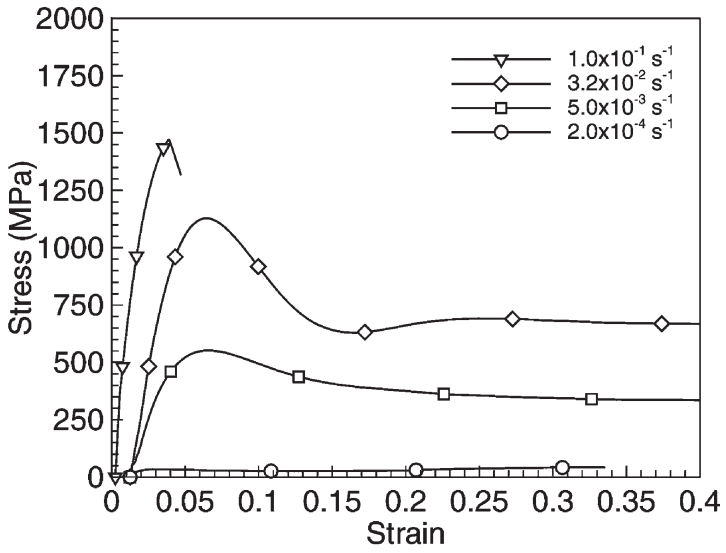

Figure 2.6: Effect of strain rate on the uniaxial stress-strain behavior of Vit.1 at temperature $T = 643$ K. The stress-strain curves have been shifted to the right to avoid overlapping curves of similar shapes and sizes (reproduced from Lu et al. [54]).

strain rate contribution to free volume. Hence, the free volume based shift function can easily be modified. Unfortunately, however the work of Johnson et al. considers primarily the equilibrium (steady-state) viscosity for constant strain-rate deformation.

In the present study, the effects of shear thinning in the non-Newtonian regime are not considered with the following justifications:

- Reasonable agreement for residual stresses are obtained with a linear viscoelastic model (Chapter 4).

- In the thermal tempering problems considered in this thesis, the glass transition region is traversed at 10–100 K/s and the material has limited time to go to the non-Newtonian regime. (Recall the 'short' time response in all experiments plotted in Figure 2.6 is within the Newtonian regime.)

- In the present study, the transient stresses around glass transition are typically smaller

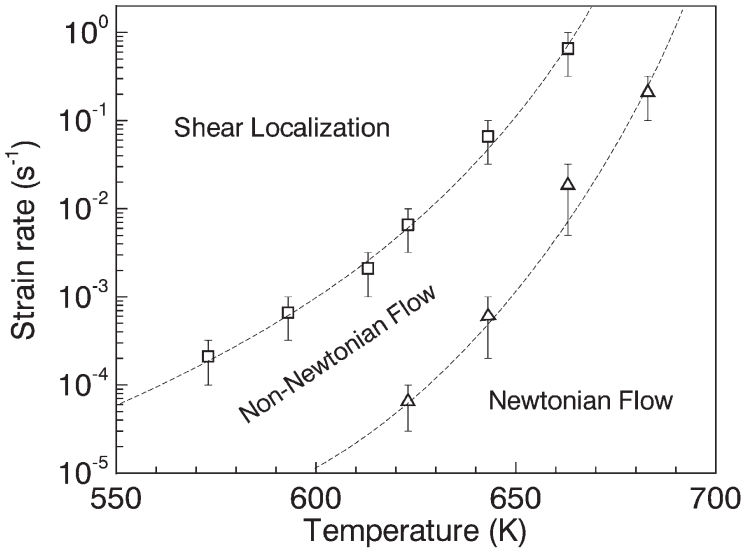

Figure 2.7: The boundaries between the three distinct modes of deformation for Vit.1. Two boundaries are shown, one for transition from homogeneous deformation to inhomogeneous deformation and the other from Newtonian to non-Newtonian flow (reproduced from Lu et al. [54]).

than 100 MPa (Section 5.4). In comparison, the stress levels in Figure 2.6 are much higher.

- The low level of measured temper stresses (maximum about ~ 400 MPa) in comparison to the yield strength of the material (1.9 GPa) justifies ignoring shear banding at low temperatures. In addition, no experimental evidence of shear bands have ever been observed in the produced samples.

- To incorporate the effect of strain rate history into the shift function poses a difficult problem.

On the other hand, the last item defines an interesting problem for future work.

Chapter 3

Modeling and Measurement of Residual Stresses in a Bulk Metallic Glass Plate

3.1 Introduction

The BMG processing typically involves casting an alloy into a mold followed by severe quenching. This procedure can lead to large thermal gradients due to the low thermal conductivity of BMG. In addition, during glass transition the alloy exhibits large changes in its viscosity within a small temperature range. All of these parameters can lead to "thermal tempering" which generates compressive surface residual stresses balanced with mid-plane tension.

A similar phenomenon was observed previously in silicate glasses (Gardon [34]). Thermal tempering in these glasses was mostly studied for a certain initial boundary value problem: an infinite plate at a uniform initial temperature convectively cooled from both sides. The resulting stress profile was roughly parabolic where compression on the surface(s) was balanced by tension in the interior. First theories made use of the instant freezing assumption (see, e.g., Aggarwala and Saibel [3]) that presumed the material behaves as a non-viscous fluid above its glass transition temperature and as a linear elastic solid below it. This sim-

plistic approach required only the glass transition temperature as the rheological input and ignored the details of the glass transition range and its cooling rate dependence as well as any stress relaxation below that range. As described in Chapter 2, the theory eventually evolved with the necessary material functions (e.g., relaxation and structural moduli) (Narayanaswamy [64]) such that any geometry could be handled with finite element modeling (e.g. Soules et al. [81], Daudeville and Carre [29]).

In this chapter, the instant freezing assumption is invoked first to obtain estimates of the residual stresses generated by this thermal tempering. Next, the only available viscoelastic data on the BMG alloy used here, its equilibrium viscosity as a function of temperature, is employed to develop the first viscoelastic model of thermal tempering in BMGs. The model predictions are then compared to residual stress data collected from a cast BMG plate using the crack compliance method.

3.2 Specimen Preparation

A $Zr_{41.2}Ti_{13.8}Cu_{12.5}Ni_{10}Be_{22.5}$ (Vit.1$^{\text{TM}}$) plate is considered in this study that is cast into a large copper mold, initially at room temperature[1]. This plate is nominally 150 mm long, 100 mm wide and 8.25 mm thick. The total thickness of the copper mold is 50.8 mm, hence, there lies a 21.28 mm thick copper section on each side of the BMG plate in the out-of-plane direction. Due to the proprietary nature of the process, only details relevant to this publication are discussed here. The alloy melt was fed into the copper mold at low pressure by vacuum assistance. A solid skin of Vit.1 likely forms at the cavity surfaces as the molten alloy flowed into the mold. Filling up the mold is estimated to take 2–3 seconds.

[1] Casting into metallic molds is the typical production method for BMG parts and one of the advanatages of BMGs over crystalline alloys lies in this process. BMGs can be cast into intricate shapes with fine dimensional tolerances similar to plastics.

The feeding pressure is kept for another 10 seconds to allow sufficient solidification of the plate such that it could be retained in the mold cavity. Final cooling to room temperature is achieved by quenching the mold in water at room temperature.

3.3 Modeling of Thermal Tempering

3.3.1 Instant Freezing Model

The name of the analysis originates from the assumption that glass abruptly solidifies at its glass transition temperature, T_g. Here, glass is treated as an elastic solid below this temperature and as a non-viscous fluid that cannot support shear above it. Also, the plane-stress condition in the large plate geometry (zero normal stress in one direction along the thickness) does not allow the fluid to feel pressure, either[2]. The first correct solution has been obtained by Indenbom [42] in 1954.

During quenching, the surface of the material will cool to T_g first, and here, the 'freezing front' will initiate and then move towards the mid-plane as the temperature of consecutive layers drop to T_g. Making the classification of Gardon [34] in the context of this model, the stresses that are generated until freezing front reaches the center are the *solidification stresses* and the rest that are due to the decay of the temperature profile in the now-elastic plate are the *temperature equilization stresses*.

Figure 3.1 demonstrates the typical shape of the resulting in-plane residual stress profile across the plate thickness. In-plane coordinates are X and Y while Z is the out-of-plane coordinate whose origin is at the mid-plane. Thermal-tempering-induced residual stresses are equibiaxial in the X-Y plane for this infinite plate problem.

[2]This is the precise reason instant freezing model can be classified as a plate tempering model and will not apply for, say, other simple geometries like long cylinder and sphere.

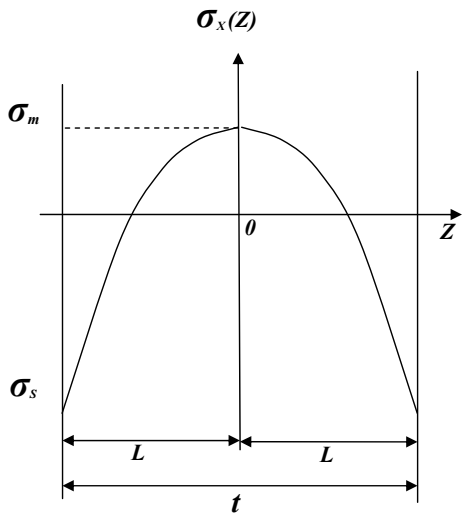

Figure 3.1: A typical residual stress profile across the thickness of a large plate due to thermal tempering: surface compression (σ_s) is balanced with mid-plane tension (σ_m). The in-plane stresses are equibiaxial and function of the thickness coordinate (Z) only.

The instant freezing model solution is developed for the convective cooling problem of silicate glass tempering. Accordingly, the heat transfer on the surface is given by [41]:

$$Q = h(T_s - T_a) \tag{3.1}$$

where, the heat flux (Q) is proportional to the differential between the surface temperature (T_s) and the temperature of the cooling medium (T_a) and the constant of proportionality is the heat transfer coefficient, h. To obtain a closed form solution for stress, the temperature solution is approximated as the first term of the Fourier series solution (see e.g., Brown and Churchill [16], p. 195) given by

$$T(Z,t) = C\cos\left(\frac{\delta Z}{L}\right)\exp\left[-\left(\frac{\delta}{L}\right)^2 \kappa t\right] \tag{3.2}$$

where C is a constant, δ is the first root of $\delta\tan\delta = Bi$, in which Bi is the Biot number,

defined as $Bi = \frac{hL}{k}$ where k is the thermal conductivity. The term κ stands for thermal diffusivity $\left(\frac{k}{\rho C_p}\right)$ where ρ is density and C_p is the specific heat. Then, the resulting residual stress profile is given as follows (the reader is referred to Aydıner et al. [11] for full derivation):

$$\sigma_X(Z) = \frac{\alpha E(T_g - T_a)}{1-\nu}\left(1 - \frac{\sin\delta}{\delta} - \int_0^{\frac{Z}{L}} \frac{(\sin\delta - \sin\delta\zeta)\sin\delta\zeta}{(1-\zeta)\cos^2\delta\zeta}\,d\zeta\right) \tag{3.3}$$

where α is the coefficient of linear thermal expansion, E is the Young's modulus, ν is the Poisson's ratio and T_a is the ambient temperature.

The instant freezing model provided a convenient closed form solution in the pre-computer days, yet it was not invalidated by the more advanced and realistic models as far as the final value of residual stresses are concerned. Indeed, when initial (pre-quench) temperature, T_i is sufficiently bigger than T_g[3], the instant freezing model predicts the residual stresses as well as the viscoelastic (Lee et al. [50]) or structural (Narayanaswmay [64]) theories within the accuracy of the material data and the stress measurement technique (Gardon [34]). This may be surprizing due to the extreme oversimplification of the material behavior, but can be understood considering two facts. First, although the freezing temperature (at which the timescale of stress relaxation becomes 'big' compared to the experimental timescale) will depend on the model, eventually at some temperature below T_g the residual stresses generated will be the thermoelastic temperature equilization stresses. Obviously, these stresses are equal for all models and they constitute a large of fraction of the final stresses. Secondly, if it is assumed that the thermal gradients are monotonically decaying or growing during solidification, i.e., the sense of stresses generated at a

[3]This requirement is partly due to not considering the higher order terms in the temperature solution. Depending on the cooling rate, T_i should be sufficiently bigger than T_g such that these terms decay to zero before the temperatures across the plate cool to T_g. (Seifert et al. [78].)

Initial(melt) temperature	T_i	900°C
Quenching temperature	T_a	25°C
Glass transiton temperature	T_g	352°C
Young's modulus	E	96 GPa
Poisson's ratio	ν	0.36
Glassy CTE	α_g	9.8×10^{-6} 1/K

Table 3.1: Processing parameters and thermophysical properties of Vit.1 reproduced from Appendix A.

material point remains the same when it passes through the glass transition *range*, the model has an averaging effect by ignoring both the non-relaxed ('remembered') portion of stresses that are generated above T_g and the relaxation of stresses that are generated below T_g. Certainly, however, the instant freezing assumption is too crude to correctly predict the time evolution of solidification stresses. Since BMG's are in molten state when they are cast, initial temperatures are much higher than T_g (see Table 3.1). Hence, the instant freezing model can be expected to estimate the tempering stresses in these materials rather accurately when equation (3.1) is applicable for their quenching process. Besides, the closed form expression provides insight and points out the important physical parameters. Among these, the dimensionless Biot number, $Bi = \frac{hL}{k}$, is particularly important. Just from the heat transfer perspective, Biot number determines the extent of thermal gradients that will be formed in the sample (Incropera and DeWitt [41]) depicted by the spatial (cosine) term in equation (3.2). Note that thermal conductivity is the only material parameter in Biot number. Density and specific heat merely alter the overall decay speed of the same temperature evolution through thermal diffusivity. Thus, via equation (3.3), the residual stress profile formed in Vit.1 plates can be calculated given the Biot number and a small set of process parameters and material properties presented in Table 3.1. Results are plotted in Figure 3.2 and Figure 3.3. The former shows the magnitude of mid-plane tension and

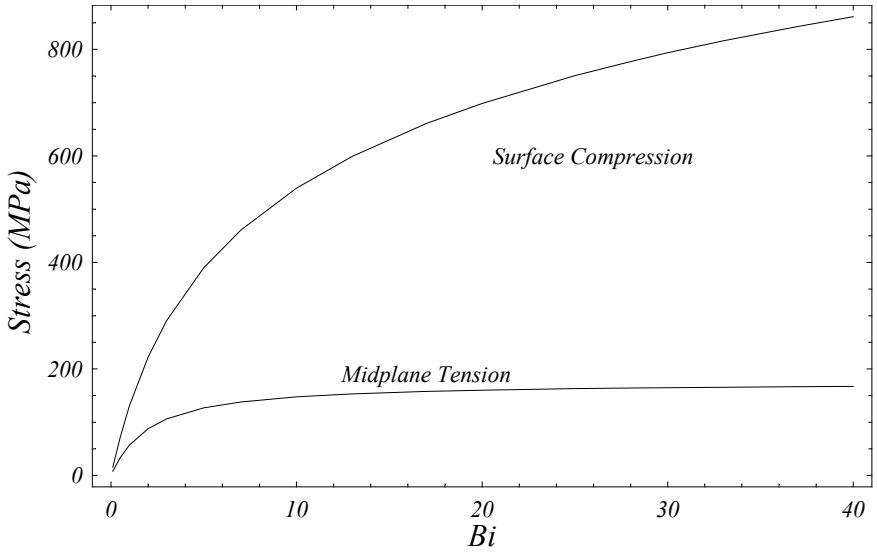

Figure 3.2: Effect of the Biot number on the absolute values of surface compression and mid-plane tension in a Vit.1 plate.

surface compression as a function of Bi and the latter presents residual stress profiles (σ_X vs. Z/L) for a set of Biot numbers.

It is shown in Figure 3.2 that, as Biot number increases, mid-plane tension goes to an asymptotic value whereas surface compression keeps monotonically rising. This saturated value of mid-plane tension can be evaluated from equation (3.3) as 175 MPa by taking the $Bi \to \infty$ limit of $\sigma_X(0)$. Also, since the balancing mid-plane tension saturates, as the value of surface compression increases, the thickness of the surface layer it is confined to decreases. As seen in Figure 3.3, this means that a progressively thinner surface layer with an increasingly high stress gradient can be formed as the degree of temper increases. On the other hand, the strong temperature dependence of its thermal parameters (described in Appendix A) seems to be a problem for the application of the instant freezing model to Vit.1. In particular, thermal conductivity, which is the first order parameter, exhibits pronounced temperature dependence increasing from $4.59\,\mathrm{W/(m \cdot K)}$ at 25°C to $20.05\,\mathrm{W/(m \cdot K)}$ at

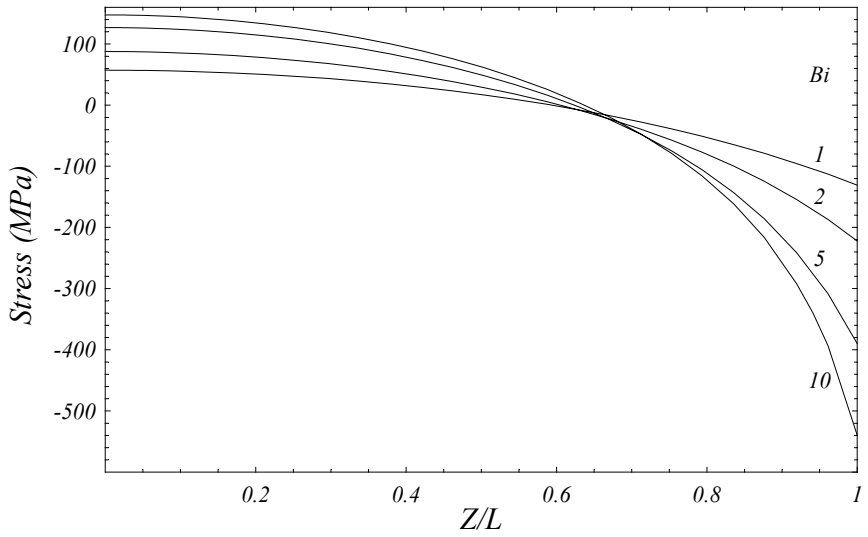

Figure 3.3: Residual stress profiles across the half-thickness of a Vit.1 plate as a function of the Biot number, $Bi = h\,L/k$. According to the model predictions, about 35% of plate thickness will be in compression.

900°C in an approximately linear fashion. Hence, equation (3.2) which is for constant thermal parameters becomes apparently invalid. To remedy this problem, the heat transfer problem is solved with the simplification that thermal conductivity is assumed constant at its T_g value ($k = k(T_g) = 9.98\,\mathrm{W/(m \cdot K)}$) to obtain an approximate temperature solution. Then, fortunately, it is seen that, in the critical interval about T_g, this approximate solution tends to the 'exact' solution that uses the detailed temperature dependent data in Appendix A. This is demonstrated in Figure 3.4[4]. Hence, the stress estimates via instant freezing model remain valid with a small error (most probably contained within the error of the model), if we define Biot number as $\tilde{B}i = \frac{h\,L}{k(T_g)}$.

[4]Note in the figure comparison is made at equal mid-plane temperatures instead of equal times. The instant freezing model does not have a 'real' time dependence since it comprises material behavior on two extremes of viscoelasticity only (elastic solid and non-viscous fluid). For example, one can artificially increase the decay speed of the temperature evolution by multiplying thermal diffusivity with an arbitrary number and the stress prediction will be unaltered.

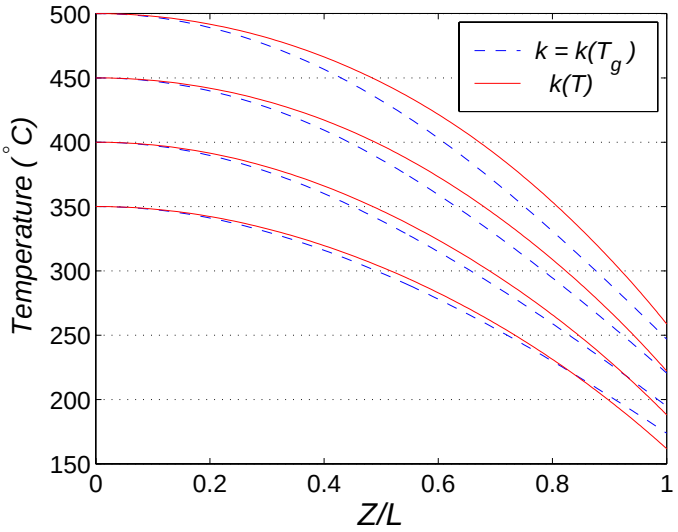

Figure 3.4: Temperature profiles at selected mid-plane temperatures (350, 400, 450, 500°C) for the temperature evolution during the quench of a Vit.1 plate. Calculations are carried out (i) with the actual temperature-dependent thermal parameters (Appendix A) including thermal conductivity, $k(T)$ (straight lines) (ii) with the simplification that $k = k(T_g) = 9.98\,\mathrm{W/(m \cdot K)}$ (dashed lines). (Process parameters for these runs are $T_i = 900°\mathrm{C}$, $T_a = 25°\mathrm{C}$, $h = 4800\,\mathrm{W/(m^2 \cdot K)}$, $L = 4.125$ mm, yielding $\tilde{B}i \simeq 2$.)

3.3.2 Viscoelastic Model

3.3.2.1 Introduction

Historically, this was the second model developed to quantify the thermal tempering of silicate glasses (Lee et al. [50]). The viscoelastic model employed the measured rheological properties of the *equilibrium* liquid at each temperature. Hence, it replaced the awkward jump from a non-viscous fluid to a linear elastic solid in the former instant freezing models with a smooth transition. The viscoelastic model was applied to a class of materials with thermorheological simplicity. For such a material, the creep function, relaxation modulus and any other characteristic viscoelastic function plotted versus the logarithm of time exhibit only a simple shift when the temperature is changed to another constant value. Equilibrium liquids of silicate glasses (called stabilized glass) were shown to be thermorheologically

simple prior to the analysis in [50].

For the tempering problem, the appropriate viscoelastic function is the shear relaxation modulus and at a certain temperature T, it will be denoted by $\mathbf{G}^T$. Bulk relaxation is typically more sluggish than shear relaxation and Lee et al. made the assumption of elastic bulk response. Hence in this problem, the viscoelastic behavior of the material over the entire temperature range is obtained using two material functions only. The first is the shear relaxation modulus measured at a reference temperature, T_r, denoted by $\mathbf{G}^r(t)$ and the second is the 'shift function', $a(T)$, which bears the temperature dependence. It shifts the reference function $\mathbf{G}^r(t)$ in logarithm of time to obtain $\mathbf{G}^T$, namely, the relaxation modulus at the temperature of interest.

3.3.2.2 Viscoelastic Model for Bulk Metallic Glass

The author is not aware of any definitive data on isothermal measurements of shear relaxation moduli for $Zr_{41.2}Ti_{13.8}Cu_{12.5}Ni_{10}Be_{22.5}$ (Vit.1$^{\text{TM}}$) at various temperatures. Therefore, this model considers the *equilibrium* viscosity of this alloy which has been thoroughly studied with creep tests around the glass transition and rotating cup experiments about the melting point (Waniuk et al [89], Masuhr et al. [57], Busch et al. [21]). The viscosity data covers a range of 14 orders of magnitude and is successfully fit with the Vogel-Fulcher-Tammann (VFT) relation as follows:

$$\eta(T) = \eta_0 \exp\left[\frac{D^* T_0}{T - T_0}\right] \tag{3.4}$$

where, D^* is called the fragility parameter and T_0 is the VFT kinetic freezing temperature. The value of η_0 is 4×10^{-5} Pa $\cdot$ s and the best fits to the experimental data yield $D^* = 18.5$

and $T_0 = 412.5$ K [89].

Since the steady-flow viscosities were measured with creep tests in the temperature range of interest, the following relation between viscosity and relaxation modulus at temperature T holds (see, e.g. Ferry [33], p. 70):

$$\eta(T) = \frac{1}{2}\int_0^\infty \mathbf{G}^T(t)\,dt \tag{3.5}$$

The determination of the relaxation modulus from the scalar viscosity data is not possible. Therefore, the analysis was pursued as a parametric study for the relaxation time spectrum (Aydıner et al. [12]). In other words, a set of relaxation moduli with varying spectra were considered for residual stress calculations such that they satisfied equation (3.5). To conveniently cover a broad relaxation spectra, the Kohlrausch-Williams-Watts (KWW) form was assumed for the relaxation modulus:

$$\mathbf{G}^T(t) = 2\mu(T)\,\exp\left[-\left(\frac{t}{\tau_s(T)}\right)^{\beta_s}\right] \tag{3.6}$$

where β_s is the stretching exponent and $\mu(T)$ the instantaneous shear modulus at T. $\beta_s = 1$ corresponds to Debye relaxation and the spectrum broadens as β_s decreases. $\tau_s(T)$ is calculated by substituting equation (3.6) in equation equation (3.4) as follows:

$$\tau_s(T) = \frac{\eta(T)}{\mu(T)}\,\frac{1}{\Gamma(1+1/\beta_s)} \tag{3.7}$$

Calculations were carried out for β_s values that systematically varied in increments of 0.05 in the $0.5 \leq \beta_s \leq 1$ range. First, the temperature dependence of the shear modulus was neglected and its room temperature value ($\mu^{RT} = 35.3$ GPa) was used. This was one of the

assumptions made by Narayanaswamy [64] in his analysis of silicate glass tempering after noting Kurkjian's data [48] that showed $\sim 15\%$ decrease in the shear modulus of glass as its temperature approached the glass transition region. Recently, a similar decrease (10–20%) in the elastic modulus of some metallic glasses has been measured as the temperature reached T_g (Keryvin et al. [44]). To investigate the sensitivity of the residual stresses to such changes in the shear modulus, a second set of computations was made by assuming a linear variation of the shear modulus from $\mu^{RT} = 35.3$ GPa at room temperature to $0.85 \cdot \mu^{RT}$ ($= 30.0$ GPa) at T_g. The results showed that the effect of shear modulus variation with temperature was negligible as far as the final residual stress values were concerned (the change was less than 0.25%). Therefore, this effect is excluded from the discussion that follows.

Note that any possible temperature dependence of the Kohlrausch factor β_s was not considered in the above parametric study. This was done to preserve the thermorheological simplicity assumption. Allowing for the temperature variation of β_s invalidates thermorheological simplicity and excessively complicates the calculations impeding the use of the current numerical method. Furthermore, the extremely weak dependence of the solution on β_s justifies this negligence of its variation with temperature.

The viscoelastic model calculations were performed using the finite element method and the details are described in the next section. The comparison of results obtained from both the instant freezing and viscoelastic models is exhibited in Figure 3.5. It is seen that the predicted residual stresses are rather insensitive to the value of the Kohlrausch factor, β_s, for the range of β_s values considered ($0.5 \leq \beta_s \leq 1$). The variation in mid-plane tension and surface compression with β_s in this range is under 5.4% (the calculated stresses increase when β_s changes from 0.5 to 1).

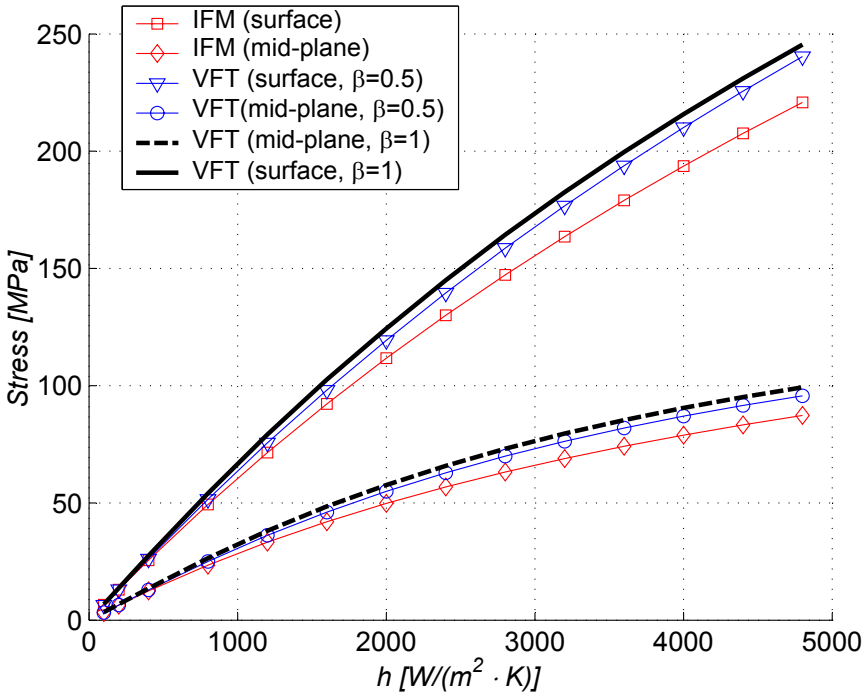

Figure 3.5: Absolute values of surface and mid-plane stresses predicted by both instant freezing (IFM) and viscoelastic-VFT models of thermal tempering of an 8.25 mm thick Vit.1 plate as a function of (convection) heat transfer coefficient. The VFT data are shown for two different calculations using $\beta_s = 0.5$ and 1 in equation (3.6).

Finally, all the arguments presented above assume the thermal stability of the BMG alloy throughout the quenching process, and phenomena such as phase separation [89, 57] were not considered. In addition, the non-linear viscous response (e.g., shear thinning) of the material (Lu [53]) due to high shear rates was also ignored.

3.3.2.3 Implementation of the Viscoelastic Model

The calculations for the viscoelastic model were conducted using the ABAQUS^{TM} finite element (FE) software[5]. A one-dimensional model was built (see Figure 3.6) to represent an infinite plate. The elements were arranged along the plate thickness direction (Z) with symmetry imposed on both perpendicular directions (X and Y). To implement the compatibility condition for the infinite plate, first, the right side nodes were constrained to deform as a line. Second, unlike regular plane strain elements where the displacements in the Y direction would merely be set to zero, generalized plane strain elements were used that allowed uniform deformation in the out-of-plane direction Y. The lengths of the elements along the Z direction were biased such that the mesh became finer towards the surface where there are higher temperature gradients. The cooling of the plate was carried out via convection heat transfer applied on the top surface. Thermorheological simplicity in ABAQUS was defined for the relaxation function, namely, relaxation modulus normalized by its instantaneous value was given by $\exp[-(t/\tau_s)^{\beta_s}]$ in the KWW formalism. This way, the use of temperature-dependent shear modulus $\mu(T)$, which invalidates thermorheological simplicity for relaxation modulus but not relaxation function, did not pose any additional

[5]For this one-dimensional thermoviscoelastic problem, the semi-analytical solution of Lee et al. that involves two coupled integral equations can be obtained with the efficient algorithm of Narayanaswamy and Gardon [65]. This algorithm was implemented in MATLAB^{TM}and FE analysis results here were verified. Unfortunately, this approach cannot be pursued even for a slightly more complicated geometry (e.g. the cylinder geometry of Chapter 4 or more detailed constitutive behavior (such as the considered temperature dependence of shear modulus) making the incorporation of FE analysis a necessary task.

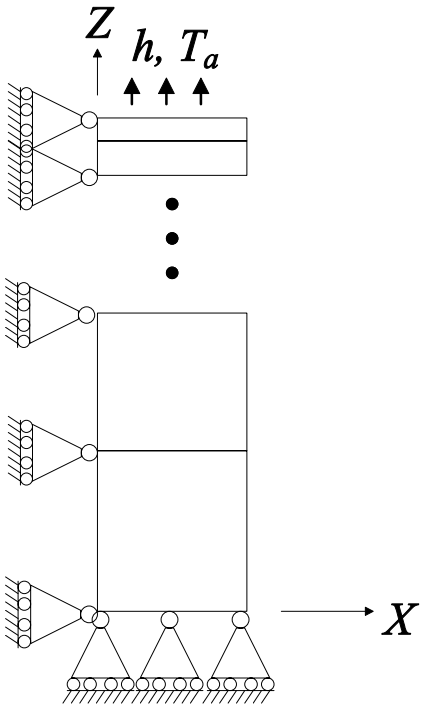

Figure 3.6: Schematic of the finite element model used in viscoelastic model calculations. An infinite plate is represented via symmetric elements (in X and Y) while the plate half-thickness extends along Z. The elements (or nodes) on the right hand side are required to move uniformly along the X direction.

difficulties. The relaxation function was calculated and input to the program at a reference temperature T_r and the shift function given below was implemented with a user-defined subroutine:

$$a(T) = \frac{\tau_s(T)}{\tau_s(T_r)} = \frac{\mu(T_r)}{\mu(T)} \exp\left[D^* T_0 \left(\frac{1}{T_r - T_0} - \frac{1}{T - T_0}\right)\right] \tag{3.8}$$

3.3.3 'Perfect' Contact Analysis of the Copper Mold Casting

The analysis up to this point has been pursued as a function of heat transfer coefficients and close results have been obtained for instant freezing and viscoelastic models. To make

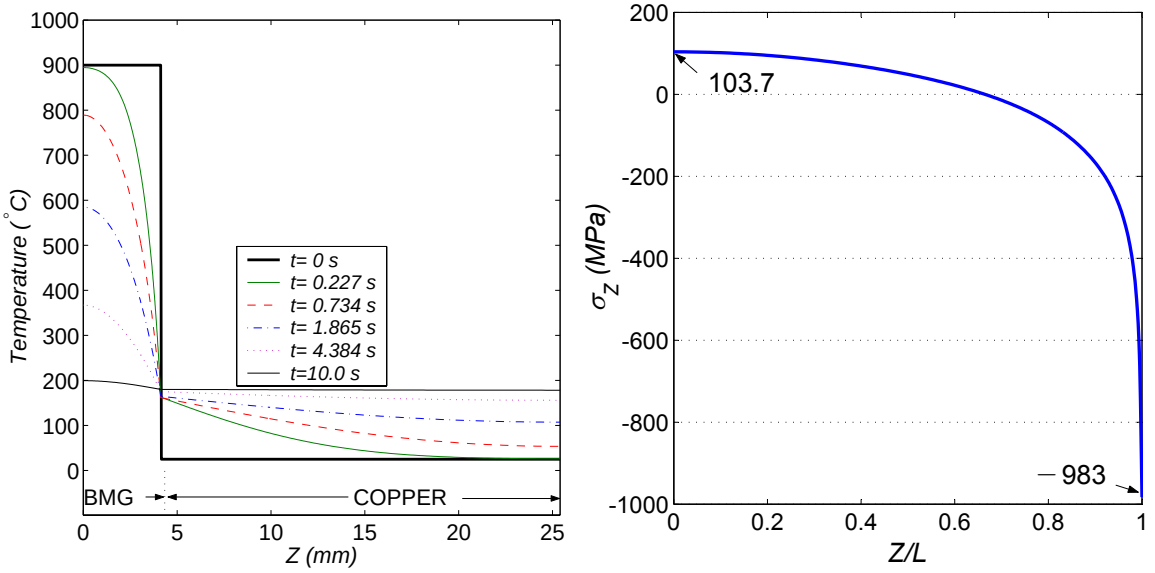

Figure 3.7: (a) Temperature profiles at selected times in the cross section of the cast Vit.1 (initially at 900°C) and the copper mold (initially at 25°C) that are put in instantaneous contact and do not separate ('perfect' contact) throughout the process. (b) The residual stresses induced in Vit.1 by this temperature solution.

quantitative comparison with the experimental data, now let us draw our attention to the casting process of the considered plate. Obviously, this process does not involve convective cooling on traction-free surfaces.

In the heat transfer analysis, considering that the filling stage takes a very small time compared to the overall duration of the process, flow effects are ignored and the heat transfer problem is approximated by putting the 8.25 mm thick Vit.1 melt at 900°C in instantaneous contact with copper mold at 25°C. A one-dimensional solution is conducted in MATLAB$^{\text{TM}}$ for this boundary value problem observing the symmetry about $Z = 0$. Free air convection ($= 20\,\text{W}/(\text{m}\cdot\text{K})$ [41]) is also applied on the outer surface of the mold, which, not surprisingly, had negligible effect. The calculation made use of the material data in Appendix A and Table 3.2 for Vit.1 and copper, respectively, and assumed perfect contact (no separation) between the two. The temperature evolution is shown in Figure 3.7(a) that

plots the temperature profile at several representative times. The heat transfer upon contact is extremely fast and reduces the BMG surface temperature to $\sim 170°C$ instantaneously. The BMG surface temperature, or more precisely, the temperature at the BMG-copper boundary remains at the same level in the rest of the process, increasing only $\sim 20°C$ as the copper mold heats up. Eventually, both phases come to equilibrium at about $\sim 190°C$. Naturally, once the temperature accross the plate thickness gets sufficiently below $T_g = 352°C$, residual stresses are not influenced by the treatment in the rest of the process. This temperature history is similar in nature to what would be imposed by convective cooling with an extremely high h by a medium at temperature $T_a = 170°C$ since, in the $h \to \infty$ limit of convective cooling, surface temperature is brought to T_a instantaneously [16].

Before, pursuing a sequential mechanical analysis with the developed models, it is required to justify the negligence of the filling stage for the stresses. At this point, we refer to residual stress studies in the injection molding process used in the polymer industry (e.g., Struik [82], Hastenberg et al. [38], Zoetelief et al. [93]). For polymers, the residual stresses are classified as flow-induced stresses and residual thermal stresses. Flow-induced stresses are the stresses generated during the filling stage of the mold whereas the residual thermal stresses are due to the differential cooling of the material, which is the only case for the thermal tempering problem. It is noted in [93] that the flow stresses are an order of magnitude lower than the thermal stresses in absolute value. This is not surprising since the existence of flow at considerable rates indicates that most of the material still has very short shear stress relaxation times, and thus, is not able to accumulate residual stresses. Based on this argument, it is likely that the residual stresses that form in the BMG plate are also mostly thermal residual stresses. For the considered plate, this assumption will be corroborated by the nature of measured residual stresses.

Density (kg/m^3)	8933
Thermal conductivity ($W/(m \cdot K)$)	413 @ $-73°C$ 393 @ 123°C 379 @ 323°C
Specific Heat ($J/(kg \cdot K)$)	356@ $-73°C$ 397@123°C 417@323°C

Table 3.2: Thermophysical properties of pure copper [41].

Hence, it is reasonable to apply the models developed for estimating residual stresses and Figure 3.7(b) shows the resulting stress profile from the viscoelastic analysis with $\beta_s = 1$. As expected, the surface stress is extremely high (-983 MPa) and the stress gradient at the surface is very steep. The mid-plane tension is 104 MPa which is in reasonable agreement with the limiting value from instant freezing model for $T_a = 170°C$ as 97 MPa.

The perfect contact analysis in this section has been made to have a reference point in the interpretation of measured residual stresses. In actual fact, due to the nature of the process, BMG likely separates from the mold cavity. As it will be explained in section 3.6, the comparison of perfect contact analysis results with the measured stresses indeed leads to this conclusion.

3.4 Residual Stress Measurement Using the Crack Compliance Method

Residual stresses in BMGs cannot be conveniently determined by non-destructive methods. While photoelasticity could be used in silicate glasses to measure both residual and in situ stress profiles during processing (Gardon [34]), the opacity of BMGs prevents the use of this method. Diffraction is similarly not applicable since BMGs are amorphous. Therefore, mechanical relaxation methods remain as the only options to obtain the stress profile within

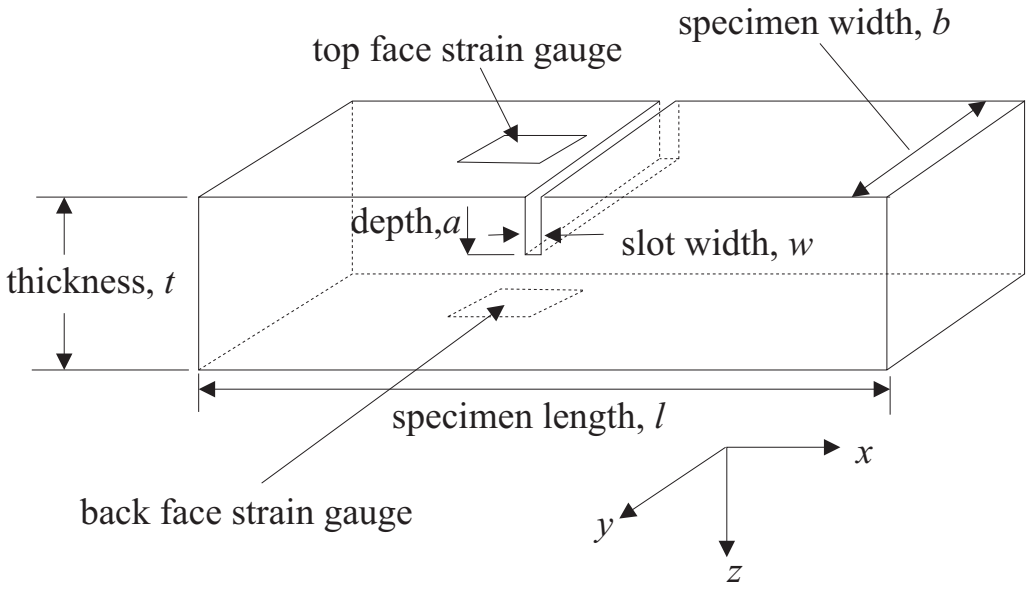

Figure 3.8: Crack compliance method terminology (adapted from [68]).

the desired spatial resolution. These methods rely on disturbing the equilibrium of a sample under residual stress by removing material in a particular way. The deformation of the sample as it reaches a new equilibrium is then monitored and this information is used to back-calculate the original residual stresses. The crack compliance method (Prime [68], Cheng and Finnie [22]) was chosen in this study since it allows accurate determination of the complete through-thickness profile with good spatial resolution in the measurement direction.

In this method, strains are measured as a slit is incrementally cut through a specimen. Assuming that the stress relaxation from cutting the slit is elastic, the original profile of residual stress is calculated from the measured strains. Figure 3.8 illustrates a crack compliance measurement and defines the terminology. A slit is introduced, and its depth a in the Z direction is extended incrementally. The test is used to determine $\sigma_X(Z)$ through the thickness of the specimen. Two strain gauges are employed. The top strain gauge, placed very near the cut, is used for determining the stresses in the near surface region

($a/t < 0.05$). The back gauge is placed directly opposite to the cut and is used to calculate the stresses through the remaining portion of the specimen.

The original residual stresses are determined from the measured strains using the series expansion approach (Prime [68], Schajer [75]) , which is very tolerant of noise and errors in the experimental strain data. It is first assumed that the unknown stress variation as a function of the through-thickness coordinate can be expressed as a series expansion:

$$\sigma_X(Z) = \sum_{i=1}^{n} A_i \, P_i(Z) \; = \; [P]\{A\} \tag{3.9}$$

where, the A_i represent unknown series coefficients. For this study, Legendre polynomials expanded over the thickness of the plates were chosen for the P_i because, by excluding the 0th and 1st order polynomials, the resulting stress distribution is guaranteed to satisfy force and moment equilibrium. The strains that would be measured at the cut depths a_j are calculated for each term in the series. These are called the compliance functions C_{ij}. Using superposition, the strains given by the series expansion can be written as

$$\epsilon_X(a_j) = \sum_{i=1}^{n} A_i \, C(a_j, P_i) \; = \; [C]\{A\} \tag{3.10}$$

A least squares fit to minimize the error between the strains given by equation (3.10) and the measured strains yields the A_i (and hence the stresses by equation (3.9)) and can be written as

$$\{A\} = \left([C]^T[C]\right)^{-1} \, [C]^T \, \{\epsilon_{measured}\} \tag{3.11}$$

In this study, the compliance functions for the top strain gauge were calculated using a numerical, body-force method solution for a slot in a semi-infinite solid (Cheng and Finnie [23])

with some improvements made to the numerical solution (Prime and Finnie [69]). The compliance functions for the back strain gauge were calculated by two-dimensional finite element calculations of a crack in a plate. Uncertainties in the final stress prediction were based on standard error propagation formulas applied to the above equations using the difference between the measured and calculated strains (equation (3.10)) as the measurement uncertainty (Hill and Lin [40]). Using too low an order, n in equation (3.9), of an expansion results in not fitting the measured strains well and, therefore, leads to large uncertainties in the stresses. Inversely, using too high of an order results in a more singular matrix inverse, equation (3.11), and also large uncertainties in the stresses. Thus, an optimal fit order was chosen to minimize uncertainty.

The cuts were made using wire electric discharge machining (EDM), which is preferred over mechanical cutting. The machine was set to 'skim cut' settings to minimize stresses induced during cutting (Cheng et al. [24]). It must be mentioned that the dimensional accuracy of the samples was not perfect since they were extracted from a cast plate. The thickness of the sample in the cut plane varied within 0.1 mm for most samples. The cut depth and thickness values were based on accurate measurements performed with an optical microscope from both sides of the sample. Figure 3.9, which is roughly to scale, shows the original locations of samples extracted from the plate. The seven samples tested for through-thickness stress profiles in the Y direction were named Y1,..., Y7, and similarly the four samples tested in the X direction were called X1,..., X4. One face of the plate was selected as the top and was kept as such for all samples except Y7, X2 and X4 that were intentionally slit from the other side to check the symmetry of the stress profile. Sample A1 was annealed at 290°C for two hours to relieve the residual stresses. This temperature is high enough to allow rapid stress relaxation (Suh and Dauskardt [83]) without significantly

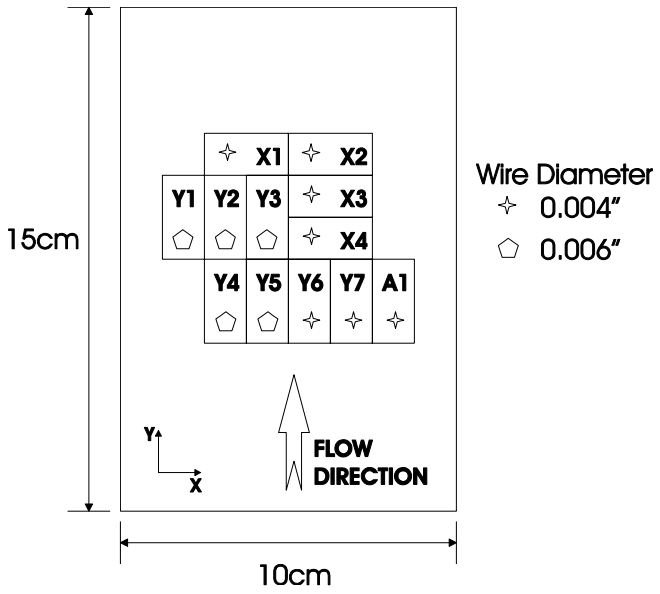

Figure 3.9: Locations of samples in the plate before cutting. Plate dimensions are 150 mm by 100 mm by 8.25 mm. Wire diameters used in cutting each sample are indicated in inches. The flow direction of the molten BMG during casting is also shown. The samples are 12.7 mm by 25.4 mm. The ones designated by X were used to determine in-plane stresses along the X direction (σ_X), while those named Y1, etc., were used to measure σ_Y.

changing the structure of Vit.1. The amorphous structure of A1 after heat treatment was confirmed with X-ray diffraction. The samples were nominally 25.4 mm long by 12.7 mm wide. The sample length, l, was large enough ($l/t \sim 3$) to substantially preserve the original residual stresses in the measurement direction on the cut plane (Prime and Hill [71]). Also the width dimension, b, was large enough to conform to the plane strain assumption used in the calculations [71]. While the earlier tests employed a 0.006 inch (0.150 mm) diameter wire, the later ones used a 0.004 inch (0.100 mm) diameter wire (see Figure 3.9 about a distribution of samples for each). The slot was cut in 0.254 mm increments. This value was reduced to 0.127 mm during the first few steps to obtain a higher resolution near the top surface.

3.5 Experimental Results

The top gauge did not yield reliable data in some early tests. This was attributed to the poor attachment and coating of the gauge which prevented its waterproof installation. The EDM machine used in these tests employed a water jet to keep the wire-workpiece region engulfed in a dielectric fluid. Fortunately, most of the data comes from the back gauge (from 10 to 90% of the thickness of the sample) and a top gauge is not strictly necessary. Therefore, almost the complete stress profile can be obtained using only back gauge data. The disadvantages in this case are that the precision in the near-surface stresses is low and the stabilizing effect of the top gauge on the solution is lost. Nevertheless, the uncertainty analysis correctly accounts for such issues. In this study, it was seen that the accuracy of the mid-plane stresses was still quite good and the trend of the stress profile was adequately resolved. On the other hand, the tests for samples X1, X2, X4, Y7 and A1 were successful in yielding data from both gauges and the results obtained from the first four of these samples are similar to those obtained from all other as-cast specimens. The back gauge strain profiles from all specimens are shown in Figure 3.10. It is worth noting that the profiles for all samples, tested both in X and Y directions (except the stress-relieved A1), exhibited remarkable similarity in shape and magnitude even though a few of the tests, e.g., that of Y6 and X4, yielded somewhat lower quality data. This shows, first, that the stress profile has weak X–Y coordinate (spatial) dependence and it also suggests that the stress state is approximately equibiaxial. Note that if samples with stress profiles that are merely multiples of each other are considered, back gauge strain vs. normalized depth data will scale linearly with the amplitude of these stress profiles. On the other hand, top gauge data is not directly comparable for its values will also depend on the gauge-to-slot distance.

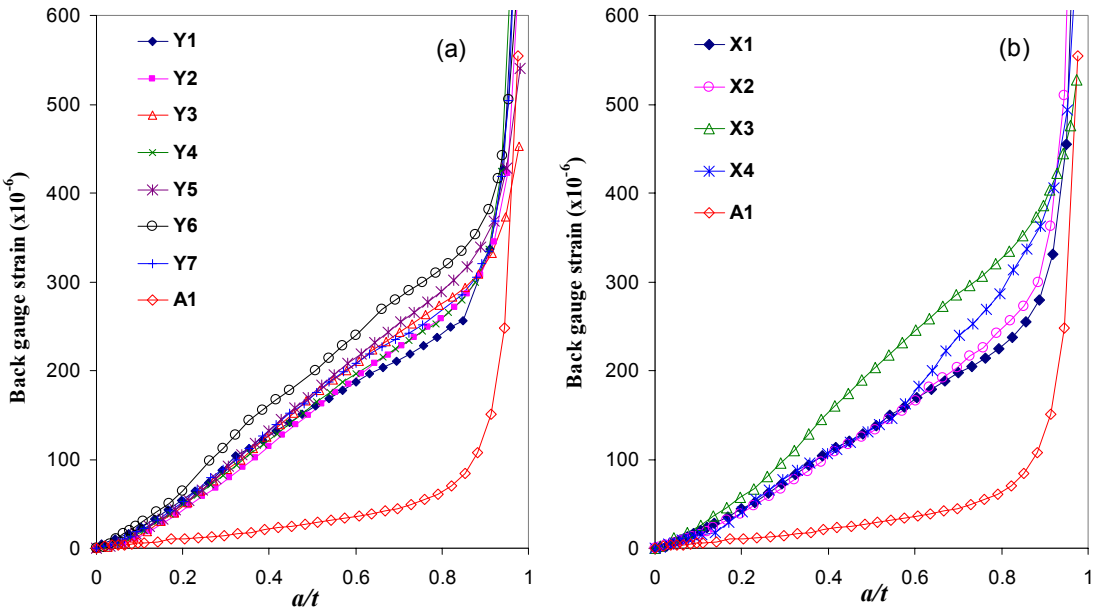

Figure 3.10: Back strain vs. normalized depth data for samples (a) in the Y direction, and (b) in the X direction, in comparison to the annealed sample A1. See Figure 3.9 for original specimen locations on the plate.

Typical stress profiles obtained from the back gauge data of specimens Y2, Y3, Y4 are shown Figure 3.11(a). These tests yielded particularly clean data and reduction of the stress profile was straightforward. In Figure 3.11(b), the test of Y7 is compared with that of the annealed sample, A1. Since the top gauge worked in both tests, the stresses on the top surface are also exhibited. The error bars in Figure 3.11 are seen to be much smaller than the observed stress profile. More significantly, the apparent stress variation in the annealed specimen (A1) is within 5 MPa indicating the stress resolution of the crack compliance method.

Note that only stress values that are significant are plotted. This involves excluding a number of points near the top surface where the back gauge response is too weak (for the tests where the top gauge did not function properly) and a few points close the full thickness of the sample where the strains no longer give a good estimate of the residual stress. As the

remaining ligament ($t - a$ in Figure 3.8) becomes small, several factors (e.g., the weight of the specimen and tension in the lead wires) increasingly contribute to the strain measured by the back strain gauge by causing bending and torsion of the remaining ligament. In small samples such as these, additional stiffness from the gauge coating can also affect the strain readings as the remaining ligament becomes small. The net effect of the remaining ligament becoming small is that the experimentally measured strains become singular as the cut approaches the back face, see Figure 3.10, whereas without these effects the strain would approach a finite value (surface stress divided by plane strain elastic modulus) as the cut neared the opposite surface. In these specimens, the singular effects became significant after about $a/t = 0.92$; therefore, stresses are not reported beyond that depth.

As seen in Figure 3.10, especially samples Y6 and X4 do not follow the generaly observed smooth profile. Their data show awkward changes in slope and some especially bad data points were deleted. Later it was realized that the reason was variations in the flow of the dielectric fluid and formation of bubbles on the gauge surfaces as the EDM wire moved into the sample. This happened only for a few samples because the wax coating on the gauges of these samples had apparently a rougher surface that caused complicated flow patterns. Some samples such as the ones in Figure 3.11(a) were usually very stable. Caution should be exercised when inverting the stresses from problematic strain data as fitting the noise will result in a wavy profile instead of the simple 'compression on the surface, tension in the middle' distribution.

The next source of error that was valid for all samples is called the 'EDM effect'. During EDM cutting, a thin material layer (with a new stress state) can be recast on the cut surfaces. This especially affects the top gauge data while the back gauge is relatively insensitive. The data from the test on the annealed specimen—very small strains measured

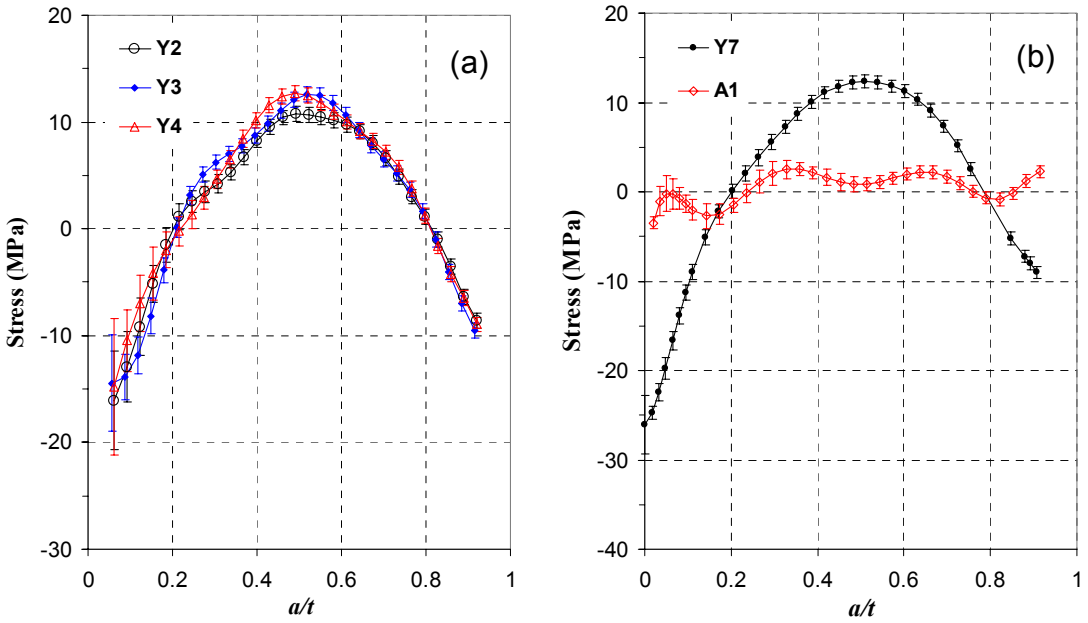

Figure 3.11: (a) Calculated stress profile vs. normalized depth reduced from the back gauge strain data only. (b) The stress profile obtained from both top and back gauges.

by the back gauge and inconsistently large values from the top gauge—confirmed the likelihood of an EDM effect. The consistency of bottom gauge results for tests made with both 0.004 inch and 0.006 inch diameter wires also corroborates that the back gauge data were unaffected. An EDM correction detailed in [24] was performed to the top gauge strains in order to obtain the stress profiles shown in Figure 3.11(b). The profile of strain as a function of cut depth that is caused by an EDM effect is quite different from the profile caused by residual stresses. It can be estimated analytically and separated out from the measured strains.

Several factors combined to make the EDM effect an issue in these tests, whereas it is usually insignificant [24]. The major factor is that the residual stresses are so low in the tested specimens. The strains caused by the EDM effect are generally a fixed small value, independent of the residual stress magnitudes, when cutting is performed gently.

Thus, they generally comprise an insignificant portion of the measured strains and do not have a noticeable effect on the results. When the stresses are extremely low, as in the tests reported here, the EDM strains can contribute significantly to the measured data and, therefore, affect the results. The other factor is that the EDM effect is, other parameters equal, greater for materials with higher yield stress and low thermal conductivity, both of which apply to the BMG specimens. Even so, if the residual stresses were higher, the EDM effect would have been negligible.

3.6 Discussion

Figure 3.5 exhibits the predictions of both the instant freezing and viscoelastic models. Despite vastly different approaches and the use of independent data in each, their similarity is remarkable. For instance, the shapes of the stress vs. heat transfer coefficient plots are almost identical.

The model predictions that are obtained by the analysis that assumed 'perfect' contact between copper mold and BMG (section 3.3.3) ($\sim$ 100 MPa for mid-plane tension and $\sim$ 1000 MPa for surface compression), however, are significantly different than the experimental results (10–13 MPa mid-plane tension and 25–30 MPa surface compression) that are much smaller. To understand the discrepancy, consider the two main stages of the analysis, the heat transfer problem (processing) and mechanical constitutive model (instant freezing and viscoelastic models).

Both instant freezing and viscoelastic models disregard a critical component of glass behavior: its structural relaxation from a metastable amorphous solid to a supercooled liquid in thermodynamic equilibrium [89, 57]. During this process, the excess free volume trapped in the material is relaxed by short range atomic movement leading to a denser,

more viscous solid. In viscoelastic theory, data for the viscoelastic behavior of the equilibrium material at every temperature is employed. Therefore, just from viscosity point of view, the viscoelastic model employed in this study is expected to overestimate the temper stresses with respect to a more advanced structural model which can accurately consider the transient effects during structural relaxation. However, as explained earlier, residual stresses are dominantly thermoelastic temperature equilization stresses and such deficient description of relaxation behavior about glass transition region has a limited affect on them. Hence, deficient material behavior is not likely to be responsible for the order of magnitude error.

The assumption that the thermal stresses are dominant over the flow-induced stresses is justified by the experimental data since (i) measured stress profiles have no significant spatial and directional dependence and, (ii) the observed 'compression-tension-compression' stress profile is typical of thermal tempering [34, 11].

Therefore, it can be concluded that major part of the discrepancy is due to the temperature solution. The low magnitude of measured stresses suggests a relatively flat temperature profile about the glass transition of Vit.1 existed during the casting. The only major assumption in the analysis which otherwise made use of carefully measured material data and actual dimensions is that the contact between the Vit.1 and copper mold is maintained during the entire process. Therefore, it is inferred that separation occured before the temperature of the majority of the sample crossection cooled to T_g. After separation, the heat transfer from the plate through the vacuumed mold cavity would be significantly reduced. Separation is expected due to the immediate solid skin formation suggested by the thermal analysis and subsequent shrinkage of the core. The perfect contact analysis was conducted to prove the point.

The difficulty of determining heat transfer in the mold casting with the separation phenomenon, may be the reason that the concept of heat transfer coefficient with equation (3.1) has been used in the literature for mold casting processes (see, e.g., Zoetelief [93], an example from polymer literature). This *effective* heat transfer coefficient suggested by the stress measurements can be obtained from Figure 3.5 assuming reasonable accuracy from the considered models.

These results point to the need for an instrumented casting experiment during which the exact temperature profile of BMG can be monitored that would allow a healthy comparison of mechanical model and experiment results. This is done in Chapter 4.

Finally, it is worth mentioning the fact that lack of high temper stresses in BMGs is not necessarily a disadvantage. Conventional (crystalline) metals typically have residual stresses on the order of 25–50% of their yield strength (Prime and Hill [71], Yazdi et al. [92]). Such stresses contribute to failure by fracture, fatigue, stress corrosion cracking, and other stress-driven processes (Wulpi [91]). These stresses are also a major source of expensive distortion problems caused during machining to final shape (Lequeu et al. [51]). Stress relief in conventional metals, by thermal treatment or by cold working (Tanner et al. [84], Metals Handbook [1]) is generally expensive and often not possible because it can significantly degrade mechanical properties. By contrast, the peak residual stresses measured in BMGs in this study only amount to about 1.5% of the yield strength. From a distortion and mechanical failure point of view, such low stresses can effectively be neglected.

3.7 Conclusion

This investigation of thermal-tempering-induced residual stresses in a thick BMG plate had two premises: (i) to accurately measure the residual stresses in BMG samples, and (ii) to

compare the results with appropriate theory and obtain insight about the processing method and the material properties. The first was accomplished by the use of the crack compliance method, which is capable of yielding through-thickness stress profiles. The method is applicable with wire EDM cutting taking advantage of the fair electrical conductivity of BMGs. Although the measured stress magnitudes were low, the technique yielded good resolution.

The measured stress profiles exhibited thermal tempering characteristics. The comparison between the theory and experiments yielded two main results (i) The BMG plate has separated from the mold before T_g and the heat transfer dropped taking the stresses down. (ii) A detailed comparison of the model cannot be made in this process and an instrumented casting process is necessary.

It is shown that same processing method of BMG plates introduces very small stresses in the material although certain dependence on process parameters (esp. feed pressure) is expected. When the pressure is higher more material can be packed inside avoiding separation for a longer time, that would be expected to result in higher thermal gradients and stresses.

The non-existence of stresses may be an advantage since an annealing treatment might bring together physical aging (free volume reduction) which results in a decrease in fracture toughness. On the other hand, the compromised heat transfer after separation might result in crystallization which will limit the critical thickness that can be attained with this procedure.

Chapter 4

Residual Stresses in a Bulk Metallic Glass Cylinder Induced by Thermal Tempering

4.1 Introduction

The purpose of the investigation in this chapter is to control the processing conditions so that a more accurate estimate of tempering stresses can be performed (Aydıner and Üstündag [9]). More specifically, the error in the heat transfer problem is minimized (recall the structure of the thermal tempering problem on Figure 1.3) so that the 'actual' agreement between the developed viscoelastic model (section 3.3.2) and experimentally determined residual stresses can be evaluated. This is accomplished by casting BMG in a stainless steel (SS) tube, which due to its higher coefficient of thermal expansion will always clamp onto the BMG core and help assure contact throughout the quenching process. In addition, the heat transfer coefficient during the quenching is actually measured.

A strong interface forms between BMG and SS after casting that is indicative of their mutual contact. To investigate the temper stresses, SS is cut out of this BMG-SS composite. Finite element analysis is performed to investigate the possible effect of its mechanical interaction with SS during casting on the final residual stresses in BMG. These stresses are

then determined using the crack compliance method. The reader is also referred to a closely akin and complimentary study presented in Appendix B. There, the stress state in a BMG-SS composite that is cast with the same method is investigated with finite element analysis and non-destructive elastic strain measurement on the SS phase via neutron diffraction.

4.2 Experimental Procedure

4.2.1 Sample Preparation

The casting process is optimized to assure uniform cooling and continuous thermal contact between the BMG and the mold. A type AISI 304L stainless steel tube (12.7 mm outer and 10.7 mm inner diameters) is used as mold. One of its ends is closed and a plug machined from the same material is slid upside down to its bottom such that an empty space forms (Figure 4.1). The tube-plug assembly is evacuated to 10^{-1} Pa and flushed with Ar gas several times. While still under vacuum, it is heated to about 900°C where the $Zr_{41.2}Ti_{13.8}Cu_{12.5}Ni_{10}Be_{22.5}$ (Vit.1) alloy completely melts and fills the tube. The tube is then quickly immersed in iced water (at 0°C) which is continuously stirred with a magnetic bar to ascertain temperature uniformity. The evacuated space above and below the BMG is considered to be of sufficiently low thermal conductivity so that most of the heat transfer will occur in the lateral direction via the circumference. In addition, to approximate the stress analysis with a plane problem, the length of the casting is large with respect to its diameter (the aspect ratio is above 8). To avoid the end effects in the heat transfer and stress analyses, the actual sample is cut 30 mm above the bottom of the cast assembly (Figure 4.1).

One advantage of such a sample preparation procedure (in addition to making the heat

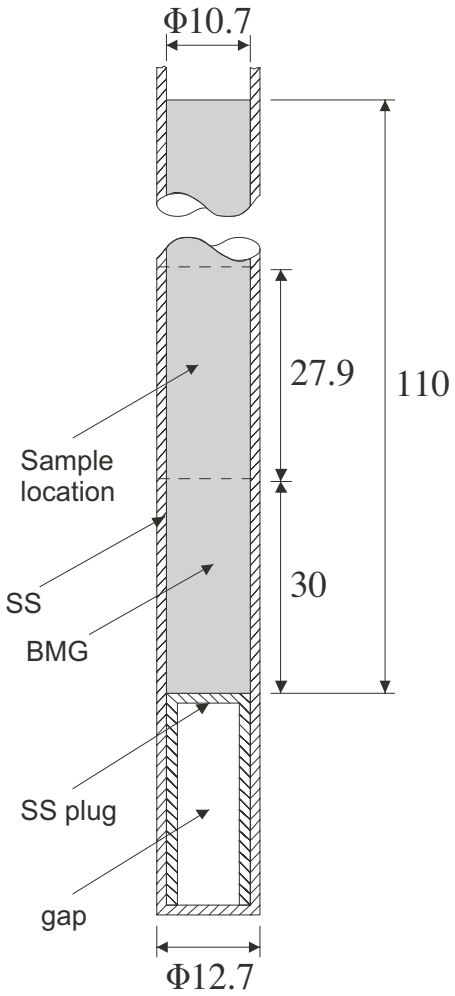

Figure 4.1: Geometry of the BMG alloy cast in a stainless steel (SS) tube. The actual sample location used in crack compliance measurements is shown between dashed lines. All dimensions are in mm.

transfer problem one-dimensional) is that it promotes contact between the mold and the BMG. As mentioned above, the CTE of the stainless steel is always higher than that of the BMG at all temperatures of interest. Since the initial temperature is the same for both, the tube is expected to be clamping on the BMG core during the cooling process. The strong interface that forms between the two is an indication of the continuity of their mutual contact. Another advantage of the processing used here is that the boundary conditions of the problem are well defined, e.g., the initial and final temperatures for both the BMG and stainless steel are well known.

Following the casting and quenching, the stainless steel tube is removed with wire electric discharge machining (EDM). The EDM process imposes insignificant cutting forces on the sample, and hence, almost no inelastic deformation is expected during cutting. However, it produces a thin molten and re-solidified layer (called the EDM layer) which typically is under tension (Cheng et al. [24]). To avoid the contribution of this layer to the final residual stress state in the BMG, it is removed by a two-minute application of an acid solution (10% HF + 45% HNO3 + 45% deionized water). This also eliminates the thin reaction layer that forms between the BMG and the steel during casting. The exclusion of the stainless steel tube after quenching serves two purposes. First, it relaxes the residual stresses due to the interaction of the tube and the BMG core. For instance, the CTE mismatch between the tube and the BMG can generate significant residual stresses in both. The second advantage brought by the removal of the tube is the fact that it greatly simplifies the crack compliance analysis of the residual stresses in the BMG. These issues are further discussed in the following sections.

4.2.2 Heat Transfer Coefficient Analysis

An accurate estimate of the heat transfer coefficient during processing is crucial for a successful comparison of experimental data with model predictions in thermal tempering. Unfortunately, several experimental difficulties make it very difficult to directly monitor the temperature evolution in the BMG during its casting and quenching. First, since the initial temperature of the BMG alloy is over 900°C, a thermocouple embedded in it will lead to an extensive interface reaction which will complicate the interpretation of the results by introducing additional thermal effects. Second, a thermocouple cast within the BMG will generate extra residual stresses that will confuse the stress analysis. Third, feeding the thermocouple through the *present* vacuum system is unfeasible. Use of a thermocouple on the lateral tube surface, on the other hand, is difficult since the tube wall is thin and properly insulating the thermocouple against water is problematic. Furthermore, a surface temperature measurement will require a faster response from the thermocouple and may lower the temporal resolution since the cooling rate at the surface is more extreme in comparison to the center.

It is therefore decided to employ a solid stainless steel rod (type AISI 304) of 100 mm length and 12.7 mm diameter with a thermocouple probe inserted in its center. This approach requires detailed knowledge of the thermophysical properties of the stainless steel as a function of temperature (see Table 4.1). Once the temperature evolution in the probe is measured, the only critical unknown in the process is the value of the convection heat transfer coefficient on the surface of the stainless steel. A fast-response thermocouple probe (0.5 mm diameter, type HKMTSS-020G with AISI 304 sheath from Omega Engineering, Stamford CT) is inserted into a 0.55 mm blind hole machined with punch EDM into a 50 mm depth from top surface. The hole is filled with Omega CC high temperature thermocouple

cement to ensure good thermal contact between the probe and the rod. Care is also taken to avoid direct contact between the quenching medium and the probe. The actual casting process is then simulated by taking the rod to 900°C and quenching into the same iced water used before for BMG processing.

The convection heat transfer coefficient (h) is defined as (Incropera and DeWitt [41]):

$$Q = h(T_s - T_\infty) \tag{4.1}$$

where Q is heat flux, T_s is surface temperature of the tube and T_∞ is temperature of the cooling medium (= 0°C). In the present analysis, using the ABAQUS^{TM} finite element software, the heat transfer problem is solved for a set of presumed heat transfer coefficients and the center temperature is extracted to compare with experimental data. Since a long rod is employed in the experiment, cooling at its center (at mid-length) is assumed to occur from the circumference only. Therefore, the heat transfer problem is reduced to a one-dimensional, axis-symmetric case where the temperature is a function of the radial coordinate only. The calculations use a mesh of 60 CAX8RT quadratic heat transfer elements biased from the center to the surface. The simulation results for heat transfer coefficients ranging from $6,000$ to $20,000\,\mathrm{W/(m^2 \cdot K)}$ in increments of $2,000\,\mathrm{W/(m^2 \cdot K)}$ are shown in Figure 4.2(a) together with the experimental data.

Two problems appear when the simulations and data are compared. First, the determination of the exact starting time for the quenching during the experiment is difficult since several seconds pass when the rod is taken out of the furnace and dipped in the water. The second problem is that the experimental curve does not seem to follow the calculated curve of a single heat transfer coefficient throughout the entire process. The probable explanation

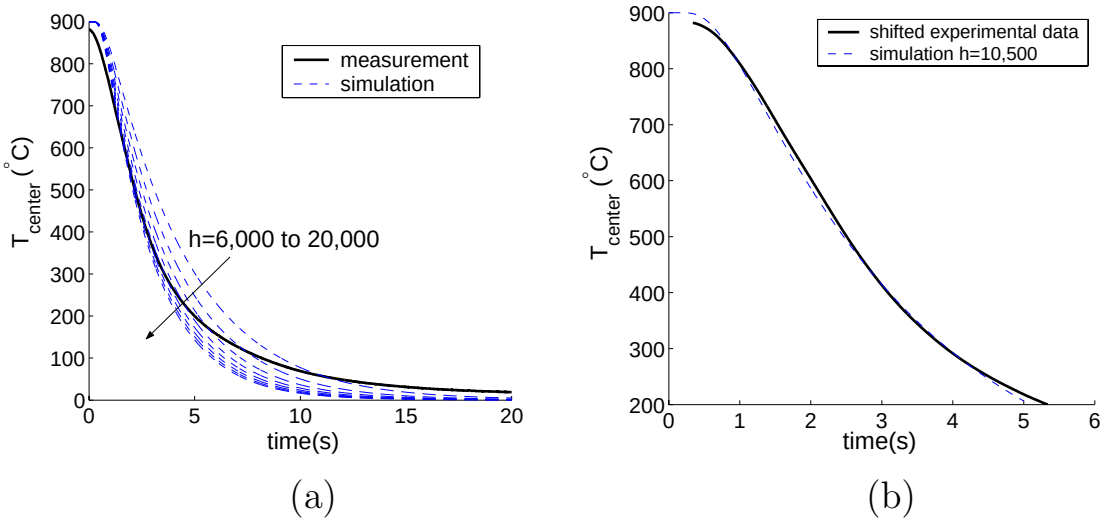

(a) (b)

Figure 4.2: Center temperature of the stainless steel rod used in heat transfer analysis as a function of quenching time. (a) Experimental data in comparison to simulations for $h = 6,000$ to $20,000\,\mathrm{W/(m^2 \cdot K)}$ in increments of $2000\,\mathrm{W/(m^2 \cdot K)}$. (b) The fit of the $h = 10,500\,\mathrm{W/(m^2 \cdot K)}$ simulation to the experimental data, which yields the best fit after the time offset optimization as detailed in the text.

for the latter is the extensive boiling observed in the early parts of the quenching which is known to enhance convective heat transfer [41].

Fortunately, the second problem can be remedied by the physics of the thermal tempering phenomenon. In thermal tempering, once the entire sample cross section freezes (i.e., becomes elastic), the stresses produced in the rest of the process are entirely determined by the temperature profile at that instant, i.e., the nature of the heat transfer after this point has no influence on the subsequent residual stress generation. Therefore, the convective heat transfer should be investigated only until the center temperature drops sufficiently below the glass transition temperature of the BMG. A 5-second initial period of quenching is chosen for this purpose since, as will be shown later, the center temperature of the BMG core is reduced below 300°C in that interval. To obtain the best fit between the experimental data and the simulated curves (and thus determine the value of the heat transfer coefficient in that period), the time offset between the two has to be optimized. Suppose

the measured temperature data are expressed by a function $f_{exp}(t_{exp})$ and the simulation curve for heat transfer coefficient h_i is denoted by$f^i_{sim}(t_{sim})$. Then the time offset between the two is $t_{offset} = t_{exp} - t_{sim}$. If the offset is corrected, the fitting error between the two curves in the 0 to 5 seconds time interval will be given by

$$err_i = \int_0^5 \left[f_{exp}(t) - f^i_{sim}(t - t_{offset})\right]^2 dt \tag{4.2}$$

The heat transfer coefficient that best represents the experimental data is h_j such that $err_j = \min(err_i)$, for all i. However, since the t_{offset} is unknown, it is first estimated as the value which minimizes err_i by translating the simulation function in time such that it matches the experimental function. In practice, f_{exp} and f^i_{sim} are taken as high order polynomials that represent the data well and the minimization of equation(4.2) for each simulation is implemented in Mathematica$^{\text{TM}}$ to calculate t_{offset}. Figure 4.2(b) displays the best match obtained for a heat transfer coefficient of $h = 10,500\,\text{W}/(\text{m}^2 \cdot \text{K})$. The resolution of the above procedure barely differentiates between $10,000$ and $10,500\,\text{W}/(\text{m}^2 \cdot \text{K})$ which suggests an error of about 5% in the value of h.

Finally, to evaluate the temperature history in the actual composite sample with this heat transfer coefficient another ABAQUS$^{\text{TM}}$ heat transfer analysis is performed. The temperature at the center of the BMG core after 5 seconds is found to be 280°C. This temperature is well below the glass transition temperature of the BMG alloy ($\sim$ 350°C) and assures that the BMG has solidified enough to be considered an elastic solid (in fact, the viscoelastic model discussed later yields a stress relaxation time of 4.3×10^8 seconds at 280°C). Therefore, it can be concluded that within the critical first 5-second period during quenching, the convection heat transfer coefficient on the outside surface of the stainless

Young's modulus (GPa)	193 [4]
Poisson's ratio	0.3 [4]
Room temperature yield strength (MPa)	170 [4]
Density (kg/m^3)	8.0 [4]
Thermal conductivity (W/(m $\cdot$ K))	12.6 @ 200 K 16.6 @ 400 K 19.8 @ 600 K 22.6 @ 800 K 25.4 @ 1000 K 28.0 @ 1200 K [41]
Specific Heat (J/(kg $\cdot$ K))	402 @ 200 K 515 @ 400 K 557@600 K 582 @ 800 K 611 @ 1000 K 640 @ 1200 K [41]
Coefficient of thermal expansion ($\times 10^{-6}$ K^{-1})	18 [4]

Table 4.1: Thermophysical properties of stainless steel (AISI 304L) employed in the present study.

steel tube is about $10,500\,\mathrm{W/(m^2 \cdot K)}$.

4.2.3 Residual Stress Measurement via the Crack Compliance Method

In this technique, the mechanical relaxation when a slit is incrementally cut into a sample is monitored with strain gauges (Prime [68]). The strain vs. depth data obtained this way are then used to calculate the original residual stress field that is relaxed. This technique was described in Chapter 3 on samples cut from a BMG plate and provided excellent accuracy despite the low stress values. In the present study, the technique is adapted to cylindrical geometry (Figure 4.3). The specimen dimensions are chosen to satisfy the plane strain condition for all slit depths: length, $L = 27.9$ mm and diameter, $D = 10.67$ mm (aspect ratio > 2.5). The slitting is accomplished with wire EDM in steps of, first, 0.127 mm, and then 0.254 mm. Both top and back strain gauges yielded reliable information. Additional details about the cutting procedure can be found in Section 3.4.

The hoop stress in the BMG cylinder (σ_θ) is calculated by assuming that the original residual stress profile along the cut depth can be represented by a series expansion:

$$\sigma_\theta(x) = \sum_{i=1}^{n} A_i \, P_i(x) \; = \; [P]\{A\} \tag{4.3}$$

where, P_i are chosen as Legendre polynomials expanded over the diameter of the specimen and A_i are the coefficients that provide the best approximation of $\sigma(x)$ via equation (4.3). Then, the strains that *would* be measured at a cut depth a_j are calculated for the residual stress distribution at that instant using the compliance functions $C(a_j, P_i)$ via linear superposition:

$$\epsilon_\theta(a_j) = \sum_{i=1}^{n} A_i \, C(a_j, P_i) \; = \; [C]\{A\} \tag{4.4}$$

A least-squares fit that minimizes the error between the measured strains and those given by equation (4.4) determines the coefficients A_i (and hence the stresses via equation (4.3)) and can be expressed as

$$\{A\} = \left([C]^T[C]\right)^{-1} [C]^T \{\epsilon_{measured}\} \tag{4.5}$$

The fit order n is chosen to minimize the total fitting error which has two constituents (Prime and Hill [70], Hill and Lin [40]): (i) the first error measures how well the chosen series can represent the actual stress profile, i.e., the *completeness* of the series. (ii) The second error propagates the fitting error in strains to the error in stresses and depends not only on the magnitude of the former but also on the *condition* of the inversion in equation (4.5).

The compliances in this study are calculated by a finite element model developed with

ABAQUS^{TM} that also employed Python scripts (Lutz [55]). The model geometry is shown in Figure 4.3(b). At each experimental value of slit depth, a_i the model geometry is modified and re-meshed using reduced integration, rectangular plane strain elements. Then the stress functions $P_i(x)$ in the series (equation (4.3)) are applied on the slit surfaces (Bueckner's superposition principle (Prime [68])) to obtain the compliances. Mesh convergence is achieved throughout the analysis. To accurately represent the strain gauges, their locations are partitioned on the circumference of the model. This permits the overlaying of an exact number of elements on the gauge surfaces. Then the nodes on these surfaces are compiled into node sets as shown in Figure 4.3(b). The magnified view of the back gauge node set (Figure 4.3(c)) exhibits quadratic elements that allow accurate representation of the curved surface. On the gauge surface, the face length of each element can be calculated as the path integral of the quadratic interpolant. Then the face lengths of all these elements are summed to obtain the gauge length. Applying this procedure on the coordinates of the nodes yields the initial gauge length, l_0 (Figure 4.3(c)), and similarly, the deformed gauge length, l, is obtained by using the deformed coordinates (Figure 4.3(d)). Therefore, the engineering hoop strain measured by the strain gauge can be calculated as $\epsilon_\theta = (l - l_0)/l_0$.

4.3 Results and Analysis

4.3.1 Residual Stresses due to Thermal Tempering

The results of the crack compliance measurement are shown in Figure 4.4 for three cases: (i) top gauge only (which has a low depth sensitivity but is more accurate for surface regions); (ii) back gauge only (which is sensitive over most of the cross section) and (iii) both gauges (the results of both gauges are combined in the stress calculation step). The

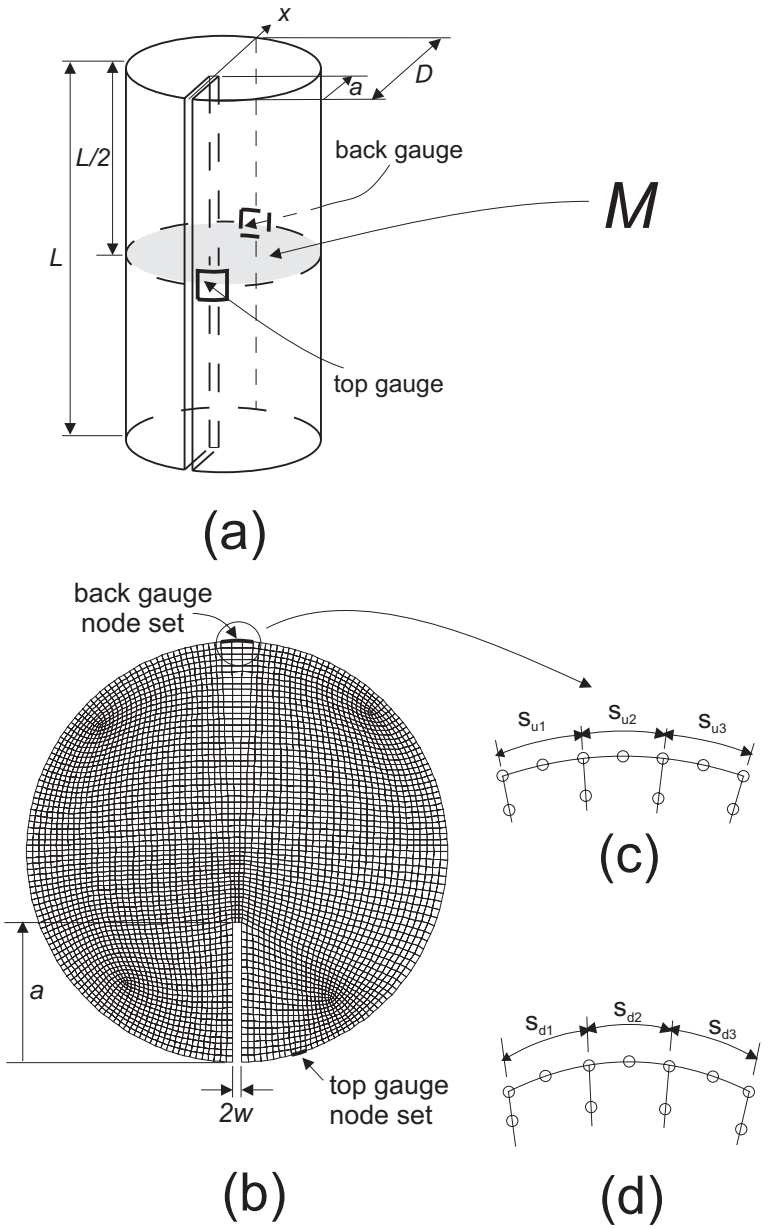

Figure 4.3: Geometry of the stress measurement and analysis. (a) The nomenclature of the crack compliance method applied to a long cylinder. Strain gauges are placed on the circumference of plane M at the mid-length of the rod where the plane strain condition is satisfied. (b) The two-dimensional finite element mesh on plane M for a certain slot depth, a. The nodes that are on the top and back strain gauge locations are defined as node sets. The initial (c) and deformed (d) configurations of the back gauge node set are magnified. The initial gauge length is given by $l_0 = s_{u1} + s_{u2} + s_{u3}$ and the deformed gauge length is $l = s_{d1} + s_{d2} + s_{d3}$.

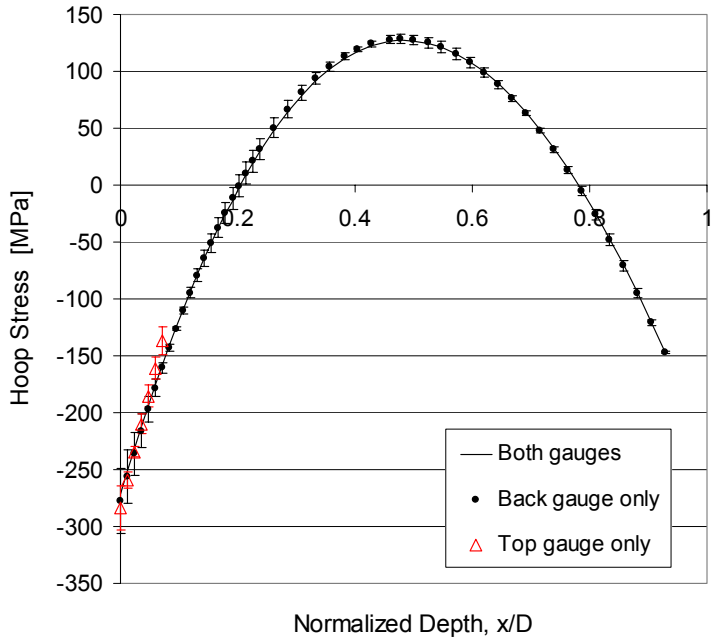

Figure 4.4: Measured hoop stress in the BMG cylinder as a function of normalized cut depth (x/D). Data obtained from (i) top gauge only, (ii) bottom gauge only, and (iii) both gauges combined are shown. All three analyses yield nearly identical results. The error bars represent the fitting errors in the crack compliance analysis.

agreement between the independent top and back gauge results is remarkable. This suggests an accurate measurement also helped by the high residual stress values which yield a good signal-to-noise ratio. As a result, the EDM effect (Cheng et al. [24]) that was an issue in back-calculating the residual stresses for the plate considered in Chapter 3 becomes insignificant in the present one. In addition, the low order of the optimal fit (merely a third order polynomial fits best both cases (ii) and (iii)) keeps the inversion in equation (4.5) well conditioned. When the top gauge is added to the analysis to improve it (Hill and Lin [40]), the total fitting error is reduced below 3 MPa for all depths. Of course, there are other error sources in the crack compliance method, e.g., the error in determining the gauge locations, the slight skew of the cut, etc. which are not accounted by the present analysis. However, these errors are normally not as significant as the fitting error [40]. A careful review of the

stress profile shown in Figure 4.4 leads to three main conclusions. First, a compression-tension-compression profile typical for thermal tempering is observed. Second, the stress magnitudes are quite high, an order of magnitude higher than those in the plate studied in Chapter 3 although the sample dimensions are comparable. And third, the residual stresses are symmetric about the sample center. The last observation strongly corroborates the axial symmetry of the residual stress profile as expected from thermal tempering and helps with the justification of the assumptions used in the heat transfer analysis. The next section compares the predictions of the viscoelastic model of thermal tempering with these experimental data.

4.3.2 Viscoelastic Model of Thermal Tempering

The viscoelastic model for the thermal tempering of BMG (Aydıner et al. [12]) is based on its equilibrium viscosity which is given by the Vogel-Fulcher-Tammann (VFT) relation (Waniuk et al. [89]):

$$\eta(T) = \eta_0 \exp\left[\frac{D^* T_0}{T - T_0}\right] \tag{4.6}$$

where, D^* is called the fragility parameter(=18.5 for the $Zr_{41.2}Ti_{13.8}Cu_{12.5}Ni_{10}Be_{22.5}$ BMG alloy), $\eta_0 = 4 \times 10^{-5}\,\mathrm{Pa \cdot s}$, and T_0 is the VFT kinetic freezing temperature(= 412.5 K). The classical viscoelastic theory of thermal tempering (Lee et al. [50]) requires the shear relaxation modulus as input and assumes the bulk relaxation is elastic due to its sluggishness. The shear relaxation modulus ($\mathbf{G}^T$) and viscosity at a temperature obey the following viscoelastic relation:

$$\eta(T) = \frac{1}{2}\int_0^\infty \mathbf{G}^T(t)\,dt \tag{4.7}$$

The parametric study in Section 3.3.2.2 showed that the predicted final residual stress state is practically independent of the shape of the relaxation modulus. Therefore, the simple Debye relaxation

$$\mathbf{G}^T(t) = 2\mu(T)\exp\left(-\frac{t}{\tau_s(T)}\right) \quad \text{where} \quad \tau_s(T) = \frac{\eta(T)}{\mu(T)} \tag{4.8}$$

yields residual stress values that are similar to those obtained from any other plausible form of G^T. Here, t is time, $\mu(T)$ is the instantaneous shear modulus at temperature T and $\tau_s(T)$ is the shear relaxation time. The reader is referred to Section 3.3.2 for further details of the viscoelastic model and how it is implemented in a finite element calculation.

Before proceeding with the comparison of model predictions with experimental data, the effect of the stainless steel tube on the final residual stress state in the BMG core needs to be analyzed. While the residual stresses in the quenched BMG-steel assembly are strongly influenced by the interaction between the two[1], the exact prediction of these stresses is difficult due to the lack of information on, e.g., the temperature-dependent constitutive behavior of the steel. However, the main emphasis of the present study is the residual stress state in the BMG *after* the removal of the steel tube, and it is shown below that the steel has a negligible influence on the final BMG stress state. To prove this point, a number of extreme cases are considered:

1. The stainless steel is elastic throughout the entire quenching process.

2. The steel is elastic-perfectly plastic with a constant yield strength taken as the room temperature value: 170 MPa (Table 4.1).

[1]The *measured* (with neutron diffraction on SS) and modeled stresses in a similar composite are studied in Appendix B.

3. The steel behaves as a mechanically inert insulation, i.e., it affects the heat transfer but its mechanical contribution is neglected.

The calculations are performed via the finite element method using the ABAQUS^{TM} package. A sequentially coupled thermal-stress analysis is conducted which involves the heat transfer calculations first. These yield the temperature evolution which is used in the subsequent mechanical analysis. Here, an implicit assumption is present, namely that the heat transfer and mechanical problems are uncoupled. This assumption is justified by the severe cooling during quenching which overwhelms heat generation in the sample due to inelastic deformation. The finite element mesh consists of a line of axis-symmetric elements along the radius of the composite. The interface between the two phases is assumed intact at all times. The elements of both phases are biased toward the interface. The kinematic boundary condition, in addition to axis-symmetry, is zero axial deformation at the bottom surface of the mesh. To impose the long cylinder condition, the nodes at the top are constrained to move together in the axial direction (generalized plane strain). The analysis also includes the removal of the stainless steel elements after cooling to room temperature for the first two cases above (case 1: steel is elastic, and case 2: steel is elastic-perfectly plastic). This way, a direct comparison with the residual stresses measured in the BMG core can be performed.

Figure 4.5 displays the results of the model calculations as a function of the heat transfer coefficient for all three cases of the stainless steel's constitutive behavior. It is clear that the final values of the residual stresses in the BMG (i.e., after the removal of the steel tube) are hardly influenced by the mechanical constraint of the steel. The largest discrepancy between the three extreme cases is about 3% of the stress values. While the calculations predict high residual stresses in the tube-BMG assembly after cooldown, most of the stresses

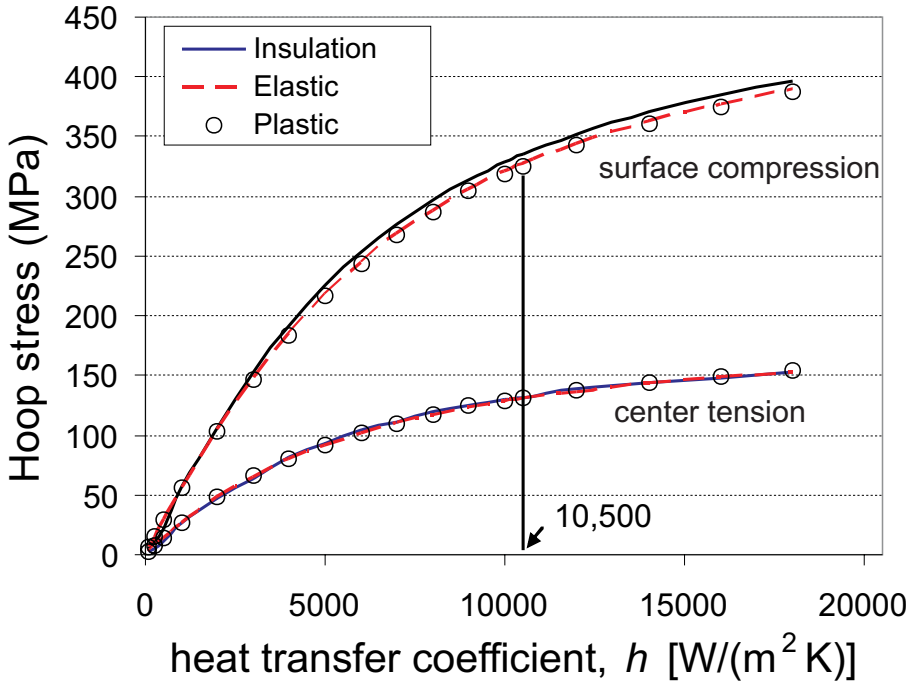

Figure 4.5: Absolute values of calculated surface compression and mid-plane tension in BMG (after the removal of the steel tube) plotted against the heat transfer coefficient, h, for all three cases of stainless steel during quenching: elastic, elastic-perfectly plastic and mechanically inert insulation. The experimental heat transfer coefficient value ($= 10,500\,\mathrm{W}/(\mathrm{m}^2 \cdot \mathrm{K})$) is noted.

are relaxed after the removal of the tube leaving only those due to the thermal tempering in the BMG. This result can be explained by the fact that the majority of the tempering-induced stresses result from temperature equalization (Gardon [34]). As mentioned earlier, these stresses develop after the whole specimen cross section becomes elastic and the decay of the temperature profile at that instant is the driving force. Once the BMG is elastic, the steel tube can only induce elastic stresses in it. Thus, when the steel is removed, regardless of how much stress it generated in the BMG, the temperature equalization stresses are unaltered. Based on these calculations, one can conclude that the effect of the steel on the final residual stresses in the BMG is negligible.

When the experimental data are compared to the simulation results using the measured heat transfer coefficient ($h = 10,500\,\mathrm{W/(m^2 \cdot K)}$), a close agreement is observed. The mid-plane hoop stress from the model calculation is +131 MPa in comparison to the experimental value of +125 MPa (about 5% difference). On the surface, the calculated stress is −330 MPa. However, since stresses at the very surface cannot be reliably measured with the crack compliance method, a comparison is made for stresses at the first experimental cut depth of $a/D = 0.012$. Here, the model predicts −315 MPa whereas the experiment measured −250 MPa (about 25% discrepancy). Of course, some of the discrepancy between the model and experiment is due to the uncertainties in the thermophysical properties of BMGs as a function of temperature. In particular, the thermal conductivity is a very sensitive parameter that influences tempering stresses.

The fact that the agreement is better on the mid-plane in comparison to surface is typical for the thermal tempering problem. The surface stresses are quite sensitive to error sources in the heat transfer problem, namely,

1. the error in approximating the heat transfer with a constant heat transfer coefficient;

2. the error in the value of the regressed heat transfer coefficient h;

3. the error in the temperature dependent thermal parameters of the material, in particular, thermal conductivity. As explained in Appendix A, these properties cannot directly be measured in the supercooled liquid region due to devitrification and extrapolated on the basis of physical formulations.

The sensitivity increases for the surface stresses due to the formation of steeper thermal and stress gradients in comparison to the mid-plane. Recall that it is only possible to compare the mechanical model results with the experimental results within the accuracy of the heat transfer solution that is input to the sequential mechanical analysis. From this perspective, the viscoelastic model agrees well with the experiment. The reader should also note that Narayanaswamy, in his definitive work on thermal tempering of silicate glasses (Narayanaswamy [64]) reported discrepancies between model predictions and experimental data of about 17% for mid-plane stresses and 35% for surface compression. The results of the present study, therefore, are noteworthy and show that the viscoelastic model is reasonably accurate in predicting thermal-tempering-induced residual stresses in BMGs.

4.4 Conclusions

An integrated theoretical-experimental investigation is performed on the thermal tempering of BMGs. Tempering-induced residual stresses are determined in a cylindrical specimen using the crack compliance technique. In addition, the convection heat transfer coefficient in the process is measured. The finite element method is employed to model the heat transfer and thermal tempering processes. The casting is done in a stainless steel tube to assure thermal contact during quenching and to better define the boundary conditions of

the problem. The following conclusions are reached:

1. High tempering stresses (around -300 MPa surface hoop stress) can be generated in BMGs with efficient cooling.

2. One way of generating such high stresses is by quenching in water which results in a high convection heat transfer coefficient ($h \sim 10,000\,\mathrm{W/(m^2 \cdot K)}$). This value is much higher that the typical heat transfer coefficients reached during the thermal tempering of silicate glasses via air jet cooling ($h \sim 500\,\mathrm{W/(m^2 \cdot K)}$, Gardon [34]). An important factor contributing to this discrepancy between the two types of glasses is the much higher thermal conductivity of BMGs ($k_{BMG} = 4.6$ to $20\,\mathrm{W/(m \cdot K)}$ vs. $k_{silica} = 1.4\,\mathrm{W/(m \cdot K)}$). Therefore, more severe cooling is required to induce large temperature gradients in BMGs.

3. The decay of these gradients below the glass transition temperature is the primary source of residual stress generation during thermal tempering.

4. The previously developed viscoelastic theory of thermal tempering in BMGs yields a good estimate of residual stresses if experimental conditions, especially the heat transfer coefficient, are accurately determined. In the present study, the viscoelastic theory predicts the mid-plane tension within 5% and the surface compression within 25% of the experimental values. The agreement is good from an engineering perspective and within the error of the heat transfer solution.

Chapter 5

Physical Aging of Vitreloy 1 and the Structural Model of Thermal Tempering

5.1 Introduction

In Chapter 4, agreement is achieved between the thermoviscoelastic model and the experimental results within the accuracy of the heat transfer solution. This agreement (5% at the center and 25% at the surface residual stresses) is on the same order as that accomplished in silicate glass tempering (Narayanaswamy [64]). Hence, from an engineering perspective, the implementation of higher order theories is not necessary for calculating tempering stresses in Vit.1 nor would this add more resolution to the problem given the unavoidable level of error in the heat transfer analysis.

The relative insensitivity of the final residual stresses on the sophistication of the mechanical model has been demonstrated with the success of the simplistic instant freezing model in Section 3.3. In sum, the details of BMG's constitutive behavior around glass transition do not have a significant impact on the final residual stresses, which are dominated by temperature equalization stresses. This was also the case in silicate glass tempering (Gardon [34]), where higher-order theories were not motivated by the poor prediction of residual

stresses, but rather by the need to quantify the transient stresses around glass transition. Transient stresses, which are tensile on the surface in the case of silicate glasses, could lead to the fracture of the workpiece. Until the incorporation of the temperature history dependence of the glass structure, the agreement with experiments was not achieved for the transient stresses measured with photoelasticity. Unfortunately, in situ measurement of transient stresses during BMG casting is not yet possible, leaving theoretical predictions uncomparable to experimental results.

However from the rheology science perspective, the quantification of the residual free volume trapped below glass transition as a function of the imposed cooling history $T(\mathbf{x}, t)$ poses a very interesting problem. This phenomenon is called 'physical aging' and has been extensively studied in polymers and silicate glasses (see, e.g., Kovacs et al. [47]). The essence of some relevant formulations as reviewed by McKenna and Simon [59] has been given in Section 2.4 and emphasizes Narayanaswamy's implementation for silicate glass tempering. These formulations made use of a structural relaxation modulus that quantifies the time-dependent volumetric response (expansion) of the material at metastable equilibrium when a small temperature jump is imposed on it. The models require a shift function which is dependent on the structure of the material.

In this chapter, we attempt to investigate the physical aging and the structural model of thermal tempering for Vit.1. First, the Matsuoka model (Section 2.7) for the shift function is adopted for metallic glass structures. Then, structural volume (as opposed to enthalpy) recovery experiments are conducted and described in Section 5.3. Volumetric recovery experiments are very challenging in terms of the resolution required for meaningful results. The instrument used here is a thermomechanical analyzer (TMA) in dilatometer mode, which has a length resolution of 0.1 micrometers. The strategy is to produce dilatometric

samples that have identical temperature histories, and therefore identical structures, so that each can be used for isothermal volume recovery experiments at a different temperature below T_g. Measuring the recovery of the same residual free volume at multiple annealing temperatures provides extensive data for comparison with the Matsuoka model. Since these samples must be fairly large ($\sim$ 13 mm long) to meet the resolution requirement, care must be exercised to impose a uniform temperature history within the samples as well. A specially designed mold is used for these purposes. Furthermore, a thermocouple is introduced into the casting and the uniform temperature history imposed on these samples is calculated from the *in situ* temperature data incorporating finite element analysis.

Finally, in the last Section 5.4, the structural theory with the Matsuoka model is applied to the tempering analysis of a Vit.1 plate. For implementation, user subroutines are coded for finite element calculations with the ABAQUS^{TM} software package.

5.2 Matsuoka Model

This model was introduced in Section 2.7. Matsuoka [58] successfully fits the polymer structural recovery data of Kovacs [46] with this model and criticizes the Arrhenius based function used by Narayanaswamy. The major reason the Matsuoka model is favored in the present study is that it is composed of a convenient extension of the VFT equation (4.6), and at least ideally, the constant D^*T_0 in the exponential function is unchanged. Therefore, adaptation of the model can be approached with the values regressed for the equilibrium liquid ($D^* = 18.5$ and $T_0 = 412.5$ K). Then, given temperature history $T(\mathbf{x}, t)$, the structural variable T_f can be calculated from the coupled solution of the expressions

$$T_f = T - \int_0^t \mathbf{M}_V^r(\xi(t) - \xi(t')\frac{\partial T}{\partial t'}dt' \tag{5.1}$$

and

$$\xi(T,T_f)=\int_0^t \frac{1}{a(T(t'),T_f(t'))}dt' \text{ where } a(T,T_f)=\exp\left[D^*T_0\left(\frac{1}{T}\frac{T_f}{T_f-T_0}-\frac{1}{T_{ref}-T_0}\right)\right] \tag{5.2}$$

Recall that T_f is related to thermal strain by

$$\varepsilon_\theta=\alpha_g\left(T(\mathbf{x},t)-T_i\right)+\alpha_s\left(T_f(\mathbf{x},t)-T_i\right) \tag{5.3}$$

and the corresponding *length* formulation (that is relevant for TMA experiments) is $l = l(0)+l(0)\,\varepsilon_\theta$. Markovsky and Soules [56] formulated an efficient, and unconditionally stable, explicit algorithm to replace the iterative solution of equations (5.1) and (5.2). This algorithm is implemented in MATLAB$^{\text{TM}}$ and verified with the iterative solution.

The form assumed for the structural relaxation function is once more the KWW function

$$\mathbf{M}_V^r=\exp(-t/\tau_{str}^r)^{\beta_{str}} \tag{5.4}$$

where the subscript τ_{str}^r is the structural relaxation time for the equilibrium liquid at reference temperature T_r (set as 800 K here) and β_{str} is the stretching exponent. For the preliminary analysis, β_{str} is taken equal to 1 (Debye relaxation). The variable of primary importance is the reference relaxation time τ_{str}^r, which can be expressed as

$$\tau_{str}^r=\frac{\eta(T_r)}{G_{str}} \tag{5.5}$$

where $\eta(T_r)$ is the equilibrium viscosity at the reference temperature and G_{str} is the structural stiffness. Since $\eta(T_r)$ is obtained from the VFT fit, to determine τ_{str}^r, all that is

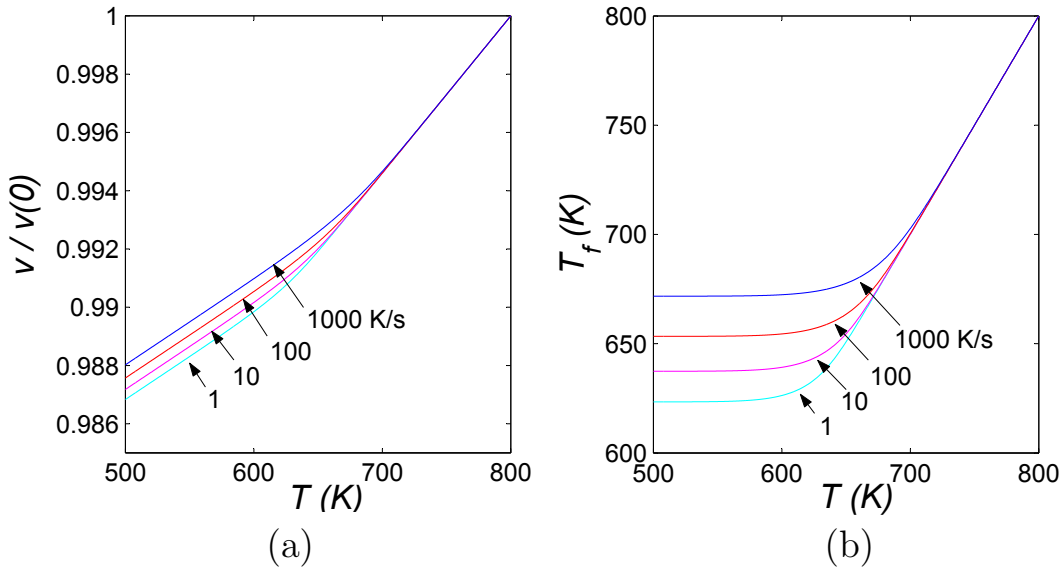

Figure 5.1: (a)Prediction of the formulation based on the Matsuoka model when the material is cooled from 800 to 500 K at the rates of 1, 10, 100, and 1000 K/s in terms of (a) specific volume normalized by its equilibrium value at 800 K, and (b) fictive temperature that is plotted vs. temperature.

needed is the value of G_{str}, which is typically lower in value than the shear modulus G (e.g., Rekhson and Mazurin [73] and Masuhr et al. [57]). Here, G_{str} is determined in reference to the data of Busch et al. [19] where the onset and end temperatures of calorimetric glass transition were measured at several different rates upon heating BMG samples in a DSC. For example, at 6.67 K/s, the onset and end temperatures of glass transition were measured as 636 and 680 K, respectively. Now, recall that T_f settles to the temperature at the end point of glass transition upon cooling. Matching this settling temperature with the onset of the glass transition value provided by Busch et al. at the same rates, G_{str} is estimated as one tenth of the shear modulus $G_{str} = G/10$. Thus, all the components required by the Matsuoka model are set. The rate dependence of structure and trapped free volume with this formulation are shown in Figure 5.1, both in terms of normalized specific volume (part (a)), and fictive temperature (part (b)).

5.3 Volumetric Physical Aging Experiments for Vitreloy 1

5.3.1 Introduction

The required function for stress formulation is the volumetric relaxation modulus, $\mathbf{M}_V^r$. This is the critical reason volumetric structural recovery experiments are pursued here, even though enthalpy recovery is easier to measure. For example, studies on a very similar alloy, known as Vit.4, by Busch and Johnson [18] and Hammond et al. [37] use enthalpy recovery to quantify physical aging. In these studies [18, 37], Vit.4 was specifically chosen because it does not undergo phase separation [18] upon annealing, which is an issue for Vit.1 (see, e.g., the viscosity measurements by Waniuk et al. [89]). Phase separation destabilizes the amorphous state with respect to primary crystallization of nanocrystals [18]. In the enthalpy recovery studies, typically, the sample is annealed at a temperature under T_g and subsequently heated through glass transition at a constant rate. The material, then, draws more heat to recover the annealed out enthalpy upon its transition to the supercooled liquid. This results in a hysteresis in the cooling and heating curves of enthalpy. Consequently, during heating of the annealed sample, specific heat C_p (the temperature derivative of enthalpy) exhibits an overshoot at the glass transition before settling to the equilibrium liquid value. Similar hysteresis in volume and overshoot in the coefficient of thermal expansion (its normalized temperature derivative), too, occurs in this process although it is harder to measure.

The instrument used to investigate this behavior in Vit.1 is the thermomechanical analyzer whose sample chamber is shown in Figure 5.2. A quartz probe sits on the sample which is connected to an LVDT with 0.1 micrometer resolution. A flat edge probe is chosen for dilatometric studies to avoid intrusion into the sample. The load on the probe is set

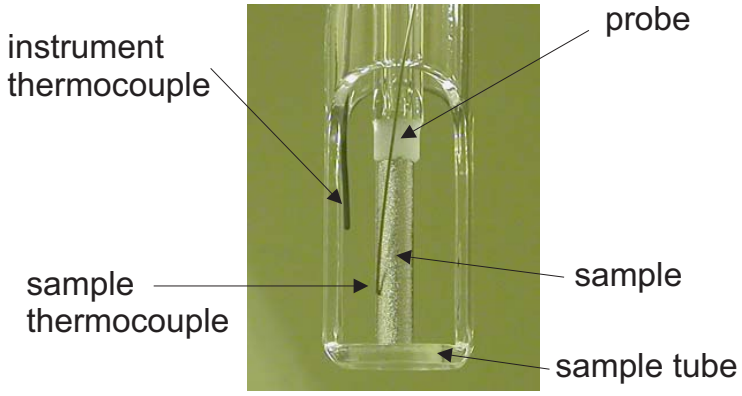

Figure 5.2: A photograph of a sample positioned in the TMA sample chamber. The probe is connected to a 0.1 micrometer sensitive LVDT. The furnace slides over the sample tube and the chamber is flushed by Helium. The instrument thermocouple facilitates temperature control whereas an additional (sample) thermocouple probe touches the sample for a direct measurement.

as 20 mN, the minimum value that could be attained with this particular instrument. A furnace slides on the sample tube shown in Figure 5.2 and the instrument thermocouple facilitates temperature control. An additional thermocouple probe with 0.025 mm diameter is used to monitor the exact sample temperature. The chamber is flushed with He gas to prevent oxidation.

As previously mentioned, volume recovery experiments involve very small changes in sample volume and require high instrument resolution. It is extremely difficult to directly quantify $\mathbf{M}_V^r$ as defined in Section 2.4, and the 0.1 micrometer resolution of TMA is not sufficient for such a measurement[1]. Kovacs' procedure [46] of heating samples to the super-cooled liquid region and instantly cooling to some temperature below T_g is also not feasible. The fastest cooling rate available in the TMA is 1 K/s, making 'instant' cooling impossible. Therefore, the following strategy is devised here to obtain volume recovery data that can

[1]Suppose the temperature jump is 5 K. The length of the sample is 13 mm and the structural CTE is 8.2×10^{-6} 1/K. Then, the span of recovery to be measured is ~ 0.5 micrometers and this allows merely 5 points to measure the function even when the noise at the same level is not considered.

be used to evaluate $\mathbf{M}_V^r$:

1. Design a casting procedure where Vit.1 is rapidly cooled with a measured temperature history that is uniform within the prospective samples.

2. Ramp the temperature in the TMA with the rate of 50 K/min and to a sub–T_g annealing temperature.

3. Measure the free volume relaxation during the isothermal hold at this temperature.

5.3.2 Specimen Preparation

The procedure of stainless steel (SS) tube casting has been described in Section 4.2.1. The casting here for preparing the TMA samples differs in two respects: (i) the geometry of the tube in the active (molding) section; (ii) the feeding of a thermocouple probe through the vacuum into the casting chamber.

A cross section of the mold region is shown in Figure 5.3(a). It comprises three rectangular chambers machined from an AISI 316 SS block using a wire electric discharge machine. The entire cross section is evacuated, and only the middle chamber is filled with Vit.1 melt when the assembly is heated to $\sim 900°$C. During the quench, the evacuated chambers on either side of the central melt inhibit heat transfer in the y direction. The cooling is thus dominated by the heat drawn form the top and bottom surfaces. The intent of this design is to render the heat transfer problem approximately 1-D, i.e., allow thermal gradients only in the x direction. Without insulating the sides, this would require casting a large plate, which is not possible with the current procedure (due to the fixed 50 mm diameter of the vertical furnace tube) and not desirable for it would require a very large amount of BMG alloy. The thickness, width and length (dimensions in x, y, z directions in this order) of the

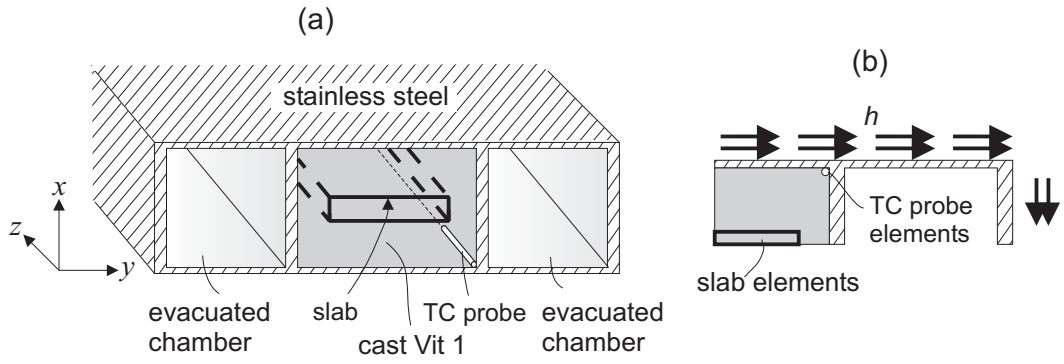

Figure 5.3: (a) Cross section of the designed SS mold that has three rectangular chambers. The middle chamber is filled with Vit.1 melt whereas the chambers on both sides remain empty. The thermocouple (TC) probe that is fed through the vacuum resides approximately in the corner of the cast BMG section. The thickness, width and length (dimensions in x, y, z directions, respectively) of this section are 12.7, 19, 127 mm, respectively. The slab that has been cut out for TMA measurements is shown with bold lines. (b) The 2-D geometry of the finite element heat transfer analysis of the quench. The convective heat transfer occurs from the free surfaces, shown in the figure with arrows and the heat transfer coefficient, h. The temperature history of the TC probe is obtained from FE analysis as the average response of the elements that reside in the cross section of the TC (TC probe elements). Similarly, the thermal history of the slab is averaged from the slab elements.

BMG beam cast in this way are 12.7, 19, 127 mm, respectively. The three-chamber mold is closed on one end whereas the other end is welded to a 600 mm long, 19 mm diameter tube of the same material. The open end of this assembly is connected to vacuum circuitry. This connection is outside the furnace tube and remains under $\sim$ 200°C during furnace operation. Therefore, we will call it the 'cold zone'.

To increase the cooling rate of the BMG section, the SS thickness on the top and bottom surfaces is kept to a mere 0.6 mm. Also, to promote the intensity of convection, the quenching water is salted with 15 volume pct. NaCl (brine quench), iced and stirred. The thermocouple probes are fed from the cold zone. A three-way connector is used to connect the tube to both the vacuum circuitry and a low-temperature thermocouple feed-through. The 120 mm long, fast response probes (0.5 mm diameter, type HKMTSS-020G with AISI 304 sheath from Omega Engineering, Stamford CT) are extended to the hot zone

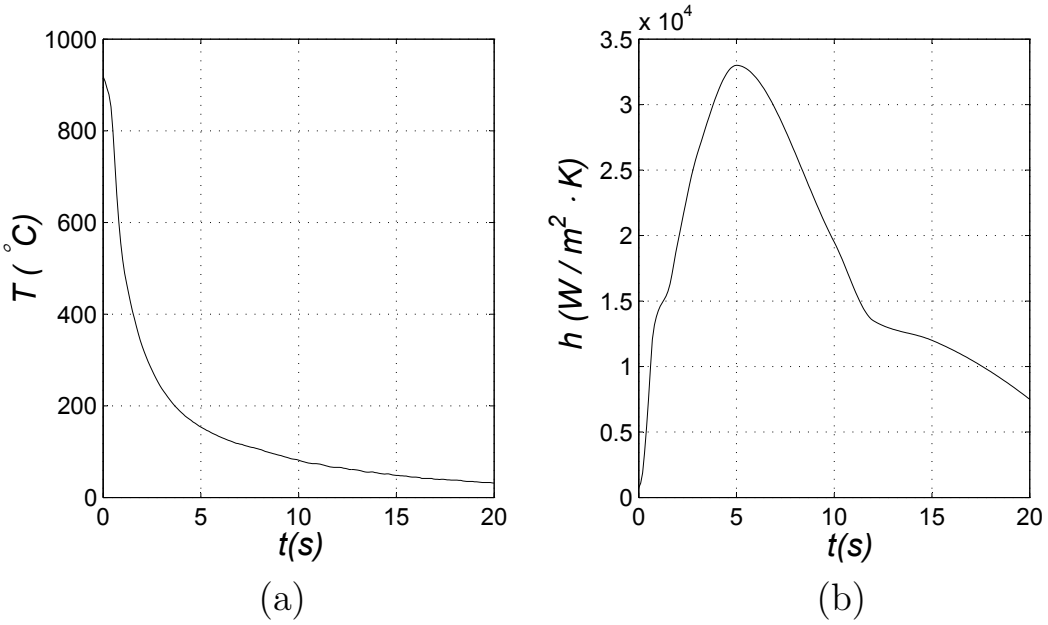

Figure 5.4: (a) Temperature vs. time data from the thermocouple. (b) Back-calculated time variation of the heat transfer coefficient, h.

from inside the tube. The grounded probe which envelopes the thermocouple wires and junction with a thin AISI 304 sheath could survive the hostile environment of the BMG melt and yield temperature data throughout the process. This temperature data is shown in Figure 5.4(a). At the end of the process, the probe is, naturally, cast in the BMG beam. The exact location of the probe tip is found out by sectioning (see Figure 5.3(a)). The temperature data are then used to solve the inverse problem: what heat transfer coefficient as a function of time would yield this temperature history at the thermocouple location? The analysis is implemented in ABAQUS$^{\text{TM}}$ and Figure 5.3(b) demonstrates the considered domain. Only a quarter of the casting section needs to be considered due to symmetry. The *AMPLITUDE option is used to vary the magnitude of h in time, by iteratively comparing the calculated thermocouple temperature with the experimental data. The thermocouple temperature from the FE analysis is taken as the mean temperature of the elements that lie in the thermcouple section. The heat transfer coefficient as a function of time obtained

in this manner is shown in Figure 5.4(b).

A 2.4 mm thick, 13 mm wide slab is cut out of the mid-plane of the beam as shown in Figure 5.3(a). Note that the thermal gradients in the x direction are smallest at the mid-plane where the slab is extracted. The temperature history of the slab is taken by averaging over the slab elements (see Figure 5.3(a)) upon the solution of the inverse problem.

Finally, TMA samples are cut off the slab in the x direction yielding 13 mm long samples with a 2.4×2.4 mm cross section.

5.3.3 Experimental Results and Discussion

Figure 5.5(a) shows the temperature history imposed on the sample for the isothermal hold temperature of 567 K. The first stage is the temperature history from the casting obtained by the procedure detailed in the previous section. Obviously, this stage determines the amount of free volume trapped within the material. The second stage involves the 50 K/min ramp in the TMA as the sample is taken to the annealing temperature. Finally, the third stage is merely the isothermal hold. This temperature history is input to the Matsuoka model and Figure 5.5(b) shows the resulting length variation normalized by its value at the start of the third stage, $l/l(0)$. Notice that the model accounts for the annealing of free volume during the ramp that is clearly visible just before the beginning of the isothermal stage. Also, when the heating ramp is continued without interruption until the supercooled liquid region, the curve which has deviated from the cooling curve merges back onto the equilibrium liquid line, realizing the aforementioned hysteresis. Figure 5.6 demonstrates the isothermal recovery data at 531, 548, 567 and 589 K in comparison to the model calculations in terms of normalized length vs. time. The agreement is clearly limited. It is qualitatively observed in the experimental data that as the annealing temperature increases, structural

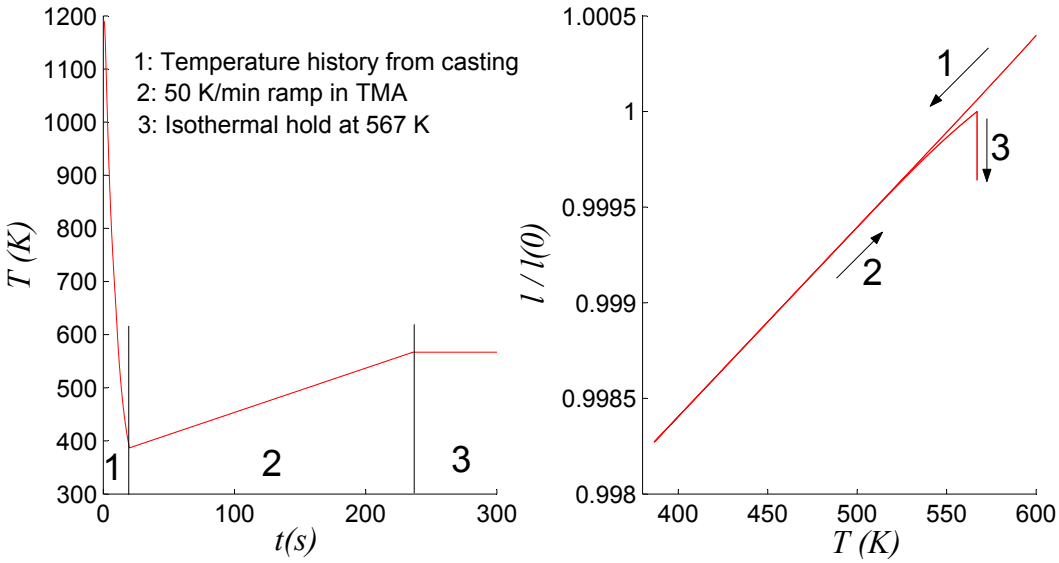

Figure 5.5: (a) The entire temperature history (temperature T vs. time t) of the sample that is composed of three stages: (1) the cooling during the casting, (2) 50 K/min ramp in the TMA, and (3) isothermal hold in the TMA (for this example) at 567 K. (b) Output of the Matsuoka model for this temperature history in terms of normalized sample length ($l/l(0)$) plotted vs. temperature. The three stages of temperature history are indicated on the figure with arrows.

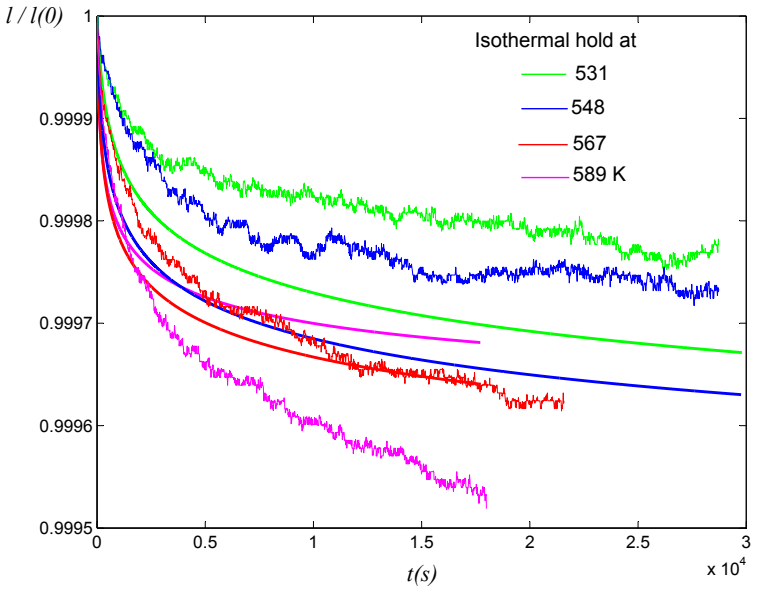

Figure 5.6: Length of the physically aged sample (l) normalized by its length at the beginning of the isothermal hold $l(0)$ plotted vs. time (t) at hold temperatures of 531, 548, 567, 589 K. Both the experimental data (noisy curves) and the calculations with the Matsuoka model (smooth curves) are presented with the same color for each temperature.

recovery becomes more rapid. However, since the magnitude of deviation from equilibrium, Δv, is higher as the temperature gets lower, eventually the higher temperature curves cross the lower temperature curves. For example, the model predicts that the 589 K curve crosses both the 567 and 548 K curves within the time scale of the experiment. However, the experimental data do not reveal any such intersections. Also, the experimental 'overall' relaxation time is roughly two orders of magnitude smaller than the model predictions. When the values of β_{str} and G_{str} in the model are varied within physical bounds, the agreement level does not improve significantly. Part of the problem may be phase separation for this alloy. Future studies will target better evaluation of the results with regards to the adequacy of the Matsuoka model and the phase separation phenomenon.

5.4 Stress Analysis

5.4.1 Introduction

Despite the limited experimental agreement, we take the Matsuoka model as a reasonable attempt to assess the magnitude of the structural effect for the thermal tempering of BMGs. The question as to whether there is a pronounced distribution of densities (trapped free volumes) across the specimen cross section (similar to the case in silicate glasses) is interesting and may be technologically important. Here, we consider again a Vit.1 plate that is cooled by a Biot number of $\tilde{B}i = \frac{h\,l}{k(T_g)} = 2$ (Section 3.3). The constitutive law is formed by the introduced fictive temperature and shift function (equations (5.1) and (5.2)), in addition to the viscoelastic shear relaxation law

$$s_{ij}(\mathbf{x},t) = \int_{-\infty}^{t} \mathbf{G}^r(\xi(\mathbf{x},t) - \xi(\mathbf{x},t')) \frac{\partial e_{ij}(\mathbf{x},t')}{\partial t'}\, dt' \tag{5.6}$$

and elastic dilatational response

$$\sigma_{kk} = K_0(\varepsilon_{kk}(\mathbf{x},t) - 3\varepsilon_\theta(\mathbf{x},t)) \tag{5.7}$$

where thermal strain ε_θ is given by equation (5.3). Recall from Section 2.5 that the addition of the structural model over the thermoviscoelastic one is twofold: (i) the stress generating thermal strain becomes dependent on structure (equation (5.3)) and, (ii) via the T_f dependent shift function relaxation time(s) depend on the structure.

5.4.2 Finite Element Implementation with ABAQUS^{TM} Software

The fictive temperature is defined as a field variable with the user subroutine USDFLD. The calculation of T_f at each integration point is performed by the Markovsky and Soules algorithm [56]. For finite element analysis, the computational time savings provided by this algorithm as opposed to the standard coupled solution become appreciable. The effect of fictive temperature on the coefficient of thermal expansion (the first effect above) is easily implemented in the input file by using the field variable dependence of CTE. For the effect of structure on relaxation times (the second effect) the user subroutine UTRS (that is for defining shift functions in ABAQUS^{TM}) is coded in accordance with equation (5.2). The output of the finite analysis has been verified with the previously used MATLAB^{TM} scripts. The aforementioned user subroutines are included in Appendix C.

5.4.3 Results

Due to the the fact that the differential between the initial temperature T_i and the glass transition temperature T_g is large ($\sim$ 650 K) in BMG processing, the results are surprisingly simple. Figure 5.7 plots the cooling rates (part (a)) and temperatures (part (b)) as a function of time for surface and mid-plane points. The cooling rates in Figure 5.7 reveal that when the temperature of the surface and mid-plane points drop to the vicinity of the glass transition region (at about 2.2 and 6.3 s, respectively), their cooling rates are very close in value ($\sim$ 70 K/s). This implies that the structure across the plate is almost uniform, as evidenced by small differences ($<$ 1 K) of the settled fictive temperatures. If T_i was sufficiently close to T_g, then the cooling rate at the surface would be much higher than that of the mid-plane as the surface temperature approached the glass transition region. This also explains the pronounced density difference observed between the surface and mid-plane

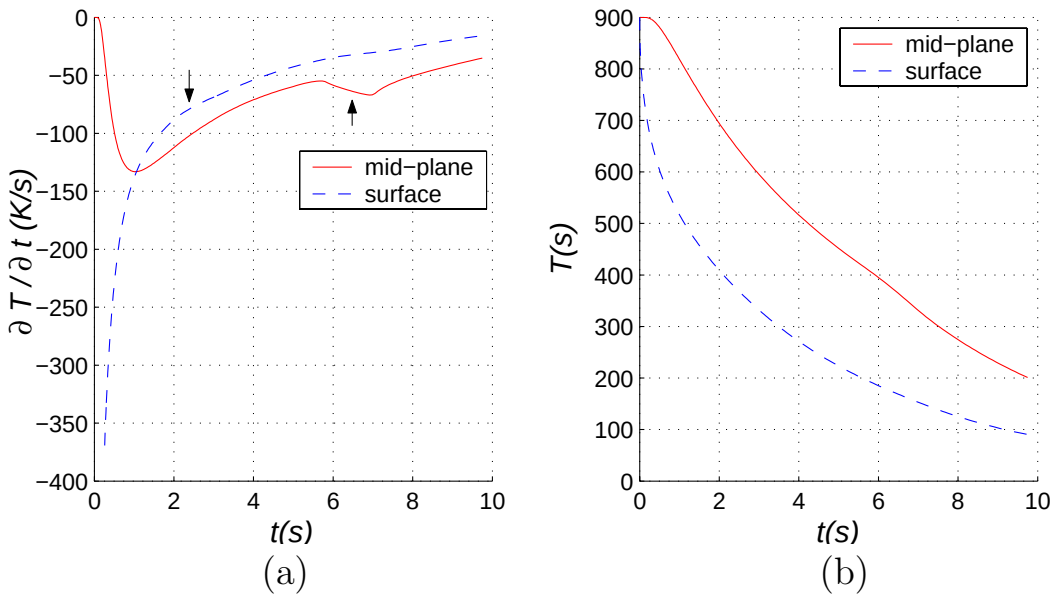

Figure 5.7: (a) Cooling rate and (b) temperature plotted vs. time at the mid-plane and surface points of a Vit.1 plate cooled with $\tilde{Bi} = 2$. The arrows in the first figure indicate the approximate moments when temperature drops to the glass transition range.

points in silicate glass tempering, a feature that is likely missing in BMGs.

Notice in Figure 5.7(a) that the intersection of the cooling rates of the surface and mid-plane points defines the point in time when thermal gradients begin to decay. At this instant, because the surface temperature is still above the glass transition range, the transient stresses are expected to be compressive on the surface (when considered with the fact that the structural effect is negligible). Figure 5.8 shows transient stresses at selected times that essentially agree with this conclusion. The opposite sense of transient stresses is another important difference of BMG tempering in comparison to silicate glass tempering.

The implemented structural model yields values of 98 MPa mid-plane tension and -254 MPa surface compression, representing only a small departure from the values given by the viscoelastic model: 98 MPa mid-plane tension and -241 MPa surface compression.

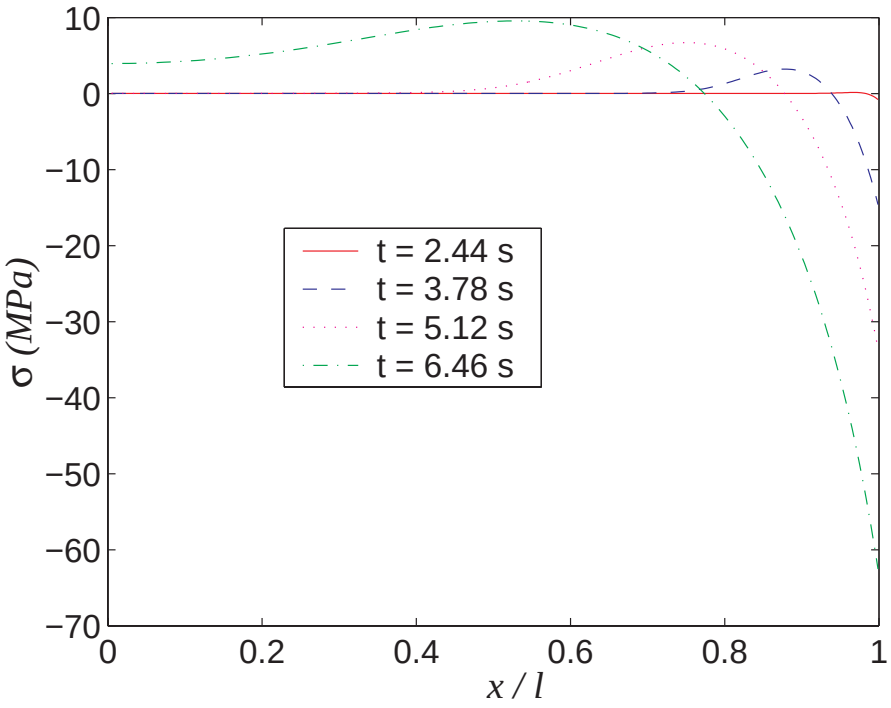

Figure 5.8: Transient stresses calculated by the structural model at selected times in the solidification stage.

Chapter 6

Conclusions and Future Work

A first-time analytical-experimental investigation is presented in this thesis on the rapid cooling induced residual stresses in a novel bulk metallic glass alloy, $Zr_{41.2}Ti_{13.8}Cu_{12.5}Ni_{10}Be_{22.5}$ (Vit.1). These stresses are called 'thermal tempering' stresses pertaining to the similar phenomenon in silicate glasses.

This thermomechanical problem has a two-stage structure. The first stage is the heat transfer problem that involves the determination of sample temperature as a function of time and position during the cooling process. Since the constitutive behavior is defined by the heat diffusion equation, the task here is to quantify (i) initial and boundary conditions, and (ii) precise thermal properties of the material. Then, these two are used to solve for temperature by numerical methods (e.g., the finite element method). For the former, a casting method is devised to prevent separation of BMG from the mold that allows a well defined convection problem. Then, the heat transfer coefficient in this process is measured. For the latter, experiments are conducted for thermal conductivity (the thermal parameter of primary importance in the thermal tempering problem) with the Van Der Pauw method for electrical resistivity and the flash method for thermal diffusivity. Since the material devitrifies in the supercooled liquid region, the properties in this range are extrapolated from the amorphous region data on the basis of physical formulations.

The second stage of the thermal tempering analysis is the mechanical problem which determines the stress evolution in the sample given the temperature solution. The mechanical problem requires modeling of the material behavior in addition to the experimental determination of stresses. The constitutive behavior is modeled at three levels of viscoelastic phenomenology using the instant freezing, viscoelastic, and structural models. The first is a simple analytical estimate for residual stresses and requires only the glass transition temperature as rheological input. The second is the temperature dependent thermoviscoelastic treatment that employs time-temperature superposition. The third accounts for the temperature history dependence of the glass structure. The constitutive laws for the viscoelastic and structural models are incorporated into the finite element method (ABAQUS^{TM} software package), allowing the application of these models to complex geometries. For implementation of the structural model, and to investigate the advanced rheological features of the material, structural volume recovery experiments are conducted with a Perkin Elmer TMA 7. The in-situ measurement of transient stresses during BMG casting is, yet, not possible. In fact, high-resolution, accurate measurement of residual stresses in these opaque and amorphous materials is challenging. The crack compliance method is determined as the ideal method to accomplish this goal, after evaluating few other methods such as the hole-drilling strain gauge method and the layer removal method. Also, the use of the non-destructive neutron diffraction method on a crystalline phase that is cast with a BMG sample is assessed in a model composite.

The following conclusions are drawn from these investigations:

- BMGs exhibit a pronounced increase in their thermal conductivity at high temperatures. For Vit.1, the room temperature thermal conductivity is $4.6\,\mathrm{W/(m\cdot K)}$ whereas it increases in an approximately linear fashion to $10\,\mathrm{W/(m\cdot K)}$ at 352°C (its glass

transition temperature), and to $20\,\mathrm{W/(m \cdot K)}$ at 900°C (the typical processing temperature used in casting). Accounting for the temperature dependence of thermal conductivity is crucial for the analysis; using the room temperature thermal conductivity for the entire temperature range results in a significant overestimate of stress magnitudes. It should be noted that the main source of this pronounced increase in thermal conductivity with temperature is the rise in the heat carried by electrons (the electronic component of thermal conductivity). The magnitude and temperature dependence of thermal conductivity constitute an important distinction between silicate glasses (typical thermal conductivity $\sim 1.4\,\mathrm{W/(m \cdot K)}$) and *metallic* glasses.

- Despite a higher thermal conductivity, significant stresses (up to 400 MPa surface compression) can still be introduced in BMGs with severe cooling, which involves heat transfer coefficients on the order of $10^4\,\mathrm{W/(m^2 \cdot K)}$, using the stainless steel tube casting method. Agreement within the accuracy of the temperature solution is obtained between the stresses calculated with the viscoelastic model and the measured values.

- Similar to silicate glasses, residual stresses in BMG tempering are quite insensitive to the details of material behavior around the glass transition region, indicated by the fact that the instant freezing, viscoelastic, and structural models all yield close results for residual stresses. The primary reason for this result is that the tempering process is dominated by the thermoelastic stresses that are generated after the material freezes.

- Due to the large differential between the initial temperature and the glass transition temperature during BMG casting (~ 550 K), thermal gradients, depicted by surface and center temperature difference, typically reach their maximum and start to decay

before temperatures across the sample thickness cool to the glass transition. This has two implications: (i) There is no transient tension on the surface and, therefore, even solidification stresses on the surface are compressive. (ii) The structure of the material or the trapped free volume below glass transition is fairly uniform through the cross section. In the case of silicate glasses, for which the initial temperature is close to the glass transition temperature, thermal gradients still grow at the solidification stage. For this reason, transient tension forms on the surface of a tempered silicate glass plate during solidification and after-process structure of the material exhibits pronounced variation across the thickness such that density increases from the surface to the mid-plane.

- By comparing experimental residual stress values with model predictions, it is shown that during copper mold casting with a low feed pressure, BMGs can separate from the mold cavity when most of the material is above the glass transition temperature.

- Temper stresses arise from thermal gradients around the glass transition. Therefore, residual stresses are good indicators of the cooling intensity in the casting process. Hence, measurement of residual stresses can be used to obtain an 'average' heat transfer coefficient for the process, using the stress vs. heat transfer coefficient plots in this thesis.

Following the investigations presented so far, the following items may be interesting future studies:

- An experimental study of the impact of the tempering stresses on the mechanical performance of the material (e.g., using bending or and uniaxial tension/compression tests). The interaction of the residual stresses with shear bands would be an interesting

study that can be investigated both for monolithic and composite BMG samples.

- In the investigation of the volumetric structural recovery, experiments yield limited agreement with the adopted Matsuoka model. Thus, a future investigation is necessary to evaluate the model and the impact of the phase separation phenomenon, which is commonly observed during the annealing of Vit.1.

- The viscoelastic pressure relaxation of the alloy is ignored in this study. The difficulty of conducting bulk relaxation experiments is apparent. Therefore, creep experiments, where the material is put under a constant pressure and the time dependent dilatation is measured, may be more convenient.

- The incorporation of the shear thinning effect into the present framework.

- The effect of feed pressure in copper mold casting is an interesting topic in terms of obtaining more efficient heat transfer and therefore higher residual stresses.

- As a side effect of fast quenching from the melt to room temperature, which involves a volumetric contraction of about 2%, pores might form in the center section of relatively thick BMG samples. Such defect formation needs to be analyzed for obvious technological reasons.

Appendix A

Material properties of $Zr_{41.2}Ti_{13.8}Cu_{12.5}Ni_{10}Be_{22.5}$

A.1 Thermal Properties

Thermal tempering is a thermomechanical problem where residual stresses arise in a traction-free sample due to temperature gradients during cooling. The heat produced through inelastic dissipation mechanisms is negligible in comparison to the heat drawn by forced cooling, therefore thermal problem is uncoupled from the mechanical problem. In this way, heat transfer problem is solved first to obtain the temperature field, $T(\mathbf{x}, t)$, and then this temperature field is imposed on the succeeding mechanical analysis.

Since the cause of stress generation is thermal gradients formed within the sample, the accurate prediction of stresses relies firstly on the accurate solution of the heat transfer problem and then on the correctness of the assumed mechanical behavior. Therefore, without rendering the error in the temperature solution small enough, it is not possible make a successful evaluation of the mechanical models (such as thermoviscoelastic, structural, etc.). Solution of the thermal problem requires identification of boundary conditions (e.g., the intensity of convective heat transfer), and also of the thermal properties of the material. These properties are thermal conductivity $k(T)$, specific heat $C_p(T)$ and density $\rho(T)$ which

are the material parameters in the heat diffusion equation $\nabla \cdot (k(T)\,\nabla T) = \rho(T)\,C_p(T)\,\frac{\partial T}{\partial t}$. The efforts to accurately determine boundary conditions are described elsewhere and this section details the data on thermal properties.

The task is difficult since the temperature range for the casting of $Zr_{41.2}Ti_{13.8}Cu_{12.5}Ni_{10}Be_{22.5}$ alloy is broad (typically around $(300, 1200)\,\mathrm{K}$), k and C_p exhibit pronounced temperature dependence in this range, and certain temperatures are unsuitable for property measurements due to crystallization or rigid sample requirement of the instruments. Moreover, considering only temperature dependence is still a simplification due to the kinetic phenomenon of glass transition. This was the motivation of structural theory that, for the stress problem, focused on viscosity and specific volume. For thermal parameters, however, such second-order dependence is disregarded to avoid superfluous complexity[1]. As a further justification, the residual stresses are completely insensitive to the heat transfer solution after kinetic freezing. Hence, it is rather critical to acquire the correct temperature evolution from casting temperature to the end point of glass transition (kinetic freezing). The dominant portion of this interval is, obviously, liquid and supercooled-liquid regions where mere temperature dependence suffices to determine the structure.

The following sections present property versus temperature data for each thermal property detailing the sources. In any of these tables, the value of the property at an intermediate temperature can be calculated by linear interpolation.

[1] In a case that rate dependence of thermal parameters is considered, the parameters would have to evolve with the temperature solution. Since, in general, every material point has different thermal history, this would mean iterative calculation at every material point. The rate-dependent material data that would make such consideration beneficial does not exist.

T	C_p	
(K)	(J/(g−atom · K))	(J/(kg · K))
300	24	400
450	25.5	425
500	26.5	441
550	28	466
602	29	483

Table A.1: Specific heat of $Zr_{41.2}Ti_{13.8}Cu_{12.5}Ni_{10}Be_{22.5}$ in the glassy region.

A.1.1 Specific Heat (C_p)

The references for C_p are the differential scanning calorimetry (DSC) studies by Busch et al. [19] and Fecht [32]. Busch et al. provide data for a set of cooling rates in the $(540, 720)$ K range. Samples are treated with a preliminary heat treatment to equalize their structure and then taken to the temperature of measurement from room temperature. Hence, the data for all samples are identical in the glassy region within experimental error. Fecht provides data for only a single cooling rate, but in a broader temperature range of $(320, 990)$ K, excluding 720 to 970 K where rapid crystallization precludes experiments. The data sets are in very good agreement in their overlapping portion of the glassy region. The data is reproduced in Table A.1 in units of J/(g−atom · K) (as it is provided in [19, 32]) and J/(kg · K). The error in these measurements are inferred to be around 0.7 J/(g−atom · K) (12 J/(kg · K)). In the supercooled liquid and liquid regions, Busch has given the following temperature dependence that fits the data successfully.

$$C_p^{liq} = 3R + (7.5 \times 10^{-3}\ T + \frac{8.17 \times 10^{-6}}{T^2})(\text{J/g}-\text{atom} \cdot \text{K}) \tag{A.1}$$

From this formula, the following Table A.2 is produced for the supercooled liquid and liquid regions.

T	C_p	
(K)	$(\mathrm{J/(g-atom \cdot K)})$	$(\mathrm{J/(kg \cdot K)})$
680	47.7	800
723	45.6	760
773	44.4	740
873	42.2	703
973	40.9	681
1073	40.1	668
1173	39.7	661

Table A.2: Specific heat of $Zr_{41.2}Ti_{13.8}Cu_{12.5}Ni_{10}Be_{22.5}$ in the supercooled liquid and liquid regions.

The end point of glassy region in Table A.1 (602 K) was picked as the onset of glass transition for the slowest cooling rate (0.0167 K/s) in the work of Busch et al. Similarly, the starting point of supercooled liquid region in Table A.2 (680 K) is taken as the end of glass transition for the fastest cooling rate(6.67 K/s). This means, the glass transition region, where C_p depends on temperature history, is excluded in the above data for the range of cooling rates considered by Busch et al. The transition between the two data sets is taken to be simply linear. Moreover, the glassy region data is, in fact, dependent on the frozen-in structure. In the actual cooling process, depending on the rapidness of cooling, the glassy region C_p would exhibit an offset over the data of annealed samples presented in Table A.1 (see e.g. [20]). Hence, with the justifications stated in the previous section, no attempt is made to strictly follow the actual curve(s) of C_p at and below the glass transition region, but to make the most reasonable approximation out of the available data.

A.1.2 Density (ρ)

It is interesting that for the room temperature density of this metallic glass, values used or reported in the literature range from 5.9 to 6.1 $\mathrm{g/cm^3}$. The degree of discrepancy here cannot be explained by merely the cooling rate dependence of density (or specific volume as it has

been elaborated in Chapter 2). It can perhaps be attributed to less careful measurements on this slowly varying property to obtain a nominal value and/or compositional variations. To the knowledge of the author, the most accurate data for the density of this alloy as a function of temperature is provided by Ohsaka et al. [66]. In this study, the specific volume of a nominally 2.2 mm diameter sphere has been measured in an electrostatic levitator as it cools (by natural radiative heat loss) from above 1300 K to 400 K. The volume measurements were made on the images of the sphere recorded on a CCD camera and the authors report an error of only 0.2% in this procedure. The best linear fits to the data in the liquid and glassy regions are given by

$$v_l = 0.1583 + 8.877 \times 10^{-6}\, T \ (\mathrm{cm}^3/\mathrm{g}) \quad (700 - 1300)\,\mathrm{K}$$

$$v_g = 0.1603 + 5.528 \times 10^{-6}\, T \ (\mathrm{cm}^3/\mathrm{g}) \quad (400 - 550)\,\mathrm{K}$$

and it is observed that the room temperature measurement (with a micrometer) lies along the v_g line. Density data resulting from these fits is given in Table A.3.

T(K)	ρ(g/cm^3)
300	6.174
550	6.122
700	6.079
1300	5.888

Table A.3: Density of $Zr_{41.2}Ti_{13.8}Cu_{12.5}Ni_{10}Be_{22.5}$ as a function of temperature.

Also, to provide more confidence, experiments were conducted by the author with the buoyancy principle based on the instructions in ASTM standard C693-93 [6] on a sample that was extracted out of the cast beam in Section 5.3.2. These measurements yielded a room temperature density of $6.15 \pm 0.03\,\mathrm{g/cm}^3$ in close agreement with Ohsaka et al.'s data.

A.1.3 Thermal Conductivity (k)

Thermal conductivity is the most important of the thermal parameters in the thermal tempering problem. This can be seen most clearly through the Biot number, $Bi = \frac{h\ l}{k}$, where l is the characteristic length and h is the convective heat transfer coefficient. Biot number largely determines[2] the extent of thermal gradients within the sample in a convective cooling process [41].

Temperature-dependent thermal conductivity measurements have been conducted by Snyder [80] in 1997 and, in a recent work, by Snyder and the author at Jet Propulsion Laboratory, Pasadena, CA. The measurements are done on two different setups.

The first setup is a high-temperature Hall-effect station that is used to measure the resistivity of the material with the Van Der Pauw method (see, e.g., the original article [88] and the related ASTM Standard F76-86 [8]) in an atmosphere-controlled furnace. The electrical conductivity, denoted by σ, is the reciprocal of resistivity. To understand the relation of these measurements to thermal conductivity, let us recall the following solid state physics arguments. For solids, thermal conductivity has two components. The first is the electronic component (k_e) which represents heat carried by the electrons. The second is the lattice part (k_l) which represents the heat carried by phonons. For metals, k_e is usually much bigger than k_l and it is related to electrical conductivity through *Wiedemann-Franz Law* (see, e.g., Kittel [45]). This law states that for metals at not too low temperatures the ratio of the thermal conductivity to the electrical conductivity is directly proportional to the tempera-

[2]The solution for the convective cooling of a simple geometry (e.g., slab or cylinder) with constant thermal parameters can be written as a series of spatial functions multiplied by time decay terms [16] and the spatial functions are independent of ρ and C_p. After the rapid decay of all the terms except the first one, the spatial solution, and therefore, thermal gradients, become independent of ρ and C_p. These parameters, via thermal diffusivity, merely affect the decay speed of the same temperature evolution. Certainly, when all the thermal parameters and boundary conditions are temperature-dependent this conclusion is not as sharp, but still of qualitative value.

ture. The constant of proportionality is called the Lorenz number L, given, thus, by $L \equiv \frac{k_e}{\sigma T}$ and under the assumptions of *free electron* theory, its value is $2.45 \times 10^{-8}\,\mathrm{W} \cdot \mathrm{ohm/K^2}$. Experimental values of L for several metal elements are listed in Kittel [45], ranging from 2.23 to $3.04 \times 10^{-8}\,\mathrm{W} \cdot \mathrm{ohm/K^2}$ at 273 K.

The samples used in resistivity measurements were nominally 1.2 mm thick, 14 mm diameter discs, which were machined parallel and flat within a tolerance of 0.01 mm. The setup provided high precision and room temperature resistivity was determined as $1.92 \pm 0.3 \times 10^{-6}\,\mathrm{Ohm} \cdot \mathrm{m}$ from measurements on several different samples and varying position of the contacts. In accordance with this, 1997 data and recent measurements are also in good agreement. It is observed that resistivity decreases (electrical conductivity increases) with temperature with a very modest slope. The linear fit to electrical conductivity in the $(293, 573)\,\mathrm{K}$ range yields

$$\sigma(T) = 6.99 \times 10^{1}\,T + 4.986 \times 10^{5}\ (\mathrm{m} \cdot \mathrm{Ohm})^{-1} \tag{A.2}$$

Therefore, k_e is approximately linear with temperature through Wiedemann-Franz Law. Assuming the theoretical value of Lorenz number, k_e values are calculated as $3.8\,\mathrm{W/(m \cdot K)}$ at room temperature and $7.5\,\mathrm{W/(m \cdot K)}$ at 573 K. As a side point, measurements were pursued also after crystallization that occurred around 700 K up to 925 K. Even after crystallization, which brought about a small drop, resistivity remained on a similar level (minimum value in this range is $1.55 \times 10^{-6}\,\mathrm{Ohm} \cdot \mathrm{m}$), implying a quite robust linear dependence of k_e on temperature.

The second setup is for thermal diffusivity ($\kappa = \frac{k}{\rho C_p}$) measurement[3] via the *Flash Method* (see, e.g., ASTM Standard E1461-92 [7]) and identical disc samples were utilized. The

[3]The setup is capable of measuring C_p as well, but less accurately than a DSC.

sample chamber is contained in an atmosphere-controlled furnace allowing high temperature measurements. Figure A.1(a) shows thermal diffusivity measurements. Sample 1 is tested

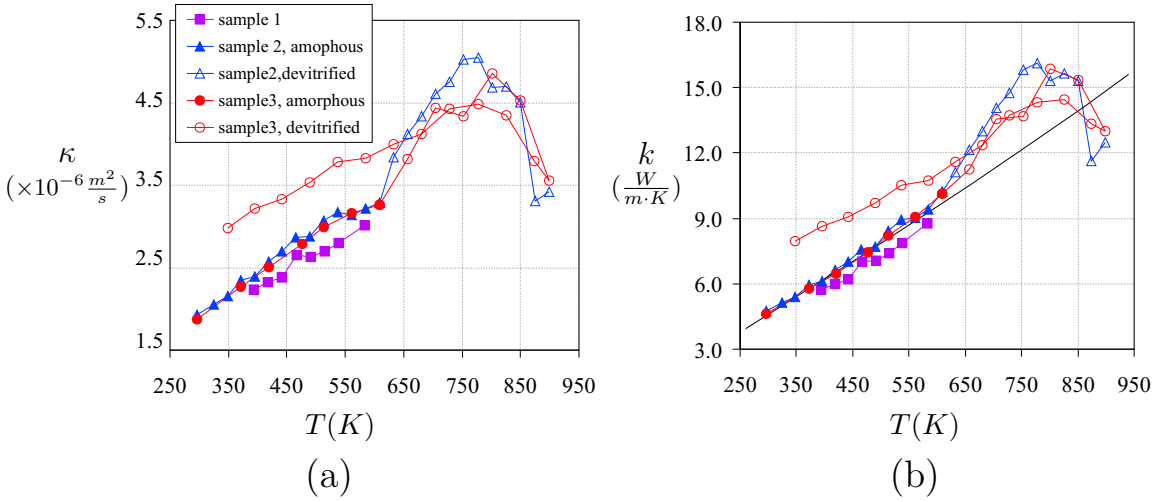

Figure A.1: (a)Thermal diffusivity, κ, data from experiments with the flash method, (b) Thermal conductivity, k, that is calculated as $k = \kappa\,\rho\,C_p$, the solid line is the fit detailed in the text. For both plots filled markers are for amorphous data points whereas empty markers of the same kind imply that the sample has devitrified.

in 1997, whereas samples 2 and 3 were recently tested. Sample 2 has been heated to above its melting temperature and lost its shape above 900 K, and the bad data points here are omitted. Sample 3 has been heated up to 900 K, but then cooled to yield data upon cooling as well. As seen on this figure, after smooth variation up to 608 K in the glassy region (this part of data is shown with solid symbols), κ exhibits a relatively big jump in its magnitude and slope, starting from the data point at 632 K. Although this temperature is slightly above the typical glass transition temperature, the jump is attributed to devitrification since the chamber furnace takes about 1200–1800 seconds to move from one measurement temperature to the other[4]. Therefore, data collected for samples 2 and

[4]The TTT diagram of the alloy (Masuhr et al. [57]) shows about $10^4 s$ at this temperature up to devitrification. However, two things should be considered here, (i) this TTT diagram has been produced by cooling from the melt, upon heating devitrification time drops significantly, (ii) the sample has been annealed in between the previous data points as well. Nevertheless, the samples, without doubt crystallize at a slightly higher temperature, say at 650 K, and the argument here is just against considering 632 K data point as amorphous.

3 after this point are for the devitrified material and they are shown with hollow symbols in the figure. In calculating the thermal conductivity from thermal diffusivity via $k(T) = \kappa(T) \cdot \rho(T) \cdot C_p(T)$, density and specific heat, values tabulated in the previous sections are used for the amorphous data. For the devitrified data points, $\rho(T)$ and $C_p(T)$ data for crystal phase are used that are taken from the same references, Ohsaka et al. [66] for density and Busch et al. [19] for specific heat. Figure A.1(b) shows thermal conductivity calculated in this way. Note, due to lower specific heat of the crystal, rise of thermal conductivity upon devitrification is much more gradual compared to thermal diffusivity. In the glassy region thermal conductivity of all samples agree well (particularly those of samples 2 and 3 which are from the same batch, and therefore, have similar 'memory') and the approximately linear temperature dependence is apparent. Below glass transition temperature, the cooling curve of sample 3 yields the thermal conductivity of the crystal which is significantly higher than that of the amorphous phase. This may possibly be attributed to higher lattice contribution k_l for the crystal.

Since, it has not been possible to make direct measurements for the thermal conductivity of the supercooled liquid and the liquid, due to devitrification and loss of sample shape, respectively, values for these regions need to be extrapolated from the amorphous region data. For this, thermal conducitivity is written as $k(T) = L\,\sigma(T)\,T + k_l$ where $\sigma(T)$ is given by equation (A.2) and slow variation of k_l with temperature is assumed. Least-squares fitting of the thermal conductivity data of the flash experiment samples to this equation yields L and k_l as $2.94 \times 10^{-8}\,\mathrm{W \cdot ohm/K^2}$ and $0\,\mathrm{W/(m \cdot K)}$, respectively. Fitting for the Lorenz number and lattice conductivity, this analysis utilized data from both experimental techniques. It was already apparent that k_e is the dominant over k_l comparing *free electron* values of k_e and measured k (e.g., 3.8 vs. $4.6\,\mathrm{W/(m \cdot K)}$ at room temperature), however

a zero k_l is not expected. Better resolution on the value of k_l may be obtained by direct measurement and/or evaluating sub-room-temperature measurements. Nevertheless, the error considered here is in how (total) thermal conductivity, k, is partitioned between k_e and k_l and its effect on the fit of k is limited. This fit is shown in Figure A.1(b) and values at representative temperatures are presented in Table A.4.

T(K)	k (W/(m · K))
273	4.16
473	7.39
673	10.80
873	14.36
1073	18.10
1273	21.99

Table A.4: Thermal conductivity of $Zr_{41.2}Ti_{13.8}Cu_{12.5}Ni_{10}Be_{22.5}$ as a function of temperature.

A.2 Mechanical Properties

Mechanical properties of Vit.1 are summarized in Table A.5. The references on elastic moduli are in Conner et al. [28]. Coefficient of thermal expansion (CTE) is not only a first-order parameter for stress generation but crucial for structural relaxation studies (Chapter 5). Its values above and below glass transition, liquid and glassy CTEs, respectively, are taken from the careful experiments by He et al. [39] with a TMA. The glassy CTE is rather straightforward to measure accurately with a TMA and the value by He et al. is verified with the instrument used in Chapter 5. The fit of Ohsaka et al. presented in Section A.1.2 is somewhat different in the glassy region(9.8 vs. 11.3 1/K), but this data is more noisy and TMA data is favored. ESL data needs to be checked rather in the liquid region since it allows the complete temperature range, which is not possible with the TMA, once more. due to devitrification and viscous flow. This value (17.7 1/K) is in good agreement with the

Young's modulus, E (GPa)	96 [28]
Poisson's ratio, ν	0.36 [28]
Room temperature yield strength, σ_y (MPa)	1900 [28]
Glassy CTE (1/K)	9.8 [39]
Liquid CTE (1/K)	18 [39, 66]

Table A.5: Mechanical properties for $Zr_{41.2}Ti_{13.8}Cu_{12.5}Ni_{10}Be_{22.5}$.

peak CTE value reported by He et al. (18.1 1/K), before devitrification occured. Therefore, we accept a value of 18 1/K for liquid CTE, here.

Appendix B

Residual Stresses in a Bulk Metallic Glass-Stainless Steel Composite

B.1 Introduction

Residual stresses in BMGs are difficult to measure directly with non-destructive methods. The amorphous nature of BMGs precludes the commonly used diffraction-based technique for residual stress measurement. However, it is possible to introduce a limited amount of crystalline phase into the BMG alloy and measure the residual elastic strain in it after processing. Then, the link between the strains measured in the crystalline phase and the stresses in the BMG can be established through mechanical modeling. This approach has been successfully employed in studying the in situ deformation behavior of BMG matrix composites with metallic inclusions (e.g., Dragoi et al. [31], Clausen et al. [26], Balch et al. [13, 14]). A similar approach is followed in the present study. A model cylindrical composite sample was produced under controlled conditions to evaluate the residual stresses in a BMG alloy. Due to its good interface strength and limited reactivity with most BMGs, stainless steel (SS) was used as the crystalline second phase. The residual strains in the steel were measured by neutron diffraction and compared with the results of a finite element (FE)

analysis. It is shown that significant residual stresses are induced in the SS/BMG composite and that neutron diffraction and FE can be effectively combined to evaluate and predict them.

The study also addresses the question on the constitutive behavior of SS that is used as a mold during the BMG casting process. This behavior is crucial in determining the stress state of the resulting BMG-SS composite. This question, however, was avoided in Chapter 4 by cutting out the SS tube and measuring the stresses in the monolithic BMG rod via crack compliance method. It has been demonstrated that any plausible mechanical behavior of SS, from zero to perfectly elastic stiffness, does not appreciably alter the final residual stresses in the BMG rod. Here, conversely, the sample is retained as a composite and the strain data is directly obtained from the SS sections.

This section is abridged from the paper by Aydıner et al. [10] and the user is referred to this reference for full details.

B.2 Experimental

The sample geometry is shown in Figure B.1. It consists of an AISI 314 stainless steel pin at the center (diameter: 3.2 mm), a tube of the same steel at the circumference (outer diameter: 19.0 mm, inner diameter: 15.6 mm) and a BMG alloy (Vitreloy 1) in between. The first step in the production of this specimen was the welding of an SS pin to the closed end of a 900 mm long SS tube. Next, the top end of the tube was connected to a vacuum line after pre-cast BMG ingots were put inside. The assembly was evacuated and placed in a vertical furnace where the BMG alloy melted at around 900°C and filled the volume between the pin and the tube. Finally, the composite was quenched in room temperature water. A 50 mm long section of the SS/BMG composite was then cut to obtain the specimen in Figure B.1.

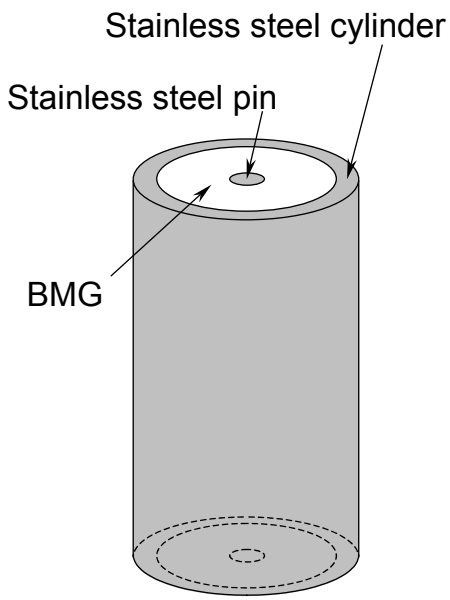

Figure B.1: Model specimen made of a type-314 stainless steel tube (19.0 mm outer diam., 15.6 mm inner diam.) and a middle pin (3.2 mm diam.) with a Vit.1 BMG cast in between. The specimen height is about 50 mm.

Other details of specimen preparation using this method were presented elsewhere. It is important to note that both SS/BMG interfaces were intact after processing. An identical tube (with an attached pin) was also heat treated under the same conditions, but without a BMG core, to be used as a stress-free reference in neutron diffraction measurements. The details of heat transfer coefficient determination were presented in Section 4.2.2. In the present study, additional experiments where the quench water was stirred with varied speeds showed that heat transfer is very weakly dependent on stream velocity (plausibly due to boiling convection [41]) and that the heat transfer coefficient varies between 8000 and $10000\,\mathrm{W/(m^2 \cdot K)}$ with an average value of $h = 9000\,\mathrm{W/(m^2 \cdot K)}$. These numbers were used in the FE calculations. Neutron diffraction provided a non-destructive measure of the residual strains in the steel components. The use of this technique at a reactor source and specifically at the Missouri University Research Reactor Centers 2XD powder

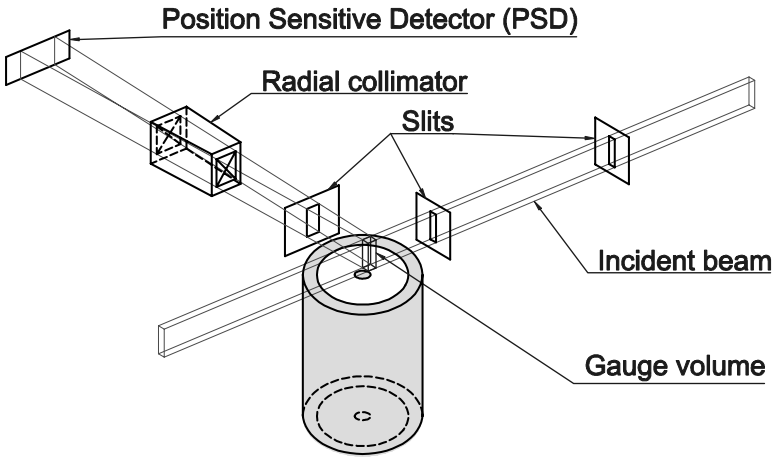

Figure B.2: Schematic of the 2XD neutron diffractometer at the Missouri University Research Reactor Center. The sampling (or gauge) volume is defined by slits in the incident and diffracted beams to be about $1 \times 1 \times 8$ mm^3.

diffractometer. Measurements were performed using a monochromatic neutron beam of wavelength, $\lambda = 1.478\,\text{Å}$ and a position sensitive detector (PSD). The 311 stainless steel peak at $2\theta = 86.6^\circ$ was employed. The gage volume was a rectangular box of $1 \times 1 \times 8$ mm^3 defined by incident and diffracted beam slits (see Figure B.2). An oscillating radial collimator was used on the diffracted beam to reduce sources of background neutrons. The residual strain was obtained from the difference in the 311 lattice spacings of the composite and the stress-free reference sample. The uncertainty in experimental strain data (obtained from 4 repeated measurements on the reference sample) is estimated at $330\,\mu\epsilon$ (where $\mu\epsilon = 10^{-6}$ strain), mostly due to the translation error.

B.3 Modeling

The thermoviscoelastic model detailed in Section 4.3.2 is used for BMG along with the material data in Appendix A. The elastic constants and thermal parameters of AISI 314 are taken from Metals Handbook [4] whereas the plastic data is shown in Table B.1. It is well

	Temperature (K)	σ_Y (MPa)	$\sigma_{T,Tensile}$ (MPa), $\varepsilon_{T,p}$
CASE 1	298	205	721, 0.332
CASE 2	298	310	868, 0.332
CASE 3	294	358	1105, 0.498
	700	276	804, 0.346
	811	248	758, 0.355
	866	224	665, 0.297
	1033	138	450, 0.530
	1089	103	259, 0.407
	1144	90	274, 0.575

Table B.1: Temperature-dependent plastic behavior of AISI 314 stainless steel for three cases considered. σ_Y: Yield strength, $\sigma_{T,Tensile}$: true stress at the ultimate tensile strength, and $\epsilon_{T,p}$: the corresponding plastic component of true strain. The reference for Case 1 and Case 2 is Metals Handbook [4] whereas the data of Case 3 is from the report by Simmons and Cross [79].

known that the plastic behavior of stainless steels is strongly dependent on heat treatment, sample dimensions and geometry. As a result, a wide range of plasticity data exist for the AISI 314 steel. Therefore, the constitutive behavior of the SS was regarded a parameter in the present analysis and three data sets were considered. As will be shown, such a parametric study also helps with the understanding of the model predictions sensitivity to the constitutive behavior of the SS, which could not be determined in situ during this investigation. The first two cases listed in Table B.1 are room temperature test results whereas the third case includes high temperature data as well [4, 79]. The data are presented in Table B.1 in terms of yield strength (σ_Y), true stress at the ultimate tensile strength ($\sigma_{T,Tensile}$) and the corresponding plastic component of true strain ($\epsilon_{T,p}$), the way they were used in the FE calculations. The latter two quantities specify the hardening behavior. The analysis assumed von Mises plasticity with isotropic hardening. The FE implementation was in principle identical to the sequential thermal mechanical analysis of Chapter 4 and

the case specific details and discussion are given in [10].

B.4 Results

Axial elastic strain results from neutron diffraction and five different FE model predictions are presented in Figure B.3. In all but one FE model (namely, 'Elastic SS, BMG (CTE)'), the constitutive behavior of the BMG was described by the thermoviscoelastic model. In the latter case, both SS and BMG were considered linear elastic and no thermal gradients were allowed. Therefore, the only residual stress source in this case is the CTE mismatch between the two phases below 352°C (the glass transition temperature of BMG). This case was considered to highlight the effect of temperature gradients in the residual stress state of the composite. It is obvious in Figure B.3 that if CTE mismatch were the only source of residual strain in this composite, then the axial strains in the pin and the tube would be identical and quite different than the experimental data. In all the other four FE models the BMG behaved as a viscoelastic material, but the constitutive behavior of the SS varied from a linear elastic material ('Elastic SS'), to one with a room temperature yield strength of $(\sigma_Y)_{SS} = 205$ MPa (Case 1), or $(\sigma_Y)_{SS} = 310$ MPa (Case 2), and finally for Case 3, with a high yield strength at room temperature, $(\sigma_Y)_{SS} = 358$ MPa which decreases at higher temperatures (see Table B.1 for additional details). Note that the first two cases assume no variation of SS yield strength as a function of temperature.

Diffraction data exhibited a high tensile residual strain in the SS pin ($+1420\,\mu\epsilon$) and a low compressive strain in the tube ($-140\,\mu\epsilon$), both in the axial direction. A straight line was used to show the ND result for clarity although the measurement was taken from one location, 1 mm wide in the radial and hoop directions. The measurement in the pin is insensitive to the exact radial location of the sampling volume since the model calcula-

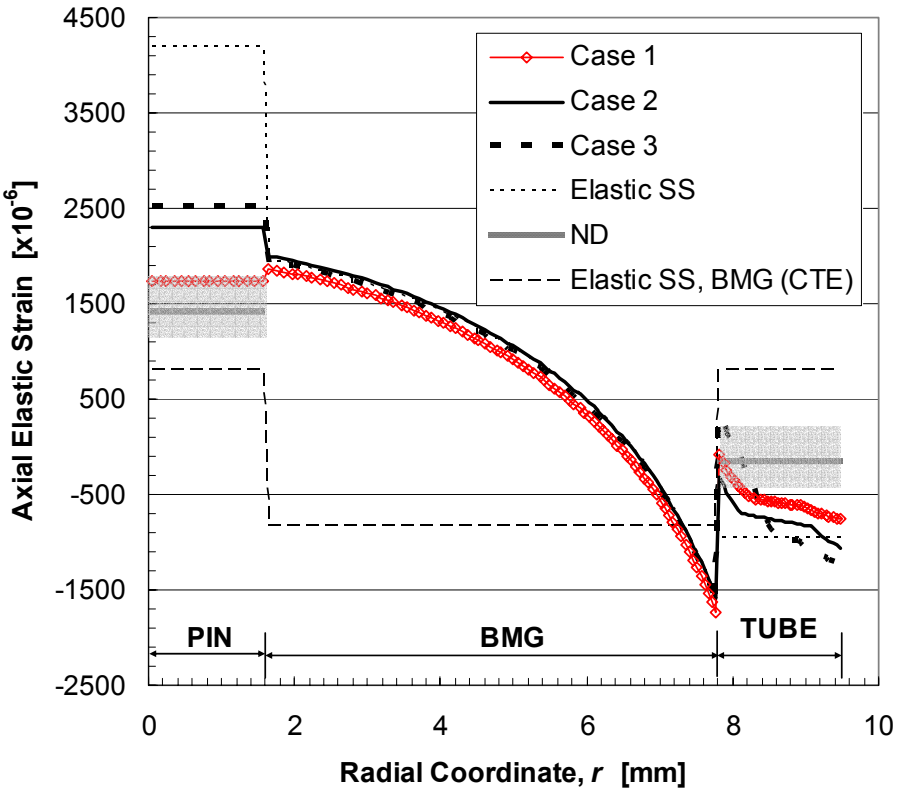

Figure B.3: Axial elastic strains measured by neutron diffraction (ND) and calculated for different constitutive behaviors of stainless steel (SS) and BMG: Case 1: $(\sigma_Y)_{SS} = 205$ MPa, BMG viscoelastic; Case 2: $(\sigma_Y)_{SS} = 310$ MPa, BMG viscoelastic; Case 3: $(\sigma_Y)_{SS} = 358$ MPa at room temperature and drops at higher temperatures (Table B.1), BMG viscoelastic; 'Elastic SS': SS linear elastic, BMG viscoelastic; 'Elastic SS, BMG (CTE)': both phases are linear elastic, no thermal gradients allowed (CTE mismatch is the only residual stress source). The shaded areas represent the error bars for the ND data ($330\,\mu\epsilon$).

tions yielded almost uniform elastic strain in it. The variation in the tube is much more pronounced. The primary reason is that the pin, being at the center, never experienced severe temperature gradients within itself. When it yielded, plastic deformation was uniform and due to the loads exerted by the remaining section of the sample. Conversely, the tube underwent non-uniform plastic deformation even before metallic glass solidified due to high thermal gradients within its wall. Such deformation was especially pronounced in Case 3 where high temperature softening of SS was considered. Note that when plastic deformation was prevented (the 'Elastic SS' case), the strain distribution in the tube, too, became uniform (Figure B.3).

The ND data from the pin had a better signal-to-noise ratio. In addition, since the pin carries uniform axial strain, it is more advantageous in comparing the experimental data with model predictions. Therefore, the following discussion will concentrate only on the pin. When the FE calculations are compared with each other, the obvious trend is more elastic strain in the pin as room temperature yield strength increases. The extreme point is the fictitious elastic SS calculation which represents infinite yield strength. A simple explanation for this result is that the majority of the residual stresses are generated after the BMG completely 'solidifies', since the pin-BMG interface should be able to transfer load to the pin. If the 'solidification' or 'setting' of the BMG is assumed to occur at 352°C (its glass transition temperature), the maximum temperature at this instant at the center of the pin is only slightly higher (362°C) according to the heat transfer solution. As mentioned earlier, the pin does not yield due to thermal gradients within itself before the 'setting' of the BMG. Therefore, no significant high temperature plastic deformation is expected in the pin and the low temperature plastic properties of the SS essentially control the stress level in the pin. Indeed, when high temperature softening was deleted from the input file of Case

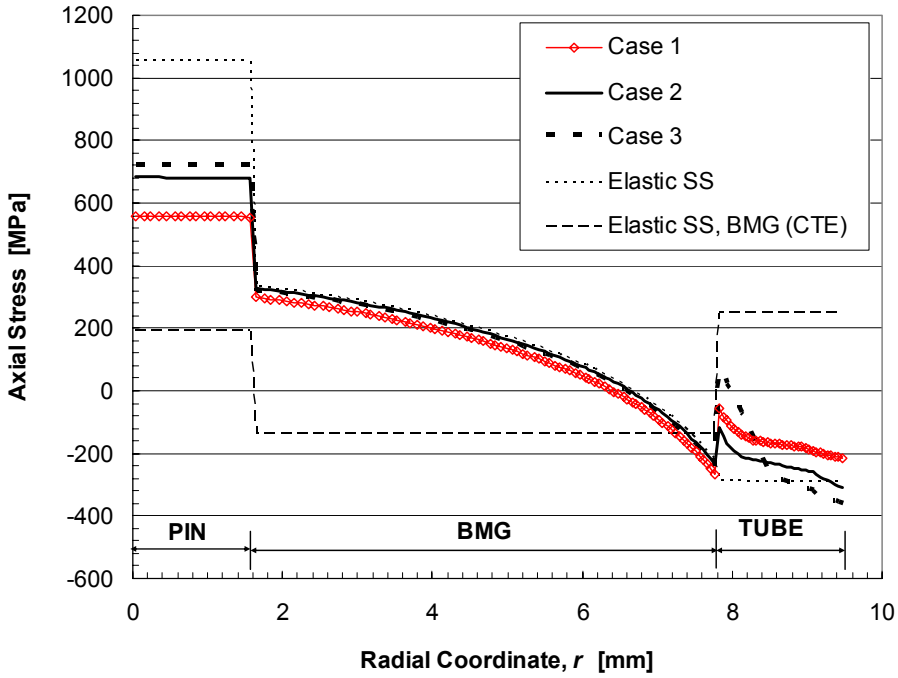

Figure B.4: Axial stresses predicted by the FE model for various constitutive behaviors of SS and BMG (see the caption of Figure B.3 for details).

3 and the calculation was repeated, the results (not shown) were not significantly affected. This means, an accurate calculation of residual strains in the pin requires exact information about the plastic behavior of the SS only around room temperature. This result eliminates the influence on the final residual stresses of the high temperature constitutive behavior of the SS, an unknown in the present study. Although the exact heat treatment (and hence the room temperature plastic behavior) of the SS during the composite processing is not known, it can be reasonably speculated that it approaches Case 1 (i.e., yield strength around 200 MPa) judging from the proximity of the model predictions for this case to the ND data in the pin (Figure B.3).

Figure B.4 presents the axial residual stresses in the composite. The parabolic shape of the stress distribution in the BMG is typical of thermal tempering. In Figure B.4, it is obvious that the stress profile in BMG is not influenced appreciably by the constitutive

behavior of SS. Here, the temper level can be expressed as the difference between the end points of this parabola ($\sim$ 560 MPa). In a tempered, monolithic BMG surface compression to mid-plane tension ratio is around 2. Hence, the temper level attained in the present study corresponds to about +190 MPa mid-plane tension and −380 MPa surface compression in a monolithic BMG sample. This result again proves that BMGs can build significant residual stresses due to thermal tempering. It is worth noting that the SS/BMG composite studied here is a tempered product, too, as the surface compressive axial stress in the SS tube reaches −200 MPa (Figure B.4).

Appendix C

ABAQUS Subroutines for Structural Model

```
      SUBROUTINE USDFLD(FIELD,STATEV,PNEWDT,DIRECT,T,CELENT,TIME,DTIME,
     1 CMNAME,ORNAME,NFIELD,NSTATV,NOEL,NPT,LAYER,KSPT,KSTEP,KINC,
     2 NDI,nshr,coord,jmac,jmtyp,matlayo,laccflg)
C
      INCLUDE 'ABA_PARAM.INC'
c 11-28-2003
c I have deleted the debug write's

c 11-26-2003
c reproduction of markovsky and soules algorithm 1984 in calculating
c the fictive temperature, in this version i'll verify the single
c relaxation time fictive temperature, then i may care about putting
c the multiple relaxation time formulation implemented by partial
c fictive temperatures. having one field variable per each might be
c a good idea.

c the previous version outputs the derivative of the thermal strain
c to set the coefficient of thermal expansion in a table definition
c however, all those arguments were for a tangent sense coefficient of
c thermal expansion which is the only notion I had, ABAQUS on the other
c hand uses a chord type CTE(see Chapter 12.1 in Standard Manual to see
c what I mean:

c so let me formulate things again

c the thermal strain from the initial temperature is given by
c eT = alphaL * (Tf-Ti)+ alphaG * (T-Tf)
c    = alphaG * (T-Ti) + alphaS * (Tf-Ti)

c since alphaABQ = abaqus definition of CTE is not in integral sense
c but simply eT = alphaABQ*(T-Ti), we can get alphaABQ as
c                alphaABQ = alphaG + alphaS* (Tf-Ti)/(T-Ti)
```

```
c so this form is identical to what you have with the tangent formulation
c except instead of dTf/dT you end up with (Tf-Ti)/(T-Ti) as your second
c field variable.

c Also this version is adapted for use in the VFT fit of BMG, through
c Matsuoka's formulation. I have to use exactly the same parameters as in
c UTRS of course. Note now I have to use UTRS since there is
c dependence on fictive temperature, the first field variable.
c since this formulation uses the parameters of the arhenius shift
c function the shift function specified in UTRS should have exactly
c the same parameters for consistency.


C MATERIAL PARAMETERS
      PARAMETER(DSTART0=7631.25,TREF=800,TERMTREF=2.580645E-3)
      PARAMETER(T0=412.5, TAUREF=4.0465E-6)
C TAUREF is the structural relaxationtime at TREF so it is calculated from a
C a different moduli, this time 10 times smaller then G so TAUREF is 10 times
C bigger
      PARAMETER(TI=900)
C !!!!!!!!!!! TI is in degC. initial temperature should be the same as in
C the analysis.
C
      CHARACTER*80 CMNAME,ORNAME
      CHARACTER*8  FLGRAY(15)
      DIMENSION FIELD(NFIELD),STATEV(NSTATV),DIRECT(3,3),T(3,3),TIME(2),
     *  coord(*),jmac(*),jmtyp(*)
      DIMENSION ARRAY(15),JARRAY(15)
C

c I can use PNEWDT to keep DTIME constant and do even more
c complicated solution dependent stuff on adjusting PNEWDT
c yet now all I need is constant intervals and I'll achieve that
c by sending setting the maximum and initial increments to the same
c small value in the input file

c the explicit formula of the algorithm requires the current
c temperature, the temperature in the previous increment and fictive
c temperature in the previous increment.

c i have to keep the temperature and fictive temperature
c of the previous increment stored
c somewhere in other words store the temperature in this increment for
c use in the next increment let me use a solution dependent state
c variable for that

c for the first two calls (two increments), time is zero so there
```

```
c is nothing to do but take the initial values
c and set them to the solution-dependent variables,

c first inc first inc first inc
      IF ((TIME(1).EQ.0.).AND.(KSTEP.EQ.1)) THEN
          CALL GETVRM('TEMP',ARRAY,JARRAY,FLGRAY,jrcd,
     $     jmac, jmtyp, matlayo, laccflg)
          TEMP1 = ARRAY(1)
          STATEV(1)=TEMP1
c the fields have been initialized in the input file
          STATEV(2)=FIELD(1)
c simply return now
          RETURN
      ENDIF

c for next increments first call the state variables with GETVRM
      CALL GETVRM('SDV',ARRAY,JARRAY,FLGRAY,jrcd,
     $     jmac, jmtyp, matlayo, laccflg)

      TEMP0=ARRAY(1)
      TEMP0K = TEMP0 + 273.

c exactly the same thing for fictive temperature of the previous step

      FICTIVETEMP0 = ARRAY(2)
      FICTIVETEMP0K = FICTIVETEMP0 + 273.

      CALL GETVRM('TEMP',ARRAY,JARRAY,FLGRAY,jrcd,
     $     jmac, jmtyp, matlayo, laccflg)
      TEMP1 = ARRAY(1)

      TEMP1K=TEMP1 + 273.

c get fictive temperature which is the field variable.

      FACTOR=EXP(DSTART0*(-(FICTIVETEMP0K/TEMP0K)/(FICTIVETEMP0K-T0)
     $ + TERMTREF))

      FICTIVETEMP1K = (TAUREF*FICTIVETEMP0K+TEMP1K*DTIME*FACTOR)/
     $ (TAUREF+DTIME*FACTOR)


      FICTIVETEMP1 = FICTIVETEMP1K - 273.
      FIELD(1) = FICTIVETEMP1

c second field variable:
c calculate (Tf-Ti)/(T-Ti), make sure TI is set right in degC,
```

```
c the same as in the problem

      FIELD(2) = (FICTIVETEMP1 - TI)/(TEMP1-TI)

c now update the old guys for the next step, both in degC.

      STATEV(1)=TEMP1
      STATEV(2)=FIELD(1)

c if error, write comment to .DAT file:

      IF(jrcd.NE.0) THEN
       WRITE(6,*) 'REQUEST ERROR IN USDFLD FOR ELEMENT NUMBER ',
     1   NOEL,' INTEGRATION POINT NUMBER ',NPT
      ENDIF

      CLOSE(UNIT=16)

      RETURN
      END

C     I KEEP THE TEMPERATURES IN K HERE, SINCE IN THE PROBLEM
C     THEY ARE IN DEGC, THERE IS THE CONVERSION FIRST. IN
C     MATSUOKA ABSOLUTE TEMPERATURE GOES IN THE FORMULATION
C     AT ONE POINT SO IT HAS TO BE DONE.
C     IN THE ACCOMPANYING ROUTINE USDFLD FICTIVE TEMPERATURES ARE
C     KEPT ALSO INPUT IN DEGC, CONVERTED TO K, USED AND OUTPUT IN
C     DEGC SO THAT I AM CONSISTENT WITH MY CONVERSIONS.

C     INTO THE ROUTINE-> DEGC, CONVERT TO K, USE, OUTPUT BACK IN
C     DEGC

      SUBROUTINE UTRS(SHIFT,TEMP,DTEMP,TIME,DTIME,PREDEF,DPRED,
     1 STATEV,CMNAME,COORDS)
C
      INCLUDE 'ABA_PARAM.INC'

C MATERIAL PARAMETERS
      PARAMETER(DSTART0=7631.25,TREF=800,TERMTREF=2.580645E-3)
      PARAMETER(T0=412.5)
C TREF is in K , TERMTREF=1/(TREF-T0)
C
C
      CHARACTER*80 CMNAME
C
      DIMENSION SHIFT(2),TIME(2),PREDEF(1),DPRED(1),STATEV(1),
     1 COORDS(1)
```

```
C
      TEMP0=TEMP-DTEMP
      TEMP0K = TEMP0 + 273.

      TEMP1=TEMP
      TEMP1K = TEMP1 + 273.

      FICTIVETEMP0 = PREDEF(1) - DPRED(1)
      FICTIVETEMP1 = PREDEF(1)

      FICTIVETEMP0K = FICTIVETEMP0 + 273.
      FICTIVETEMP1K = FICTIVETEMP1 + 273.

      TREL0= (FICTIVETEMP0K/TEMP0K)/(FICTIVETEMP0K-T0)-TERMTREF
      TREL1 = (FICTIVETEMP1K/TEMP1K)/(FICTIVETEMP1K-T0)-TERMTREF
C
      H0 = DSTART0 * TREL0
      H1 = DSTART0 * TREL1
      IF (H0.LE.100.) THEN
        SHIFT(1)=EXP(H0)
      ELSE
        SHIFT(1)=EXP(50.)
      ENDIF
      IF (H1.LE.50.) THEN
        SHIFT(2)=EXP(H1)
        ELSE
      SHIFT(2)=EXP(50.)
      ENDIF
      RETURN
      END
```

Bibliography

[1] *Metals Handbook (desk ed.)*. American Society for Metals, Metals Park, OH, 1985.

[2] G. Adam and J. H. Gibbs. On temperature dependence of cooperative relaxation properties in glass-forming liquids. *Journal of Chemical Physics*, 43(1):139–146, 1965.

[3] B. D. Aggarwala and E. Saibel. Tempering stresses in an infinite glass plate. *Physics and Chemistry of Glasses*, 2(5):137–140, 1961.

[4] American Society for Metals. *Metals Handbook*, volume 3, Metals Park, OH, 1978.

[5] C. A. Angell. Formation of glasses from liquids and biopolymers. *Science*, 267(5206):1924–1935, 1995.

[6] ASTM, West Conshohocken, PA. *Standard Test Method for Density of Glass by Bouyancy, ASTM Standard C693-93*, 2001.

[7] ASTM, West Conshohocken, PA. *Standard Test Method for Thermal Diffusivity of Solids by the Flash Method, ASTM Standard E1461-92*, 2001.

[8] ASTM, West Conshohocken, PA. *Standard Test Methods for Measuring Resistivity and Hall Coefficient and Determining Hall Mobility in Single Crystal Semiconductors, ASTM Standard F76-86*, 2001.

[9] C. C. Aydıner and E. Üstündag. Residual stresses in a bulk metallic glass cylinder induced by thermal tempering. Submitted to *Mechanics of Materials*, 2003.

[10] C. C. Aydıner, E. Üstündag, B. Clausen, J. C. Hanan, R. A. Winholtz, M. A. M. Bourke, and A. Peker. Residual stresses in a bulk metallic glass-stainless steel composite. Submitted to *Materials Science and Engineering A*, 2003.

[11] C. C. Aydıner, E. Üstündag, and J. C. Hanan. Thermal-tempering analysis of bulk metallic glass plates using an instant-freezing model. *Metallurgical and Materials Transactions A*, 32(11):2709–2715, 2001.

[12] C. C. Aydıner, E. Üstündag, M. B. Prime, and A. Peker. Modeling and measurement of residual stresses in a bulk metallic glass plate. *Journal of Non-Crystalline Solids*, 316:82–95, 2003.

[13] D. K. Balch, E. Ustundag, and D. C. Dunand. Diffraction strain measurements in a partially crystallized bulk metallic glass composite containing ductile particles. *Journal of Non-Crystalline Solids*, 317(1-2):176–180, 2003.

[14] D. K. Balch, E. Ustundag, and D. C. Dunand. Elasto-plastic load transfer in bulk metallic glass composites containing ductile particles. *Metallurgical and Materials Transactions A*, 34A(9):1787–1797, 2003.

[15] B. A. Boley and J. H. Weiner. *Theory of Thermal Stresses*. Wiley, New York, NY, 1960.

[16] W. J. Brown and R. V. Churchill. *Fourier Series and Boundary Value Problems*. McGraw-Hill, New York, NY, fifth edition, 1993.

[17] H. A. Bruck, T. Christman, A. J. Rosakis, and W. L. Johnson. Quasi-static constitutive behavior of Zr41.25Ti13.75Ni10Cu12.5Be22.5 bulk amorphous-alloys. *Scripta Metallurgica Et Materialia*, 30(4):429–434, 1994.

[18] R. Busch and W. L. Johnson. The kinetic glass transition of the Zr46.75Ti8.25Cu7.5Ni10Be27.5 bulk metallic glass former-supercooled liquids on a long time scale. *Applied Physics Letters*, 72(21):2695–2697, 1998.

[19] R. Busch, Y. J. Kim, and W. L. Johnson. Thermodynamics and kinetics of the undercooled liquid and the glass-transition of the Zr41.2Ti13.8Cu12.5Ni10.0Be22.5 alloy. *Journal of Applied Physics*, 77(8):4039–4043, 1995.

[20] R. Busch, Y. J. Kim, W. L. Johnson, A. J. Rulison, W. K. Rhim, and D. Isheim. Hemispherical total emissivity and specific-heat capacity of deeply undercooled Zr41.2Ti13.8Cu12.5Ni10.0Be22.5 melts. *Applied Physics Letters*, 66(23):3111–3113, 1995.

[21] R. Busch, A. Masuhr, and W. L. Johnson. Thermodynamics and kinetics of Zr-Ti-Cu-Ni-Be bulk metallic glass forming liquids. *Materials Science and Engineering A*, 304:97–102, 2001.

[22] W. Cheng and I. Finnie. A method for measurement of axisymmetric axial residual-stresses in circumferentially welded thin-walled cylinders. *Journal of Engineering Materials and Technology*, 107(3):181–185, 1985.

[23] W. Cheng and I. Finnie. A comparison of the strains due to edge cracks and cuts of finite width with applications to residual-stress measurement. *Journal of Engineering Materials and Technology*, 115(2):220–226, 1993.

[24] W. Cheng, I. Finnie, M. Gremaud, and M. B. Prime. Measurement of near-surface residual-stresses using electric- discharge wire machining. *Journal of Engineering Materials and Technology*, 116(1):1–7, 1994.

[25] R. M. Christensen. *Theory of Viscoelasticity*. Academic Press, New York, NY, second edition, 1982.

[26] B. Clausen, S.-Y. Lee, E. Ustundag, C. C. Aydıner, R. D. Conner, and M. A. M. Bourke. Compressive yielding of tungsten reinforced bulk metallic glass composites. *Scripta Materialia*, 49(2):123–128, 2003.

[27] M. H. Cohen and D. Turnbull. Molecular transport in liquids and glasses. *Journal of Chemical Physics*, 31(5):1164–1169, 1959.

[28] R. D. Conner, R. B. Dandliker, and W. L. Johnson. Mechanical properties of tungsten and steel fiber reinforced Zr41.25Ti13.75Cu12.5Ni10Be22.5 metallic glass matrix composites. *Acta Materialia*, 46(17):6089–6102, 1998.

[29] L. Daudeville and H. Carre. Thermal tempering simulation of glass plates: Inner and edge residual stresses. *Journal of Thermal Stresses*, 21(6):667–689, 1998.

[30] A. K. Doolittle. Studies in Newtonian flow .2. the dependence of the viscosity of liquids on free-space. *Journal of Applied Physics*, 22(12):1471–1475, 1951.

[31] D. Dragoi, E. Ustundag, B. Clausen, and M. A. M. Bourke. Investigation of thermal residual stresses in tungsten-fiber/bulk metallic glass matrix composites. *Scripta Materialia*, 45(2):245–252, 2001.

[32] H. J. Fecht. Thermodynamic properties of amorphous solids —glass-formation and glass-transition—. *Materials Transactions JIM*, 36(7):777–793, 1995.

[33] J. D. Ferry. *Viscoelastic Properties of Polymers*. Wiley, New York, NY, third edition, 1980.

[34] R. Gardon. Thermal tempering of glass. In R. D. Uhlmann and N. J. Kreidl, editors, *Glass: Science and Technology*, volume 5, chapter 5, pages 145–216. Academic Press, Orlando, FL, third edition, September 1986.

[35] C. J. Gilbert, R. O. Ritchie, and W. L Johnson. Fracture toughness and fatigue-crack propagation in a Zr-Ti-Ni- Cu-Be bulk metallic glass. *Applied Physics Letters*, 71(4):476–478, 1997.

[36] M. E. Gurtin and E. Sternberg. On the linear theory of viscoelasticity. *Archive for Rational Mechanics and Analysis*, 11(4):291–356, 1963.

[37] V. H. Hammond, M. D. Houtz, and J. M. O'Reilly. Structural relaxation in a bulk metallic glass. *Journal of Non-Crystalline Solids*, 325(1-3):179–186, 2003.

[38] C. H. V. Hastenberg, P. C. Wildervanck, A. J. H. Leenen, and G. G. J. Schennink. The measurement of thermal-stress distributions along the flow path in injection-molded flat plates. *Polymer Engineering and Science*, 32(7):506–515, 1992.

[39] Y. He, R. B. Schwarz, D. Mandrus, and L. Jacobson. Elastic moduli, density, and structural relaxation in bulk amorphous Zr41.2Ti13.8Cu12.5Ni10Be22.5 alloy. *Journal of Non-Crystalline Solids*, 207:302–306, 1996.

[40] M. R. Hill and W. Y. Lin. Residual stress measurement in a ceramic-metallic graded material. *Journal of Engineering Materials and Technology*, 124(2):185–191, 2002.

[41] F. P. Incropera and D. P. DeWitt. *Fundamentals of Heat and Mass Transfer*. Wiley, New York, NY, fourth edition, 1996.

[42] V. L. Indenbom. *Zhurnal Tekhnicheskoi Fiziki*, 24(5):925–928, 1954.

[43] W. L. Johnson, J. Lu, and M. D. Demetriou. Deformation and flow in bulk metallic glasses and deeply undercooled glass forming liquids—a self consistent dynamic free volume model. *Intermetallics*, 10(11-12):1039–1046, 2002.

[44] V. Keryvin, M. L. Vaillant, T. Rouxel, M. Huger, T. Gloriant, and Y. Kawamura. Thermal stability and crystallization of a Zr55Cu30Al10Ni5 bulk metallic glass studied by in situ ultrasonic echography. *Intermetallics*, 10(11-12):1289–1296, 2002.

[45] C. Kittel. *Introduction to Solid State Physics*. Wiley, New York, NY, sixth edition, 1986.

[46] A. J. Kovacs. Transition vitreuse dans les polymeres amorphes. Etude phenomenologique. *Adv. Polymer Science*, 3:394–507, 1964.

[47] A. J. Kovacs, J. J. Aklonis, J. M. Hutchinson, and A. R. Ramos. Isobaric volume and enthalpy recovery of glasses .2. transparent multi-parameter theory. *Journal of Polymer Science Part B-Polymer Physics*, 17(7):1097–1162, 1979.

[48] C. R. Kurkjian. Relaxation of torsional stress in the transformation range of a soda-lime-silica glass. *Physics and Chemistry of Glasses*, 4(4):128–136, 1965.

[49] R. S. Lakes. *Viscoelastic Solids*. CRC Press, Boca Raton, FL, 1998.

[50] E. H. Lee, T. G. Rogers, and T. C. Woo. Residual stresses in a glass plate cooled symmetrically from both surfaces. *Journal of the American Ceramic Society*, 48(9):480–487, 1965.

[51] P. Lequeu, P. Lassince, T. Warner, and G. M. Raynaud. Engineering for the future: weight saving and cost reduction initiatives. *Aircraft Engineering and Aerospace Technology*, 73(2):147–159, 2001.

[52] G. U. Losi and W. G. Knauss. Thermal-stresses in nonlinearly viscoelastic solids. *Journal of Applied Mechanics-Transactions of the Asme*, 59(2), 1992.

[53] J. Lu. *Mechanical behavior of bulk metallic glass and its composite over a wide range of strain rates and temperatures*. PhD thesis, California Institute of Technology, Pasadena, CA, 2002.

[54] J. Lu, G Ravichandran, and W. L. Johnson. Deformation behavior of the Zr41.2Ti13.8CU12.5Ni10Be22.5 bulk metallic glass over a wide range of strain-rates and temperatures. *Acta Materialia*, 51(12):3429–3443, 2003.

[55] M. Lutz. *Programming Python*. O'reilly and Associates, Sebastopol, CA, second edition, 2001.

[56] A. Markovsky and T. F. Soules. An efficient and stable algorithm for calculating fictive temperatures. *Journal of the American Ceramic Society*, 67(4):C56–C57, 1984.

[57] A. Masuhr, T. A. Waniuk, R. Busch, and W. L. Johnson. Time scales for viscous flow, atomic transport, and crystallization in the liquid and supercooled liquid states of Zr41.2Ti13.8Cu12.5Ni10.0Be22.5. *Physical Review Letters*, 82(11):2290–2293, 1999.

[58] S. Matsuoka. *Relaxation Phenomena in Polymers*. Hanser, Munich, 1992.

[59] G. B. McKenna and S. L. Simon. Time dependent volume and enthalpy responses in polymers. In R. A. Schapery and T. S. Sun, editors, *Time Dependent and Nonlinear*

Effects in Polymers and Composites, ASTM STP 1357, pages 18–46. American Society for Testing and Materials, West Conshohocken, PA, 2000.

[60] E. H. Morland, L. W.and Lee. Stress analysis for linear viscoelastic materials with temperature variation. *Transactions of the Society of Rheology*, 4:233–263, 1960.

[61] C. T. Moynihan, P. B. Macedo, C. J. Montrose, P. K. Gupta, M. A. Debolt, J. F. Dill, B. E. Dom, P. W. Drake, A. J. Easteal, P. B. Elterman, R. P. Moeller, H. Sasabe, and J. A. Wilder. Residual stresses in a glass plate cooled symmetrically from both surfaces. *Annals of the New York Academy of Sciences*, 279:15–35, 1976.

[62] R. Muki and E. Sternberg. On transient thermal stresses in viscoelastic materials with temperature dependent properties. *Journal of Applied Mechanics*, 28:193–207, 1961.

[63] O. S. Narayanaswamy. Model of structural relaxation in glass. *Journal of the American Ceramic Society*, 54(10):491–498, 1971.

[64] O. S. Narayanaswamy. Stress and structural relaxation in tempering glass. *Journal of the American Ceramic Society*, 61(3-4):146–152, 1978.

[65] O. S. Narayanaswamy and R. Gardon. Calculation of residual stresses in glass. *Journal of the American Ceramic Society*, 52(10):554–558, 1969.

[66] K. Ohsaka, S. K. Chung, W. K. Rhim, A. Peker, D. Scruggs, and W. L. Johnson. Specific volumes of the Zr41.2Ti13.8Cu12.5Ni10.0Be22.5 alloy in the liquid, glass, and crystalline states. *Applied Physics Letters*, 70(6):726–728, 1997.

[67] A. Peker and W. L. Johnson. A highly processable metallic-glass - Zr41.2Ti13.8Cu12.5Ni10.0Be22.5. *Applied Physics Letters*, 63(17):2342–2344, 1993.

[68] M. B. Prime. Residual stress measurement by successive extension of a slot: The crack compliance method. *Applied Mechanics Reviews*, 52(2):75–96, 1999.

[69] M. B. Prime and I. Finnie. Surface strains due to face loading of a slot in a layered half-space. *Journal of Engineering Materials and Technology*, 118(3):410–418, 1996.

[70] M. B. Prime and M. R. Hill. unpublished research, 2002.

[71] M. B. Prime and M. R. Hill. Residual stress, stress relief, and inhomogeneity in aluminum plate. *Scripta Materialia*, 46(1):77–82, 2002.

[72] M. S Rekhson and S. M. Rekhson. Shear, uniaxial, and biaxial stress-relaxation functions. *Journal of the American Ceramic Society*, 69(9):704–708, 1986.

[73] S. M. Rekhson and O. V. Mazurin. Stress and structural relaxation in Na2O-CaO-SiO2 glass. *Journal of the American Ceramic Society*, 57(7):327–328, 1974.

[74] H. N. Ritland. Limitations of the fictive temperature concept. *Journal of the American Ceramic Society*, 39(12):403–406, 1956.

[75] G. S. Schajer. Application of finite-element calculations to residual-stress measurements. *Journal of Engineering Materials and Technology*, 103(2):157–163, 1981.

[76] G. W. Scherer and S. M. Rekhson. Viscoelastic-elastic composites .1. general-theory. *Journal of the American Ceramic Society*, 65:352–360, 1982.

[77] F. Schwarzl and A. J. Staverman. Time-temperature dependence of linear viscoelastic behavior. *Journal of Applied Physics*, 23(8):838–843, 1952.

[78] W. Seifert, A. Maschke, and M. Dubiel. Glass transition and instant freezing theories - a comparison of frozen-in temper stresses. *Glastechnische Berichte-Glass Science and Technology*, 71:341–351, 1998.

[79] W. F. Simmons and H. C. Cross. Report on elevated temperature properties of stainless steels. Technical report, American Society for Testing Materials, Philadelphia, PA, 1952.

[80] J. Snyder and Johnson W. L. Thermal conductivity of Zr41.2Ti13.8Cu12.5Ni10Be22.5. unpublished data.

[81] T. F. Soules, R. F. Busbey, S. M. Rekhson, A. Markovsky, and M. A. Burke. Finite-element calculation of stresses in glass parts undergoing viscous relaxation. *Journal of American Ceramic Society*, 70(2):90–95, 1987.

[82] L. C. E. Struik. Orientation effects and cooling stresses in amorphous polymers. *Polymer Engineering and Science*, 18(10):799–811, 1978.

[83] D. W. Suh and R. H. Dauskardt. Mechanical relaxation time scales in a Zr-Ti-Ni-Cu-Be bulk metallic glass. *Journal of Materials Research*, 17(6):1254–1257, 2002.

[84] D. A Tanner, J. S Robinson, and R. L. Cudd. Cold compression residual stress reduction in aluminium alloy 7010. *Materials Science Forum*, 347-349:235–240, 2000.

[85] S. P. Timoshenko and J. N. Goodier. *Theory of Elasticity*. McGraw-Hill, New York, NY, third edition, 1970.

[86] A. Q. Tool. Relation between inelastic deformability and thermal expansion of glass in its annealing range. *Journal of the American Ceramic Society*, 29:240–253, 1946.

[87] N. W. Tschoegl. *The Phenomenological Theory of Linear Viscoelastic Behavior: An Introduction*. Springer-Verlag, Berlin, 1989.

[88] L. J. van der Pauw. A method of measuring specific resistivity and hall effect of discs of arbitrary shape. *Philips Research Reports*, 13:1–9, 1958.

[89] T. A. Waniuk, R. Busch, A. Masuhr, and W. L. Johnson. Equilibrium viscosity of the Zr41.2Ti13.8Cu12.5Ni10Be22.5 bulk metallic glass-forming liquid and viscous flow during relaxation, phase separation, and primary crystallization. *Acta Materialia*, 46(15):5229–5236, 1998.

[90] M. L. Williams, R. F. Landel, and J. D. Ferry. Temperature dependence of relaxation mechanisms in amorphous polymers and other glass-forming liquids. *Physical Review*, 98(5):240–253, 1955.

[91] D. J. Wulpi. *Understanding How Components Fail*. American Society for Metals, Metals Park, OH, second edition, 1999.

[92] S. R. Yazdi, D. Retraint, and J. Lu. Experimental study of residual stress distributions in quenched parts by the incremental large hole drilling method and by the neutron diffraction method. *Journal of Testing and Evaluation*, 28(4):282–289, 2000.

[93] W. F. Zoetelief, L. F. A. Douven, and A. J. I. Housz. Residual thermal stresses in injection molded products. *Polymer Engineering and Science*, 36(14):1886–1896, 1996.